Flight Dynamics Model of A Small Flexible Aircraft

A DISSERTATION
SUBMITTED TO THE FACULTY OF THE GRADUATE SCHOOL
OF THE UNIVERSITY OF MINNESOTA
BY

Abhineet Gupta

IN PARTIAL FULFILLMENT OF THE REQUIREMENTS
FOR THE DEGREE OF
DOCTOR OF PHILOSOPHY

Peter J. Seiler, co-advisor
Gary J. Balas, co-advisor

December, 2019

Acknowledgements

The research conducted for this thesis would not have been possible without the guidance and support of a lot of people. First, I would like to express my gratitude towards Prof. Gary Balas who accepted me as his student and agreed to guide me through my PhD. Perhaps, more than his knowledge and expertise in the field of aerospace engineering and controls, he inspired me with his attitude towards academics and research. His philosophy about conducting high quality research and making significant contribution to the rest of the research community in an openly accessible manner will continue to inspire me throughout my career.

Upon the untimely demise of Prof. Balas, my current adviser Prof. Peter Seiler graciously agreed guide me for the rest of my PhD. Prof. Seiler's guidance has been the primary driving force behind the research. His work ethics, dedication towards research and willingness to help his students in every way possible, be it about academic progress, career or personal life are unparalleled.

Dr. Harald Pfifer and Dr. Daniel Ossmann, who served as post-doctoral research associates for my research group, provided me with a more personalized level of oversight. Their day-to-day guidance has been imperative for this research. I would also acknowledge my colleagues including Chris Regan, Brian Taylor, Dr. Claudia Moreno, Dr. Aditya Kotikalpudi, Sally Ann Keyes and Dr. Julian Theis who collaborated on the project and were always ready to help and support me in my endeavors. The PhD and master students in the research group were always willing to have engaging discussions and provide feedback whenever I needed it.

Dedication

To my family

Abstract

The presence of aeroservoelastic effects in the flight dynamics of flexible aircraft presents significant challenges in terms of performance degradation and instability. In order to develop control system for such aircraft, an accurate flight dynamics model is needed. Developing such a model is an multi-disciplinary effort and requires theoretical and experimental knowledge and research. This thesis describes the development of the flight dynamics model of a small, flexible aircraft. Each step of the multi-stage process of the development of the flight dynamics model is described. The steps include designing and conducting vibration experiments on the aircraft for system identification of the structural dynamics and the development of a finite element model based structural model based on the acquired data. Aerodynamic models are developed and implemented using modifications of standard vortex and doublet lattice methods. The purpose of the modifications is to capture the geometric nonlinearity. The effects of these complex phenomena on the flight dynamics and instability (flutter) are analyzed. Mean axes based flight dynamics equations are utilized. These subcomponents are implemented in the simulation software SIMULINK to obtain the flight dynamics model. Flight tests are conducted to obtain data which is used to update the flight dynamics model by updating the aerodynamics model of the aircraft. A correction matrices based approach is used for this purpose. The resulting model has low computational cost but is capable of capturing complex behavior like geometric nonlinearities and unsteady aerodynamics. The low computational cost and modularity of the flight dynamics model makes it ideal for analysis of the effect of various kinds of aerodynamics and structural phenomena. For example, the significant effects of the capturing the geometrically nonlinear aerodynamics on flutter characteristics of the aircraft are easily evaluated by this model without long, tedious and resource intensive computations. The model is also suitable for Monte-Carlo analysis to estimate the effect of various kinds of open-loop and closed-loop uncertainties.

Contents

List of Tables

List of Figures

Chapter 1

Introduction

Long and slender, high aspect ratio wings with flexible airframes are increasingly being incorporated in the designs of the modern aircraft [1, 2]. Significant weight reductions are possible using such designs. They achieve higher aerodynamics efficiency and thus, lead to a reduction in cost of operation including fuel cost. But, such designs also lead to an increase in the interaction between the structural dynamics, aerodynamics and the rigid body dynamics of the aircraft. As the aircraft becomes more flexible, the frequencies of the flexible modes decrease and approach the frequencies of the rigid body dynamics and the aerodynamics modes. This gives rise to dynamic coupling between these modes. These modes can also interact with the control system of the aircraft. Note that both computer based autopilots and human pilots are prone to such interactions. The phenomena of these interactions are known as aeroservoelasticity [3, 4]. Research in the field of aeroservoelasticity involves a multi-disciplinary approach which includes study of aerodynamics, structural dynamics and control theory [5].

Aeroservoelastic interactions [6] can not only degrade the performance of an aircraft but they can also lead to instability due to various phenomena like flutter, divergence and control surface reversal [3, 4]. This implies that design of flutter suppression control system [7, 8, 9, 10, 11, 12, 13] and aeroservoelastic analysis of the aircraft [2] are imperative for flexible aircraft. Therefore, a mathematical flight

dynamics model which is capable of modeling various aeroservoelastic interactions is required. Such a model can be utilized at various stages of aircraft development. For example, the model can be used during aircraft design stage to evaluate the performance of the aircraft or during control design stage to help design and analyze a flutter suppression control system. This thesis focuses on development of such a mathematical flight dynamics model of a flexible aircraft. The following section contains the outline of the thesis describing the process of the development of the flight dynamics model. Section 1.2 contains the details of the contribution made by this thesis.

1.1   Outline of the Thesis

The process of developing the flight dynamics model consists of developing the models for various submodules and integrating them together. The steps of the development process is outlined here and details are provided in separate chapters.

Chapter 2 provides an overview of the research project including its objectives, challenges faced and the research-through-development approach taken to achieve its goals. The details of the specific flexible aircraft on which the research is conducted are also provided. This includes the details of the fabrication process and geometric and mass properties.

Chapter 3 provides the an overview of the proposed flight dynamics model. The flight dynamics model involves separate mathematical models for various subcomponents of the aircraft. An overview of the overall modeling approach and the interconnection between various subcomponents are described.

Chapter 4 describes the mean axes approach used to obtain the flight dynamics equations of the flexible aircraft. The resulting decoupling between the rigid body and the flexible dynamics of the aircraft by utilizing the mean axes framework is discussed. The assumptions and the derivation of the equations of motion are discussed. Calculations of various sensor outputs using the mean axes approach are also discussed.

Chapter 5 describes process of the development of the finite element method (FEM) based structural model, used to compute the deflections (translations and rotations) of the structure under external loads. The details of the ground vibration test (GVT), the post-processing of the data obtained and the process of updating the FEM model based on the data are discussed in this chapter.

Chapter 6 provides the details of development of the aerodynamic model. The model is used to calculate the forces acting on the aircraft due to the airflow around it. Panel method based models are derived and implemented to calculate the steady and unsteady aerodynamic forces. The modifications in these methods to capture the geometrically nonlinear effects on the aerodynamic forces are described in the chapter.

Chapter 7 describes the implementation of various submodules in the simulation software SIMULINK to obtain the flight dynamics model. The chapter includes the linearization and analysis of the flight dynamics and flutter characteristics of the aircraft. Effects of aerodynamic phenomena like the presence of geometric nonlinearities and unsteady aerodynamics are also analyzed.

Chapter 8 describes the process of comparison and validation of the flight dynamics model using flight test data. The details of the processing of flight test data to obtain estimated frequency response and using it to update the flight dynamics model with a goal to reduce the mismatch between the model and the data is described.

Chapter 9 provide details of the conclusions drawn from this thesis.

1.2 Contribution of the Thesis

The multi-disciplinary research conducted in this thesis contributes to the field of aerospace engineering in the following ways.

- **Structural Dynamics**: Ground vibration test are conducted on a flexible aircraft. The process of designing and executing the vibration experiments

for a small flexible aircraft is described in this thesis. This includes the physical design of the experiment and selection of hardware, input and output selection and the post-processing of the data. The design of experiment and the lessons learned can be followed by researchers for their system.

- **Aerodynamics**: Panel based methods are modified to include complex phenomena like geometric nonlinearities. These modifications increases the capability and complexity of the existing methods while keeping the computation cost low. This results in a low cost and relatively easier method to capture complex aerodynamic behavior instead of using computation fluid dynamics approaches.

- **Flight Dynamics Model**: A modular, nonlinear, control oriented flight dynamics model for a flexible aircraft is developed. The model has several desirable properties. The nonlinear model has a low computational cost so that the control system can be implemented and tested quickly at various stages of control design. A linear model is easily obtained from the nonlinear model. The linear model is low order to facilitate the process of control system design. The modular nature of the flight dynamics model makes it more flexible in terms of analyzing the effect of various phenomena. For example, the effect of geometric nonlinearity in the aerodynamics can be easily evaluated by including geometrically linear or geometrically nonlinear aerodynamic submodule while keeping rest of the model same. This modular nature and the low computational cost of the model makes it particularly suitable for Monte Carlo analysis.

- **Model Update**: Flight tests are conduced to capture data suitable for system identification of the aircraft. A basis function based correction method is utilized to update the panel method based aerodynamics model to update the flight dynamics model. This process of implementation of this methods as well as lessons learned is useful for aerospace researchers. The flight

dynamics model of the flexible aircraft Geri is available for free at [14] and [15].

Chapter 2

Background

2.1 Introduction

This thesis describes a framework for the development of flight dynamics models of flexible aircraft. The details of the development of the model for a specific aircraft, called *Geri*, are discussed. Geri was built as part of the broader Performance Adaptive Aeroelastic Wing (PAAW) project [16]. This chapter provides an overview of the PAAW project and details of the aircraft Geri. The details of the PAAW project, its objectives, challenges faced and the research-through-development approach taken to achieve its goals are described in Section 2.2. Section 2.3 provides in-depth details of the test aircraft Geri. The fabrication process, geometric and mass properties and an analysis of the dynamic instability of the aircraft are discussed.

2.2 PAAW Project

As discussed in Chapter 1, high-aspect ratio, flexible aircraft presents significant challenges in terms of flight performance and instability due to aeroservoelastic phenomena. Performance Adaptive Aeroelastic Wing (PAAW) is a NASA Research Announcement (NRA) project which aims to address these challenges [16].

Key objectives of this research program are to enable high aspect ratio, flexible wings, and to utilize the inherent flexibility of the aircraft to control its shape for optimized performance across the flight envelope [17].

The PAAW project takes an integrated approach to aircraft design and flight control to reduce these aeroservoelastic effects. The programs utilizes a *research-through-development* approach that emphasizes incremental flight testing. Several aircraft are fabricated throughout the project keeping particular short term goals in mind like system identification, autopilot test and flutter suppression control system development. The first set of aircraft, designated mAEWing1, are intended to provide initial knowledge and experience [18]. The design of these aircraft are based on the Body Freedom Flutter (BFF) vehicle. The BFF vehicle was designed by Lockheed Martin and Air Force Research Laboratory [19, 20] to serve as a test-bed for aeroservoelastic research. The aircraft has a similar design as the X-56A test aircraft [21]. The mAEWing1 series of aircraft serve as testbed to develop modeling, design and flutter suppression capabilities [22]. This thesis focuses on the development of the flight dynamics model of an aircraft called Geri in the mAEWing1 series. The details of aircraft Geri are discussed in Section 2.3.

Subsequent aircraft designs scale up the size and complexity to serve as better representation of full size aircraft. mAEWing2 series of aircraft are fabricated to serve as a proof of scalability of the aircraft design to a full size aircraft. An aircraft from mAEWing2 series (during fabrication) and an aircraft from mAEWing1 series are shown in Figure 2.1. mAEWing2 aircraft are also used to validate the mathematical models [23] and Multidisciplinary Design and Analysis (MDAO) tools [24] developed so far.

The PAAW project has a large team of researchers from both industry and academia. The team includes members from Systems Technology, Inc. (STI), D.K. Schmidt and Associates, CMSoft, Inc., Aurora Flight Sciences, Virginia Polytechnic Institute and State University (Virginia Tech.), and University of Minnesota. Researches from Virginia Tech. developed tools for aircraft design using Multi-Disciplinary Design, Analysis and Optimization (MDAO) methods.

Figure 2.1: mAEWing1 and mAEWing2 aircraft

Virginia Tech and CMSoft developed high-fidelity models based on computational fluid dynamics. STI and D.K. Schmidt and Associates focused on developing low order aircraft models, control system design, system identification and flight test support. Researches at University of Minnesota focused on the aircraft build, ground tests, flight tests, control law design and developing medium fidelity flight dynamics models. Finally, Aurora Flight Sciences and Virginia Tech. contributed to the work done on extrapolation from the sub-scale tests to full scale as part of N+3 studies.

2.3 Overview of the Aircraft Geri

This thesis focuses on the developing a medium fidelity flight dynamics model of the aircraft Geri. Geri is designed and fabricated at the University of Minnesota as part of the mAEWing1 series of aircraft. The details of the design, build and tests of the mAEWing1 aircraft are described in [18] and briefly summarized here. The aircraft was designed using a multi-disciplinary design and optimization approach [25]. The aircraft has a blended wing-body, flying-wing design as shown in Figure 2.2. The wings were designed to be removable and easily replaceable. Several centerbodies and wingsets were built with variations in the design for

testing purposes. This design choice allows wings of various stiffness to be tested. It also minimizes risk as the centerbody can be re-used even if the wings have a structural failure during flight tests.
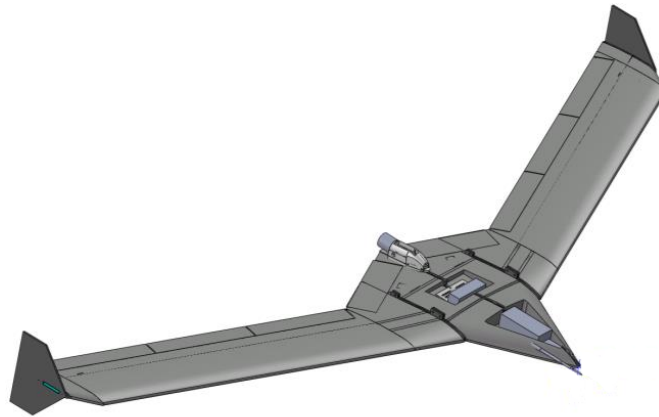
Figure 2.2: Geri aircraft

2.3.1   Physical Layout

The dimensions of Geri are shown in Figure 2.3. The wings are swept back at an angle of 22 degrees. The aircraft has a span of 3.05 meters. Winglets have been added to the wing tips, as shown in Figure 2.2, for directional (yaw) stability. The centerbody stores the flight computer, batteries, propulsion system, video camera and an inertial measurement unit (IMU). Accelerometers are located in centerbody and wings. The internal structure of the aircraft and various component are described in details next.

Figure 2.4 shows the internal layout of the aircraft. The spars are the main load carrying structures in the wings, shown in blue in the figure. Stiffness properties of the spars are critical to flutter characteristics of the aircraft. They span the entire length of the wings and continue through the wing separation joints to a rigid structure in the centerbody. The spars are fabricated using several plies of carbon fiber fabric and epoxy composite over an extruded polystyrene foam core.
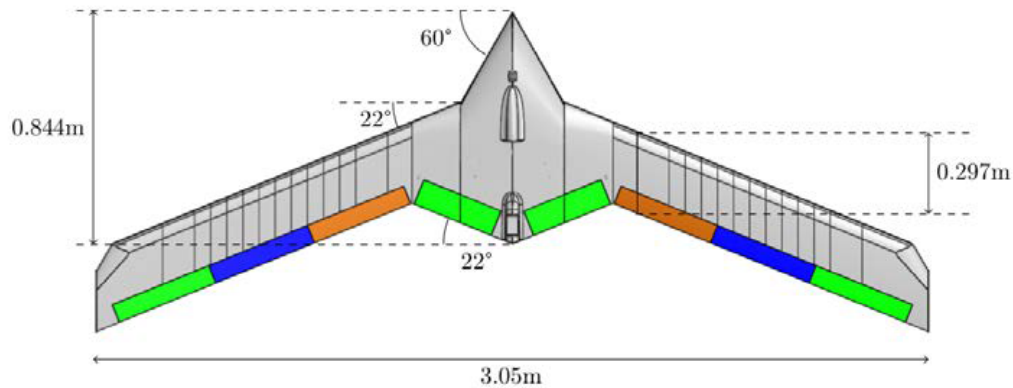
Figure 2.3: Geri planform and dimensions

Tension bolts (not shown) are used to attach the wing to the centerbody.

The on-board electronics are housed in the centerbody. An aerodynamic shell covers the spar and the centerbody. This shell consists of a low density, expanded polystyrene foam with the appropriate airfoil shape and an outer layer that combines carbon fiber and fiberglass reinforced epoxy composites. The forward avionics bay houses the flight computers and majority of the flight sensors. The propulsion system is an electric motor mounted at the trailing edge of the center chord of the aircraft. A rear bay houses the propulsion battery, power regulation and a high definition video recorder. The propulsion motor and the speed controller are housed in a motor mount located near the trailing edge of the center chord.

Figure 2.5 shows a top-view of Geri with key components labeled. The dominant direction excited by the first flutter mode is vertical, i.e. with motion in and out of the page for the top-view shown in Figure 2.5. In order to capture this motion, a total of six accelerometer are mounted on the aircraft such that their sensitive axis is vertical as well. They are located close to the leading edge and trailing edge of the centerbody as well as near to the left and right wingtips. A pitot-static probe is mounted forward of the nose with the pneumatic tubing routed to the pressure transducers in the avionics bay.

A video camera is attached at the center chord in the centerbody, just forward
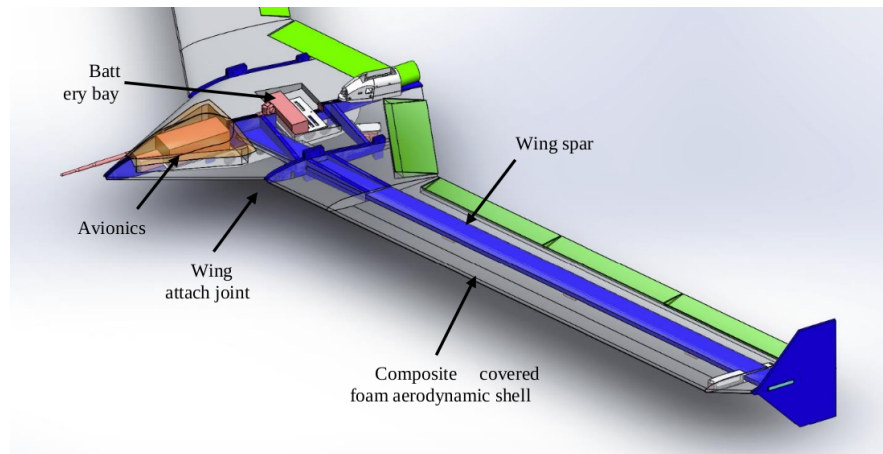
Figure 2.4: Internal layout of Geri
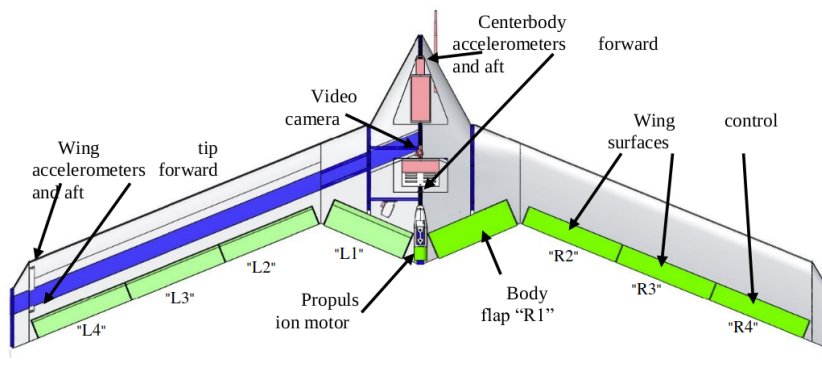
Figure 2.5: Top view of Geri

of the battery bay and the camera recorder is housed in the battery bay. The camera is aimed at tracking features on the winglets and records video onboard for post flight analysis. The flight computer used in Geri is a modified version of the *Goldy* flight control system [26]. An additional micro-controller is included to handle much of the sensor communication in order to reduce the overall time delay in the system. This enables tight latencies with a closed-loop delay of around 20 milliseconds.

Geri has a total of eight trailing edge control surfaces. Two body flaps are located in the centerbody, one on the left (denoted 'L1') and one on the right (denoted 'R1'). Three control surfaces are located in each wing (left surfaces denoted 'L2', 'L3' and 'L4' and right surfaces denoted 'R2', 'R3', and 'R4'). Hobby grade servo motors are utilized to actuate the control surfaces. These servos are mounted to the bottom surface of the wings and centerbody using metal brackets. Various tests were performed to characterize the bandwidth performance, rate limit, and time delay of the servos. The 3 dB bandwidth of the servo motors, tested with a ±5 degree amplitude, is estimated to be 29.48 Hz. Freeplay is found to be 0.213 degree in the servos. There is an additional 0.25-0.5 degree play in the control surface linkages. The servo rate limits are approximately 600 degree/sec. The control surfaces had mechanical deflection limits at approximately ±45 degrees.

2.3.2 Mass and Structural Properties

The mass and the structural properties of the aircraft are described in this section. Static and dynamic tests were conducted to obtain these properties. Table 2.1 shows the mass, center of gravity and the moment of inertia of Geri. The coordinate frame used for these measurements are such that the origin is located at the nose of the aircraft, the x-axis points in the forward direction, y-axis points towards the 'right' wing and the z-axis points towards the ground (downwards). The moments of inertia about the CG of the aircraft are tabulated where I_{xx} represents the roll inertia, I_{yy} represents the pitch inertia and I_{zz} represents the yaw inertia.

Mass (kg)	x-CG location (m)	y-CG location (m)	z-CG location (m)	Inertia I_{xx} (kg-m^2)	Inertia I_{yy} (kg-m^2)	Inertia I_{zz} (kg-m^2)
6.24	-0.603	0.0	-0.0076	2.739	0.462	3.174

Table 2.1: Mass and inertia properties of Geri

The structural properties of the aircraft play a critical role in determining

its flight dynamics properties, including flutter characteristics. The structural properties of Geri are determined by a series of static and dynamic tests. The details of these static and dynamic tests and the development of a finite element method based structural model are described in Chapter 5. Key features of the structural properties are summarized here.

The aircraft exhibits five structural modes under 35 Hz. These are the modes of the (dry) aircraft at zero airspeed. The aeroelastic modes at different flight speeds result from these (dry) structural modes interacting with aerodynamic effects. These modal frequencies and the details of the mode are described in Table 2.2 while the shapes are shown in Figure 2.6.

Mode number	Modal frequency: Hz (rad/s)	Mode shape details
1	7.81 (49.07)	1st symmetric bending
2	10.00 (62.83)	1st anti-symmetric torsion
3	14.73 (92.55)	1st symmetric torsion
4	19.72 (123.90)	1st anti-symmetric bending
5	32.44 (203.83)	2nd symmetric bending

Table 2.2: Modal parameters of Geri

For a symmetric aircraft, the vibration modes can be categorized into purely symmetric and anti-symmetric modes. This separation of the modes can result in a significant reduction in computational cost for calculation of the natural modes and frequencies as well as in the resulting dynamic responses of the aircraft. It is observed that Geri does not exhibit structural symmetry [27]. This loss of symmetry is due to small deviations in the manufacturing process for the two wings. Due to this loss in symmetry, the modes can no longer be classified into purely symmetric and anti-symmetric modes. Therefore the mode shape descriptions provided in Table 2.2 as symmetric or anti-symmetric should only be considered as approximate.

The lowest frequency mode is the first symmetric bending mode at 7.81 Hz. The corresponding mode shape is shown in the top row of Figure 2.6. In the first symmetric bending mode the two wing tips are displaced in the same direction
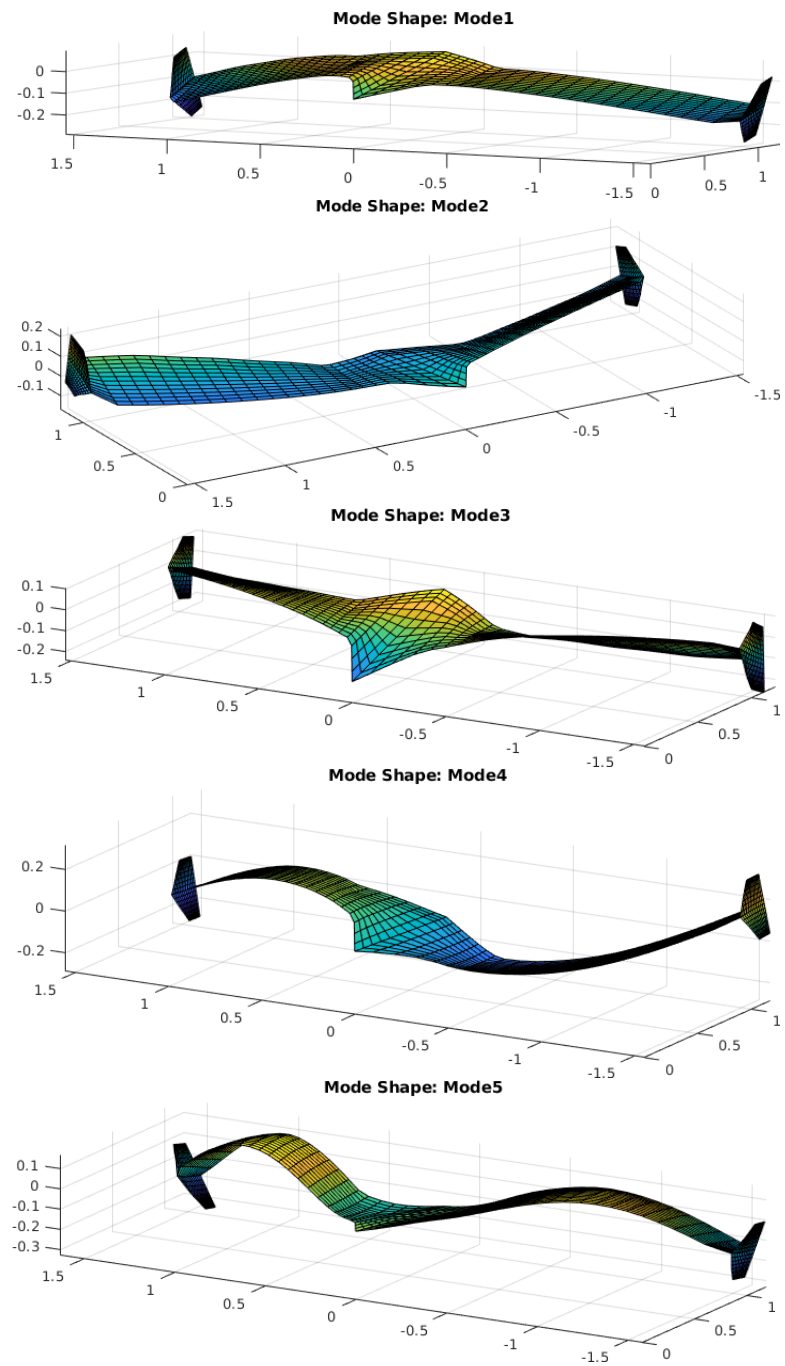
Figure 2.6: Mode shapes of Geri

perpendicular to the planform, while the centerbody is displaced in the opposite direction. The entire structure experiences approximately constant bending and no torsion. It should be reiterated here that this description is approximate and the displacement of the two wing tips is not the same due to the presence of asymmetry in the aircraft.

The second mode is the first anti-symmetric torsion mode at 10.00 Hz. In the first anti-symmetric torsion mode the two wing tips are twisted in the opposite directions while the centerbody is not twisted. The third mode is the first symmetric torsion mode at 14.73 Hz. In the symmetric torsion mode the two wing tips are twisted in the same direction while the centerbody is twisted in the opposite direction. The aircraft does not experience bending in both these torsion modes. The forth mode is the first anti-symmetric bending mode at 19.72 Hz. In the first anti-symmetric bending mode the two wing tips are displaced in the opposite directions perpendicular to the planform while the centerbody is not displaced. One peak and and one trough is observed in the mode shape creating an 'S' shape. The fifth mode is the second symmetric bending mode at 32.44 Hz. In the second symmetric bending mode the two wing tips are displaced in the same direction while the centerbody displaced in the opposite direction. Two peaks are observed in the mode shape. The aircraft does not experience torsion in modes 4 and 5.

2.3.3   Flutter Characteristics

The modes described in the previous section are for the structural dynamics of the aircraft without any external aerodynamic forces acting on it. These are called genesis modes. For an aircraft in flight, the aerodynamic forces acting on it interact with the structural modes and change the dynamics of the aircraft. The resulting modes are called aeroelastic modes. These aeroelastic modes change with the velocity of the aircraft.

If the velocity exceeds a critical value, then these modes can go unstable resulting in flutter. The variation of the poles of flight dynamics system of Geri

with velocity is shown in the root locus plot in Figure 2.7. The first structural mode changes with velocity and goes unstable at 33.5 m/sec. The frequency of the mode changes from 49.1 rad/sec at zero airflow velocity to 37.3 rad/sec at the flutter point. This flutter mode is known as the body freedom flutter mode and is characterized by the interaction of the short period mode and the first symmetric bending mode.
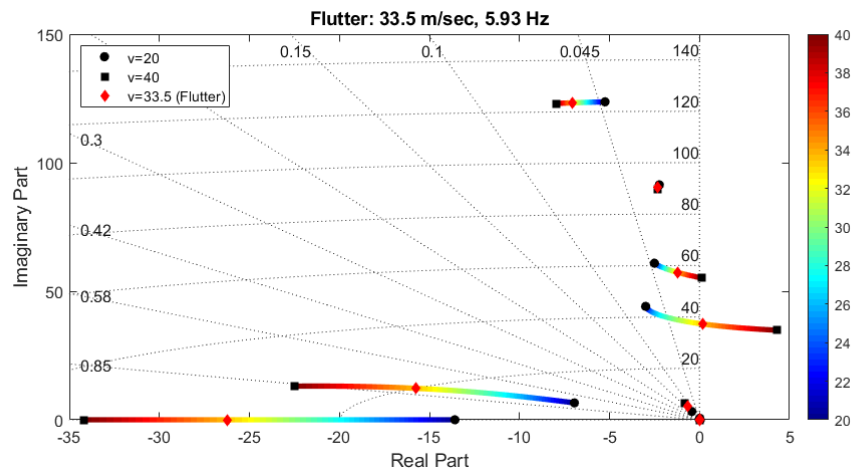
Figure 2.7: Flutter characteristics of Geri

The flutter characteristics described above are obtained using the flight dynamics modeling framework presented in this thesis. The specific model is described Chapter 7 and is updated with flight test data as described in Chapter 8. Figure 2.7 shows the flutter characteristics from the flight test updated model.

Chapter 3

Model Overview

3.1 Introduction

An overview of the proposed flight dynamics model is provided in this chapter. The flight dynamics model involves separate mathematical models for various subcomponents of the aircraft. Figure 3.1 describes overall modeling approach and the interconnection between the subcomponents. The subcomponents include structural dynamics, aerodynamics, rigid body dynamics, sensors, actuators and propulsion system [5]. The propulsion and the aerodynamic models are used to calculate the forces acting on the aircraft in flight. The propulsion force depends on the throttle input provided by the pilot. The aerodynamic forces depend on the control input, the rigid body states and flexible states. A mean axes [28] based approach is taken towards the flight dynamics which results in a decoupling of the rigid body and structural dynamics. The forces calculated by the aerodynamic model are used by the rigid body dynamics to calculate the rigid states; and by the structural dynamics model to calculate the flexible states. The sensor models are used to calculate the output of various on-board sensors based on the rigid body and flexible states.

The models of these subcomponents are implemented in the simulation software *SIMULINK* to obtain a six degrees of freedom, nonlinear, flight dynamics

model of the aircraft. The flight dynamics model can be also be linearized at any trim point to obtain a low order, linear, state-space model. The details of the model of each subcomponent is described in Section 3.2. The mean axes frame used to model the interaction between the subcomponents is described in Section 3.3.
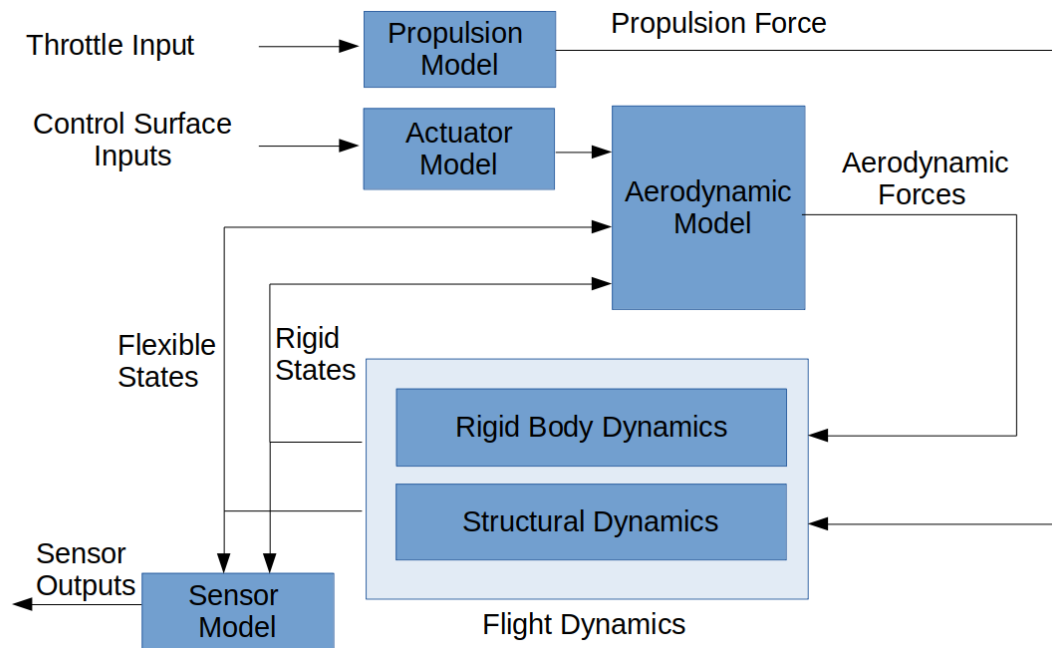
Figure 3.1: Flight dynamics modeling framework

3.2 Subcomponents

3.2.1 Structural Dynamics

This section provides an overview of the structural dynamics model for the flexible aircraft. Details on the development of this structural model are provided in Chapter 5. The model for this subcomponent describes the dynamics of the structure under external loads. Specifically, the model inputs are the external

forces acting on the structure. The model is used to compute the deflections (translations and rotations) of the structure under these loads. A simple, beam based, finite element method (FEM) [29] approach is chosen to model the structural dynamics of Geri. The process of developing the FEM model consists of the following steps:

1. **Initial model**: An initial FEM model is created based on the aircraft CAD model.

2. **Static test and FEM update**: Simple static tests are used to collect basic data for the aircraft. This data is used to perform a first update on the FEM model.

3. **Ground vibration tests (GVTs) and FEM update**: Dynamic ground vibration tests were conducted to obtain dynamic structural data for the Geri aircraft. The data was used for a second update and validation of the FEM model.

3.2.2 Aerodynamics

The aerodynamic forces acting on the aircraft are modeled using numerical, potential flow based, panel methods. The details of the aerodynamic model are given in Chapter 6. The steady forces are calculated using the Vortex Lattice Method (VLM) [30]. The VLM models the aircraft lifting surfaces, e.g. the wings, as flat plates consisting of discrete horseshoe vortices. A zero normal flow boundary condition is enforced at the collocation point of each panel. The collocation points are assumed to be at the three-quarter point of the center chord of each panel. This boundary condition is used to compute the strength of the horseshoe vortex attached to the panel. Lift and induced drag are calculated based on the horseshoe vortex strength and flight conditions like airspeed and angle of attack. The VLM neglects the influence of the panel thickness and the fluid viscosity.

The unsteady forces are calculated using the Doublet Lattice Method (DLM) [31, 32, 33]. The DLM also models the lifting surfaces as flat plates like the VLM. The DLM assumes that the flow is across a harmonically oscillating panel. Harmonic pressure distribution across the surface is obtained as a solution for a given flow condition. Thus, the DLM calculates the frequency response for pressure distribution on an oscillating surface in steady flow. The response from the DLM is calculated on a grid of frequencies and is typically fit with a rational function of frequency [34]. This rational function approximation enables time-domain simulations of the unsteady DLM forces.

3.2.3 Rigid Body Dynamics

Modeling the rigid body dynamics of a flexible aircraft presents with certain challenges [5]. It is not trivial to define the position and orientation of a flexible aircraft as it changes its shape in flight due to flexible deflection. A mean axes framework, described in the next section, is used to model the rigid body dynamics of Geri. In this framework, the rigid body translational and rotational dynamics can be described using the position and orientation of the mean axes. This results in six degrees of freedom, nonlinear equations for rigid body dynamics of the aircraft. The details of the mean axes frame used to describe the rigid body dynamics are described in Chapter 4.

3.2.4 Sensors and Actuators

Control inputs are assumed to be symmetric and anti-symmetric deflections of the four sets of left and right control surfaces as shown in Figure 2.5. A second order actuator model is used to calculate control surface deflections and velocities from control input. The aerodynamics forces generated by the control surfaces are modeled by including calculations of the effect of the nonlinear rotations of the corresponding panels of the aerodynamic grid. A simple propulsion model is assumed where the propulsion force is a linear function of the propulsion input.

The moment generated by the propulsion system is assumed to be zero.

Single axis accelerometers are used to measure the acceleration at six locations on the aircraft. An Inertial Measurement Unit (IMU) located at the center of gravity of the dry aircraft is used to measure the orientation of the aircraft. The sensor output depends on rigid body translation, rigid body rotation and flexible deflections. A mean-axes based approach is used to obtain the equations of the sensor output and are described in Section 4.5.

3.3 Mean Axes

The interconnection between the various subcomponents are modeled using the mean axes approach [5, 28, 35]. The mean axes are a set of floating, body axes. The position and orientation of these axes follow a specific set of constraints. The constraints are defined such that the linear and angular momentum relative to these axes due to flexible deflection is zero [28]. The constraints are equivalent to a set of dynamic equations for the position and orientation of the mean axes [36]. Roughly, the position and orientation of the mean axes follow equations of motion similar to those used for a rigid aircraft. The origin of the axes is always located at the instantaneous center of mass of the flexible aircraft.

The advantage of using the mean axes is that under the simplifying assumptions, the rigid body dynamics and the flexible dynamics become decoupled. The details of the mean axes approach, including the assumptions and the resulting equations of motion are described in Chapter 4.

3.4 Validation and Update

The flight dynamics model obtained is updated and validated using flight test data. The flight tests were conducted with specific excitation inputs suitable for system identification. The flight test data is processed to obtain the estimated frequency response from the control input to the sensor output. These

frequency response functions are compared with the corresponding frequency response functions from the flight dynamics model. The flight dynamics model is then modified to minimize the difference between these frequency responses. The update is performed by correcting the aerodynamic model using the correction matrices as described in [37]. An optimization routine is employed to obtain the optimal correction matrices which minimize the difference between the measured and modeled frequency response functions. The procedure and the results of the model update are described in Chapter 8.

3.5   Model Capabilities

This section describes the capabilities and advantages of the flight dynamics modeling approach described in this thesis. The aerodynamic and the structural dynamic models are linear. But the interaction between them is modeled in such a way that the resulting flight dynamics model is capable of capturing certain nonlinear behavior of the flexible aircraft. An example of such nonlinear phenomena is the change in the direction of the local lift with the structural deflection of the aircraft wings. This phenomena could be categorized as geometric nonlinearity. The effect of these nonlinear phenomena are analyzed by comparing the nonlinear simulation model with a model which does not capture these effects.

The model is also capable of including the effect of unsteady aerodynamic forces. It is particularly suitable for modeling transient flights like changing the flight path from a straight and level flight to a banked turn.

The modular nature and the low computational cost of the model makes it particularly suitable for running Monte-Carlo simulations in open-loop configuration to quantify the uncertainty, and in closed-loop configuration to quantify the robustness of the control system.

Chapter 4

Mean Axes Approach

This chapter describes the mean axes approach used to obtain the flight dynamics equations of a flexible aircraft. The mean axes frame is a floating, body reference frame. The frame moves with the aircraft but is not attached to a material point on it. The translational and rotational motion of the mean axes are governed by a particular set of constraints as discussed in Section 4.2.1.

The advantage of using the mean axes framework is that under a few simplifying assumptions, it results in a decoupling between the rigid body and the flexible dynamics of the aircraft. These assumptions and the derivation of the resulting equations of motion are discussed in Section 4.2 and 4.3. The mean axes constraints are equivalent to a set of differential equations that describe the position and orientation of the mean axes as shown in Section 4.4.

4.1 Introduction

Several flight dynamics modeling approaches have been presented in literature for flexible aircraft. These approaches usually result in highly nonlinear and complicated flight dynamic equations. Rigid body dynamics and the flexible dynamics are usually coupled in these cases. These nonlinear, coupled equations require

more computational resources to solve and simulate. The high level of complication of the resulting flight dynamics equations also presents a challenge from a systems and control design perspective. Because of the widely different modeling framework as compared to a conventional, rigid aircraft [38, 39], it is difficult to extend the extensive amount of intuition developed for rigid aircraft to flexible aircraft.

The mean axes approach, first described by Milne in the mid-1960s, has been developed to address these challenges [35]. The mean axes framework has been modified and extended to obtain the flight dynamics model of flexible aircraft as described in [28]. The details of the procedure used to obtain the flight dynamics model are described in [5]. The procedure described in the [5, 28] has been utilized to model the flight dynamics of several aircraft. If the aircraft and the flight envelope satisfy a set of simplifying assumptions, the mean axes approach can be utilized to obtain simplified flight dynamics model of a flexible aircraft. The resulting equations are such that the rigid body dynamics and the flexible dynamics are decoupled. It should be noted that the external aerodynamic and gravitational forces that excite the rigid body and flexible dynamics might still remain coupled. Another advantage of the mean axes approach is that the state vector of the flight dynamics model is an extension of the state vector of a standard, rigid aircraft model. This means that majority of the engineering intuition developed for a rigid aircraft still remains applicable to the flexible aircraft with slight modifications. Care should be taken to ensure that the mean axes framework is used correctly based on the accuracy of assumptions made in mean axes formulation. Detailed discussion on various aspects of applicability of the mean axes framework can be found in [40] and [41].

4.2   Mean Axes

In general, the flight dynamics equations of an aircraft can be obtained by utilizing any reference frame. Inertial, body fixed or floating reference frames are typically

chosen. Even though they represent the dynamics of the same aircraft, the resulting equations of motion are different and vary in their complexity depending on the choice of the reference frame. The mean axes frame is one particular floating reference frame. It moves with the flexible aircraft but is not attached to a material point on it. The translational and rotational motion of the mean axes is defined by a set of constraints as described in [5, 28] These constraints are discussed in Section 4.2.1. It is shown in [42] that the constraints are equivalent to a set of ordinary differential equations as described in Section 4.4 .

4.2.1   Mean Axes Constraints

The mean axes frame is defined by a set of constraints as described in [5, 28] and presented here. To describe the mean axes, consider a flexible body in motion. An infinitesimal element of the flexible body is denoted as dV as shown in the figure below. An inertial reference frame and a body fixed, mean axes frame are considered.
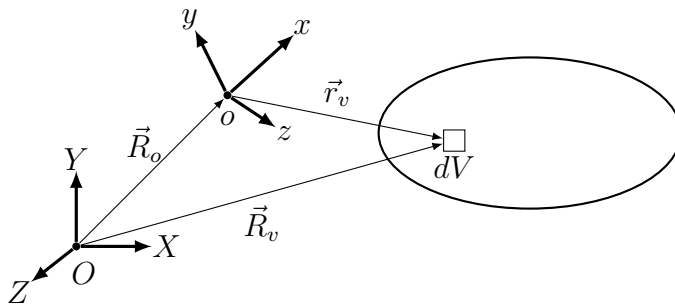
Figure 4.1: Undeformed flexible body along with inertial and mean axes

The inertial reference frame has its origin at O and the axes are denoted as X, Y and Z. Similarly, the mean axes frame has its origin at o and the axes are denoted as x, y and z. The density of the element is ρ and its volume is denoted as dV. The position vector of the origin of the mean axes frame with respect to the inertial frame is denoted by $\vec{R}_o$. The position vector of the mass element dV with respect to the mean axes frame is denoted by $\vec{r}_v$ and with respect to the

inertial axes is denoted by $\vec{R}_v$. The derivative of any vector $\vec{r}$ with respect to the inertial frame will be denoted as:

$$\frac{d\vec{r}}{dt}\bigg|_O = \dot{\vec{r}} \tag{4.1}$$

Similarly, the derivative of any vector $\vec{r}$ with respect to the mean axes frame will be denoted as:

$$\frac{d\vec{r}}{dt}\bigg|_o = \overset{\circ}{\vec{r}} \tag{4.2}$$

The transport theorem will be utilized to relate the two derivatives. The transport theorem states that:

$$\dot{\vec{r}} = \overset{\circ}{\vec{r}} + (\vec{\Omega}_o \times \vec{r}) \tag{4.3}$$

where $\vec{\Omega}_o$ is the angular velocity of the mean axes frame with respect to the inertial frame. The mean axes are implicitly defined by the following constraints on its translational and rotational motion [5]:

- The linear momentum due to elastic deformation relative to the mean axes frame is zero.

$$\int_V \rho \overset{\circ}{\vec{r}}_v \, dV = 0 \tag{4.4}$$

- The angular momentum due to elastic deformation relative to the mean axes frame is zero.

$$\int_V \vec{r}_v \times \rho \overset{\circ}{\vec{r}}_v \, dV = 0 \tag{4.5}$$

Note that the derivatives in the constraint equations described above are with respect to the floating, mean axes frame and not to the inertial frame. It should also be noted that the mean axes constraints are implicit constraints that describe

the velocity of the mean axes frame but do not provide explicit position and orientation of the frame. These implicit constraints and a discussion on their applicability on flexible aircraft are described in [5, 28].

4.2.2 Practical Mean Axes Constraints

The mean axes constraints as described in Equation 4.4 and 4.5 are nonlinear equations and difficult to apply practically. These constraints can be simplified by assuming small flexible deflection. The flexible deflection of the body is shown in Figure 4.2.
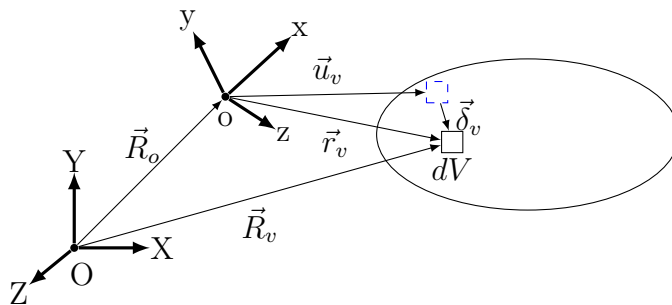
Figure 4.2: Deformed flexible body

Here $\vec{u}_v$ represents the position vector of the undeformed location of the mass element, $\vec{\delta}_v$ denotes the flexible deflection of the element. The deflected position vector of the mass element can be written as a sum of the undeformed position vector and the flexible deflection as

$$\vec{r}_v = \vec{u}_v + \vec{\delta}_v \tag{4.6}$$

It should be noted that as the mean axes frame moves with the flexible body, the underformed position vector $\vec{u}_v$ is a constant. This implies that

$$\overset{\circ}{\vec{u}}_v = 0 \tag{4.7}$$

The translational mean axes constraint described in Equation 4.4 can be written in terms of flexible deflection to obtain the first 'practical mean axes constraint' as follows:

$$\int_V \rho \, \mathring{\vec{r}}_v \, dV = 0$$

$$\implies \int_V \rho \, \mathring{\vec{u}}_v \, dV + \int_V \rho \, \mathring{\vec{\delta}}_v \, dV = 0$$

Substituting Equation 4.7,

$$\int_V \rho \, \mathring{\vec{\delta}}_v \, dV = 0 \tag{4.8}$$

The rotational mean axes constraint given in 4.5 can also be simplified as:

$$\int_V \vec{r}_v \times \rho \, \mathring{\vec{r}}_v \, dV = 0$$

$$\implies \int_V (\vec{u}_v + \vec{\delta}_v) \times \rho(\mathring{\vec{u}}_v + \mathring{\vec{\delta}}_v) \, dV = 0$$

$$\implies \int_V (\vec{u}_v + \vec{\delta}_v) \times \rho \, \mathring{\vec{\delta}}_v \, dV = 0$$

Assuming small flexible deflection, the second 'practical mean axes constraints' is obtained:

$$\int_V \vec{u}_v \times \rho \, \mathring{\vec{\delta}}_v \, dV = 0 \tag{4.9}$$

Now, it is assumed that the flexible deflection of the body is linear and can be written in terms of the free vibration modes. The free vibration modes form a set of orthogonal functions that is used to describe any flexible motion of the body. Note, that the free vibration modes (without external force) are used to describe the forced motion of the body. We can write the flexible deflection as

linear combination of translational free mode shapes (ϕ_t)

$$\vec{\delta}_v = \sum_{i=1}^{\infty} \vec{\phi}_{t_i}(v)\eta_i \tag{4.10}$$

Equation 4.10 is substituted in the practical mean axes Equations 4.8 and 4.9 to obtain the following

$$\sum_{i=1}^{\infty} \frac{d\eta_i}{dt} \int_V \rho \vec{\phi}_{t_i}(v)\, dV = 0 \tag{4.11}$$

$$\sum_{i=1}^{\infty} \frac{d\eta_i}{dt} \int_V \vec{u}_v \times \rho \vec{\phi}_{t_i}(v)\, dV = 0 \tag{4.12}$$

It should be noted that the mean axes constraints focus on the translational and rotational velocities of the of the axes. This means that the translational position and rotational orientation are free parameters that can be chosen arbitrarily. The mean axes constraint described in Equation 4.4 implies that the origin of the mean axes lies at a constant distance from the instantaneous center of mass of the body. To further simplify the calculations, we choose the initial position of the origin of the mean axis to coincide with the instantaneous center of mass of the body. With this choice of initial position of the origin of the mean axes and due to the constraint given in Equation 4.4, it can be concluded that the origin of the mean axes lies at the instantaneous center of mass of the flexible body at all times. This results on the following equation

$$\int_V \rho \vec{r}_v\, dV = 0 \tag{4.13}$$

4.3   Equations of Motion

The equations of motion of a flexible body can be written in the mean axes frame. This derivation is based on the Lagrangian approach as reviewed in this section. Additional details can be found in [5, 28]. The Lagrangian approach calculates the

equations of motion of a body based on its kinetic energy and potential energy. The Lagrange's equations can be written as:

$$\frac{d}{dt}\left[\frac{\partial T}{\partial \dot{q}_i}\right] - \frac{\partial T}{\partial q_i} + \frac{\partial P}{\partial q_i} = Q_i \tag{4.14}$$

where T is the kinetic energy of the system, P is the potential energy, q_i is the ith generalized coordinate which represents a particular degree of freedom of the system and Q_i is the generalized force corresponding to the ith generalized coordinate. The generalized coordinates are usually the position and velocities corresponding to various degrees of freedom of the system.

Kinetic energy

To obtain the equations of motion with respect to mean axes, we need to derive the expressions of kinetic and potential energy and the generalized forces in terms of the mean axes frame parameters and apply Lagrange's equations. Consider a flexible body and mean axes frame as shown in Figure 4.1.

The position of the infinitesimal mass element with respect to the inertial frame can be written as

$$\vec{R}_v = \vec{R}_o + \vec{r}_v \tag{4.15}$$

Therefore, the velocity of the mass element with respect to the inertial frame is given by:

$$\begin{aligned}
\dot{\vec{R}}_v &= \dot{\vec{R}}_o + \dot{\vec{r}}_v \\
&= \dot{\vec{R}}_o + \mathring{\vec{r}}_v + (\vec{\Omega}_o \times \vec{r}_v)
\end{aligned} \tag{4.16}$$

The total kinetic energy of the system can be written as:

$$
\begin{aligned}
T &= \frac{1}{2} \int_V \rho(\dot{\vec{R}}_v \cdot \dot{\vec{R}}_v) dV \\
&= \frac{1}{2} \int_V \rho\big(\dot{\vec{R}}_o + \overset{\circ}{\vec{r}}_v + (\vec{\Omega}_o \times \vec{r}_v)\big) \cdot \big(\dot{\vec{R}}_o + \overset{\circ}{\vec{r}}_v + (\vec{\Omega}_o \times \vec{r}_v)\big) dV
\end{aligned}
\tag{4.17}
$$

Equation 4.17 can be simplified to obtain the following equation:

$$
\begin{aligned}
T = \frac{1}{2} \int_V \rho\Big(&\dot{\vec{R}}_o \cdot \dot{\vec{R}}_o + \overset{\circ}{\vec{r}}_v \cdot \overset{\circ}{\vec{r}}_v + (\vec{\Omega}_o \times \vec{r}_v) \cdot (\vec{\Omega}_o \times \vec{r}_v) + \\
&2\big(\dot{\vec{R}}_o \cdot \overset{\circ}{\vec{r}}_v + \overset{\circ}{\vec{r}}_v \cdot (\vec{\Omega}_o \times \vec{r}_v) + \dot{\vec{R}}_o \cdot (\vec{\Omega}_v \times \vec{r}_v)\big)\Big) dV
\end{aligned}
\tag{4.18}
$$

The expression for kinetic energy can be further simplified using the mean axes constraints as defined in Equations 4.4 and 4.5. The third term drops out as

$$
\frac{1}{2} \int_V 2\rho(\dot{\vec{R}}_o \cdot \overset{\circ}{\vec{r}}_v) \, dV = \dot{\vec{R}}_o \cdot \int_V \rho \overset{\circ}{\vec{r}}_v \, dV = 0
$$

Similarly, the fourth term drops out with the application of circular shift property of the scalar triple product as shown in the equation below:

$$
\frac{1}{2} \int_V 2\rho(\overset{\circ}{\vec{r}}_v \cdot (\vec{\Omega}_o \times \vec{r}_v)) \, dV = \vec{\Omega}_o \cdot \int_V (\vec{r}_v \times \rho \overset{\circ}{\vec{r}}_v) \, dV = 0
$$

The resulting expression for the kinetic energy is:

$$
\begin{aligned}
T = \frac{1}{2} \int_V \rho\Big(&\dot{\vec{R}}_o \cdot \dot{\vec{R}}_o + \overset{\circ}{\vec{r}}_v \cdot \overset{\circ}{\vec{r}}_v + (\vec{\Omega}_o \times \vec{r}_v) \cdot (\vec{\Omega}_o \times \vec{r}_v) + \\
&2\dot{\vec{R}}_o \cdot (\vec{\Omega}_o \times \vec{r}_v)\Big) dV
\end{aligned}
\tag{4.19}
$$

The choice of the origin of the mean axes described in Equation 4.13 results in further simplification in the expression for kinetic energy. The last term in

Equation 4.19 becomes

$$\frac{1}{2}\int_V 2\rho\big(\dot{\vec{R}}_o \cdot (\vec{\Omega}_o \times \vec{r}_v)\big)dV = \vec{\Omega}_o \cdot \left(\int_V \rho(\vec{r}_v \times \dot{\vec{R}}_o)dV\right)$$

The integral expression is given by:

$$\left(\int_V \rho\vec{r}_v\, dV\right) \times \dot{\vec{R}}_o = 0$$

Therefore, the last term vanishes and the expression for the kinetic energy becomes

$$T = \frac{1}{2}\int_V \rho\Big(\dot{\vec{R}}_o \cdot \dot{\vec{R}}_o + \overset{\circ}{\vec{r}}_v \cdot \overset{\circ}{\vec{r}}_v + (\vec{\Omega}_o \times \vec{r}_v) \cdot (\vec{\Omega}_o \times \vec{r}_v)\Big)dV \qquad (4.20)$$

This expression in Equation 4.20 can be broken down to represent the total kinetic energy as a sum of translational and rotational kinetic energy and vibrational kinetic energy as follows:

$$\begin{aligned}
T &= \frac{1}{2}\int_V \rho\Big(\dot{\vec{R}}_o \cdot \dot{\vec{R}}_o + \overset{\circ}{\vec{r}}_v \cdot \overset{\circ}{\vec{r}}_v + (\vec{\Omega}_o \times \vec{r}_v) \cdot (\vec{\Omega}_o \times \vec{r}_v)\Big)dV \\
&= \frac{1}{2}M(\dot{\vec{R}}_o \cdot \dot{\vec{R}}_o) + \frac{1}{2}\int_V \rho(\overset{\circ}{\vec{r}}_v \cdot \overset{\circ}{\vec{r}}_v)dV + \frac{1}{2}\vec{\Omega}_o^T [I]\vec{\Omega}_o
\end{aligned} \qquad (4.21)$$

where M is the total mass of the body and I is the instantaneous inertia tensor of the body with respect to the origin of the mean axes. It can be seen that the total kinetic energy of the body as described in Equation 4.21 is the sum of the rigid body translational kinetic energy, the kinetic energy of the body due to flexible motion with respect to the axes and rigid body rotational kinetic energy. Thus, it can be observed that the mean axes constraints lead to a separation between the rigid body and flexible kinetic energy.

Finally, we use the practical mean axes constraint given in Equation 4.11 to

further simplify the second term in the kinetic energy expression in Equation 4.21.

$$\frac{1}{2}\int_V \rho(\mathring{\vec{r}}_v \cdot \mathring{\vec{r}}_v)dV = \frac{1}{2}\int_V \rho(\mathring{\vec{\delta}}_v \cdot \mathring{\vec{\delta}}_v)dV$$
$$= \frac{1}{2}\int_V \rho\left(\left(\sum_{i=1}^{\infty} \vec{\phi}_{ti}\frac{d\eta_i}{dt}\right) \cdot \left(\sum_{i=1}^{\infty} \vec{\phi}_{ti}\frac{d\eta_i}{dt}\right)\right)dV \tag{4.22}$$

As the translational free vibration modes are orthogonal to each other, the following expression is true:

$$\int_V \vec{\phi}_{ti} \cdot \vec{\phi}_{tj}\rho \, dV := 0 \text{ if } i \neq j \tag{4.23}$$

Thus, the Equation 4.22 can be written as:

$$\frac{1}{2}\int_V \rho\left(\left(\sum_{i=1}^{\infty} \vec{\phi}_{ti}\frac{d\eta_i}{dt}\right) \cdot \left(\sum_{i=1}^{\infty} \vec{\phi}_{ti}\frac{d\eta_i}{dt}\right)\right)dV = \frac{1}{2}\sum_{i=1}^{\infty}\left(\frac{d\eta_i}{dt}\right)^2 \underbrace{\int_V \vec{\phi}_{ti} \cdot \vec{\phi}_{ti}\rho \, dV}_{M_i} \tag{4.24}$$

where M_i is the generalized mass for i^{th} mode. The final expression of kinetic energy is

$$T = \frac{1}{2}M(\dot{\vec{R}}_o \cdot \dot{\vec{R}}_o) + \frac{1}{2}\sum_{i=1}^{\infty}\left(\frac{d\eta_i}{dt}\right)^2 M_i + \frac{1}{2}\vec{\Omega}_o^T [I]\vec{\Omega}_o \tag{4.25}$$

Potential energy

The potential energy of the system can be written as a sum of elastic potential energy and gravitational potential energy as:

$$P = P_g + P_e \tag{4.26}$$

The gravitational potential energy is given by:

$$P_g = -\int_V \vec{R}_v \cdot \vec{g}\rho \, dV \tag{4.27}$$

This can be simplified as follows

$$P_g = -(\vec{R}_o \cdot \vec{g}) \underbrace{\int_V \rho \, dV}_{=M} - \vec{g} \cdot \underbrace{\int_V \rho \vec{r}_v \, dV}_{=0} = -(\vec{R}_o \cdot \vec{g})M \qquad (4.28)$$

The elastic potential energy is calculated using D'Alembert's principle. For the given flexible body, the elastic potential energy is

$$P_e = -\frac{1}{2} \int_V \vec{\overset{\circ\circ}{\delta}}_v \cdot \vec{\delta}_v \rho \, dV \qquad (4.29)$$

Using Equation 4.10 and 4.29, the elastic potential energy can be written as:

$$P_e = \frac{1}{2} \sum_{i=1}^{\infty} \omega_i^2 \eta_i^2 M_i \qquad (4.30)$$

where ω_i is the modal frequency of ith mode and η_i is the modal deflection coordinate for i^{th} mode. Thus, the total potential energy is

$$\begin{aligned} P &= P_g + Pe \\ &= \vec{R}_o \cdot \vec{g}M + \frac{1}{2} \sum_{i=1}^{\infty} \omega_i^2 \eta_i^2 M_i \end{aligned} \qquad (4.31)$$

Generalized coordinates

The Lagrange's approach to deriving the equations of motions require the use of generalized coordinates. These generalized coordinates are chosen as translational position of the mean axes frame and the Euler angles describing the rotational orientation of the mean axes frame. The modal deflection coordinate η_i are also chosen as the generalized coordinates. The details of these generalized coordinates are discussed next.

Consider the components of the $\vec{R}_o$ in the mean axes frame.

$$\vec{R}_o = x\hat{i} + y\hat{j} + z\hat{k} \tag{4.32}$$

The translational velocity of mean axes position can also be written in terms of its components in the mean axes frame as:

$$\dot{\vec{R}}_o = U\hat{i} + V\hat{j} + W\hat{k} \tag{4.33}$$

The angular velocity of the mean axes can similarly be written in terms of its components as:

$$\vec{\Omega}_o = p\hat{i} + q\hat{j} + r\hat{k} \tag{4.34}$$

These components can be written in terms of Euler angles (ϕ, θ, ψ) and their derivatives as follows.

$$p = \dot{\phi} - \dot{\psi}\sin\theta \tag{4.35a}$$

$$q = \dot{\psi}\cos\theta\sin\phi + \dot{\theta}\cos\phi \tag{4.35b}$$

$$r = \dot{psi}\cos\theta\cos\phi - \dot{\theta}\sin\phi \tag{4.35c}$$

The relationship between the translational and the angular velocities are

$$U = \dot{x} + qz - ry \tag{4.36a}$$

$$V = \dot{y} + rx - pz \tag{4.36b}$$

$$W = \dot{z} + py - qx \tag{4.36c}$$

The kinetic and the potential energies can be written in terms of these generalized

coordinates.

$$T = \frac{1}{2}M(U^2 + V^2 + W^2) + \frac{1}{2}\begin{bmatrix} p & q & r \end{bmatrix}[I]\begin{bmatrix} p \\ q \\ r \end{bmatrix} + \frac{1}{2}\sum_{i=1}^{\infty} M_i\dot{\eta}_i^2 \qquad (4.37)$$

$$P = \vec{R}_o \cdot \vec{g}M + \frac{1}{2}\sum_{i=1}^{\infty}\omega_i^2\eta_i^2 M_i \qquad (4.38)$$

The equations of motion are derived using Lagrange's approach shown in Equation 4.14. The resulting equations of motion are described below.

Translational equations:

$$M[\dot{U} - rV + qW + g\sin\theta] = Q_x \qquad (4.39a)$$

$$M[\dot{V} - pW + uU - g\sin\phi\cos\theta] = Q_y \qquad (4.39b)$$

$$M[\dot{W} - qU + pV - g\cos\phi\cos\theta] = Q_w \qquad (4.39c)$$

where Q_x, Q_y and Q_z are the generalized forces with respect to the x, y and z generalized coordinates. These generalized forces are described in Chapter 6.

Rotational equations:

$$I_{xx}\dot{p} - (I_{yy} - I_{zz})qr + I_{xy}(pr - \dot{q}) - I_{xz}(pq + \dot{r}) + I_{yz}(r^2 - q^2) = Q_\phi \quad (4.40a)$$

$$I_{yy}\dot{q} - (I_{zz} - I_{xx})pr + I_{yz}(pq - \dot{r}) - I_{xy}(qr + \dot{p}) + I_{xz}(p^2 - r^2) = Q_\theta \quad (4.40b)$$

$$I_{zz}\dot{r} - (I_{xx} - I_{yy})pq + I_{xz}(qr - \dot{p}) - I_{yz}(pr + \dot{q}) + I_{xy}(q^2 - p^2) = Q_\psi \quad (4.40c)$$

where Q_ϕ, Q_θ and Q_ψ are the generalized forces for ϕ, θ and ψ generalized coordinates.

Flexible equations:
The equations of motion obtained using the generalized coordinates η_i describe

the flexible dynamics for each flexible mode.

$$\ddot{\eta}_i + \omega_i^2 \eta_i = \frac{Q_{\eta_i}}{M_i} \text{ for } i = 1, 2, 3, \cdots \tag{4.41}$$

Usually, only the first few modes are included in the flight dynamics model and the higher order flexible modes are discarded.

4.4 Explicit Equations of Mean Axes

The mean axes constraints described in Equations 4.5 and 4.5 are a set of implicit constraints that describe the motion of the mean axes frame. These constraints cannot be used to calculate the position and orientation of the mean axes frame explicitly. [42] provides an equivalent derivation of the mean axes framework using newtonian mechanics. An important result described in [42] is that the mean axes constraints uniquely define the equations of motion of the frame up to an arbitrary but constant rotation of the frame. These equivalent equations of motion of the mean axes are:

- Translation:

$$M\ddot{\vec{r}}_o = \vec{F}_{ext} \tag{4.42}$$

  with the initial conditions

$$\vec{r}_o(0) = \frac{1}{M} \int_V \rho \vec{r}_v(0) dV$$
$$\dot{\vec{r}}_o(0) = \frac{1}{M} \int_V \rho \dot{\vec{r}}_v(0) dV$$

  where F_{ext} = total external forces acting on the aircraft.

- Rotation:

$$\frac{d(I\vec{\Omega}_o)}{dt} = M_{ext} \tag{4.43}$$

with the initial condition:

$$\vec{\omega}_0 = I^{-1}(0) \tag{4.44}$$

where M_{ext} = total external moment acting on the aircraft, I is the instantaneous moment of inertia of the body with respect to the mean axes.

These results show that the equations of motion in the mean axes framework are essentially an extension of the well known rigid body equations for a flexible body.

4.5 Sensor Equations

An aircraft is usually fitted with various on-board sensors which are utilized for navigation and flight control systems as well as any flutter suppression control system. The flight dynamics equations can be used to calculate the output of these sensors. As the mean axes framework is used to model the flight dynamics of the flexible aircraft, the output of the on-board sensors are also calculated using the mean axes approach as described in this section.

Consider Figure 4.3 where the on-board sensor is denoted by S. The blue dot represents the undeflected position of the sensor and the red dot represents the deflected position.
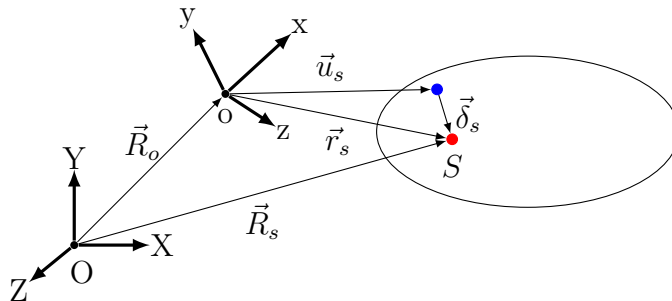
Figure 4.3: Sensors on a deformed flexible body

The output of two types of sensors are described below.

4.5.1   Accelerometer

An accelerometer measures the acceleration at a particular location on the aircraft. The accelerometer could be single-axis or multi-axis. A multi-axis accelerometer measures the inertial acceleration in all three directions while a single axis accelerometer is restricted to the inertial acceleration measurement along one particular axis. The complete inertial acceleration vector with three degrees of freedom is calculated next.

The inertial acceleration of the sensor S can be denoted by $\ddot{\vec{R}}_v$. The position vectors are related as:

$$\vec{R}_s = \vec{R}_o + \vec{u}_s + \vec{\delta}_s \tag{4.45}$$

The velocity in the inertial frame can be obtained as:

$$
\begin{aligned}
\dot{\vec{R}}_s &= \dot{\vec{R}}_o + \dot{\vec{u}}_s + \dot{\vec{\delta}}_s \\
&= \dot{\vec{R}}_o + [\overset{\circ}{\vec{u}}_s + (\Omega_o \times \vec{u}_s)] + [\overset{\circ}{\vec{\delta}}_s + (\Omega_o \times \vec{\delta}_s)] \\
&= \dot{\vec{R}}_o + (\Omega_o \times \vec{u}_s) + \overset{\circ}{\vec{\delta}}_s + (\Omega_o \times \vec{\delta}_s)
\end{aligned}
\tag{4.46}
$$

The acceleration at the sensor location in the inertial frame can be obtained as:

$$
\begin{aligned}
\ddot{\vec{R}}_s &= \ddot{\vec{R}}_o + (\dot{\Omega}_o \times \vec{u}_s) + (\Omega_o \times (\mathring{\vec{u}}_s + (\Omega_o \times \vec{u}_s))) \\
&\quad + \mathring{\mathring{\vec{\delta}}}_s + (\Omega_o \times \mathring{\vec{\delta}}) + (\dot{\Omega}_o \times \vec{\delta}_s) + (\Omega_o \times (\mathring{\vec{\delta}}_s + (\Omega_o \times \vec{\delta}_s)))) \\
&= \ddot{\vec{R}}_o + (\dot{\Omega}_o \times (\vec{u}_s + \vec{\delta}_s)) + (\Omega_o \times (\Omega_o \times (\vec{u}_s + \vec{\delta}_s))) + \mathring{\mathring{\vec{\delta}}}_s + 2(\Omega_o \times \mathring{\vec{\delta}})
\end{aligned}
\tag{4.47}
$$

The measured acceleration can be written in terms of the mean axes frame parameters and modal deflections as follows:

$$
\begin{aligned}
\ddot{\vec{R}}_s &= \ddot{\vec{R}}_o + (\dot{\Omega}_o \times (\vec{u}_s + \sum_{i=1}^{\infty} \vec{\phi}_{t_i} \eta_i)) \\
&\quad + (\Omega_o \times (\Omega_o \times (\vec{u}_s + \sum_{i=1}^{\infty} \vec{\phi}_{t_i} \eta_i))) + \sum_{i=1}^{\infty} \vec{\phi}_{t_i} \ddot{\eta}_i + 2(\Omega_o \times \sum_{i=1}^{\infty} \vec{\phi}_{t_i} \dot{\eta}_i)
\end{aligned}
\tag{4.48}
$$

where $\vec{\phi}_{t_i}$ is the translational part of the ith mode shape and η_i is the ith modal deflection coordinate.

4.5.2 Inertial Measurement Unit

An Inertial Measurement Unit (IMU) is a sensor which measures the angular velocity. The output of the IMU sensor can be written as a sum of the angular velocity of the mean axes frame and the angular velocity due to flexible deflection as:

$$
\vec{\Omega}_s = \Omega_o + \sum_{i=1}^{\infty} \vec{\phi}_{r_i} \dot{\eta}_i
\tag{4.49}
$$

where $\vec{\phi}_{r_i}$ is the translational part of the ith mode shape and η_i is the ith modal deflection coordinate.

Chapter 5

Structural Model

This chapter describes the structural model for the flexible aircraft Geri. The structural model is developed using the Finite Element Method (FEM) [29]. The model describes the dynamics of the structure under external loads. The inputs of the model are the external forces acting on the structure. The model is used to compute the deflections (translations and rotations) of the structure under these loads. The structural model is a subcomponent of the flight dynamics model of the flexible aircraft. It interacts with the aerodynamic model which calculates the forces acting on the aircraft based on its deflected shape. Details of the development of the FEM model are provided in the remainder of this chapter.

There are several possible methodologies for modeling the structural dynamics of a flexible aircraft. The choice of the methodology depends on the aircraft in question and the flight regime. For example, High-Altitude Long-Endurance (HALE) aircraft usually have very high aspect ratio, flexible wings. These aircraft exhibit large deflections during flight [43]. These large deflection cannot be represented by a simple linear displacement function and a nonlinear representation is required. This type of nonlinearity is known as structural geometric nonlinearity. Structural geometric nonlinearity plays a significant role for HALE aircraft and needs to be taken into account in the structural dynamics model. A flexible aircraft can also exhibit material nonlinearity if the deflection does not follow

the proportional stress-strain relationship [44]. If the material nonlinearities are significant, then the structural dynamics needs to take them into account as well [45, 46].

For any chosen framework, the level of detail and the complexity of the model also need to be chosen. For example, the wings of a flexible aircraft can be modeled as an equivalent Euler-Bernoulli beam attached to a stiff center body [47]. Such a model is computationally inexpensive and is capable of calculation of simple parameters like tip deflection and the first few vibration frequencies. Such models do not contain sufficient details to calculate high frequency mode shapes or structural deflections at arbitrary points on the aircraft. The complexity of beam based models can be increased by incorporating nonlinear beam elements [48]. On the other hand, models with extremely high fidelity and complexity can be obtained by incorporating highly nonlinear, computational structural mechanics based methods [43, 49]. These models are more accurate but they are computationally expensive. The order of these models can be reduced to obtain control oriented models [50].

Several factors were considered when selecting a suitable structural dynamic model framework for the flexible aircraft Geri. Geri is part of a series of flexible aircraft fabricated for the PAAW project called mAEWing1 [18]. These aircraft share the same outer mold line and aerodynamics properties but have slightly varying structural properties. The previous aircraft in the mAEWing1 series exhibit a tip deflection of around 10% of the wingspan in a typical flight test. This is considered to be within the scope of a geometrically linear structural model. Static stiffness tests were also conducted on the wings of Geri. The wings were found to exhibit a proportional stress-strain relationship. This implies that material nonlinearity does not play a significant role in the structural dynamics and can be ignored.

Based on these factors, a beam-based finite element structural model is considered suitable for the aircraft Geri. To develop the FEM based model, the complete structure is discretized into simpler elements [29]. These elements are

interconnected at finite number of points, called nodes, common to two or more elements. Equations for each element are formulated separately and then combined to obtain the equations for the complete structure. This results in a set of simultaneous algebraic equations. Therefore, the FEM discretizes the structure to approximate the (infinite dimensional) partial differential equation with a set of finite dimensional ordinary differential equations. The FEM-based structural model for Geri was constructed as follows:

1. **Initial model**: An initial FEM model was created based on the aircraft CAD model. The details of the initial finite element model are discussed in Section 5.1.

2. **Static test and FEM update**: Simple static tests were conducted and the collected data was used to perform a first update on the FEM model.

   - **Static test**: Static tests were conducted to estimate the mass, inertia and stiffness properties for the aircraft. These included tests to measure the mass, center of gravity, moment of inertia, and stiffness of spar and wings. These tests are described further in Section 5.2.1.

   - **FEM update**: The estimated properties of the aircraft were used to update the FEM model. The details of the update procedure of the initial FEM model using the static test results are described in section 5.2.2.

3. **Ground vibration tests (GVT) and FEM update**: Several ground vibration tests were conducted to obtain dynamic structural data for the aircraft. The test data was used for a second update and validation of the FEM model.

   - **GVT: setup**: The setup of the experiment is described in Section 5.3.1.

   - **GVT: procedure**: The procedure of the experiment and data acquisition is described in Section 5.3.2.

- **GVT: Post-processing**: The experimental data is acquired in the form of time domain, force and acceleration signals. The time domain data is processed to obtain frequency domain parameters like mode shapes and modal frequencies. Two post-processing methods are described in Section 5.4

- **FEM update**: The experimental modal parameters are used to update the FEM model to obtain the final structural dynamic model of the aircraft. The details of FEM update are provided in Section 5.5.

5.1 Initial Model

An initial FEM model was created for Geri by a team at Virginia Tech using data from a CAD model of the aircraft. The model was based on simple, beam-rod based elements as shown in Figure 5.1. The details of the development of the model are provided in [51]. This section briefly summarizes the key features of this initial FEM model.
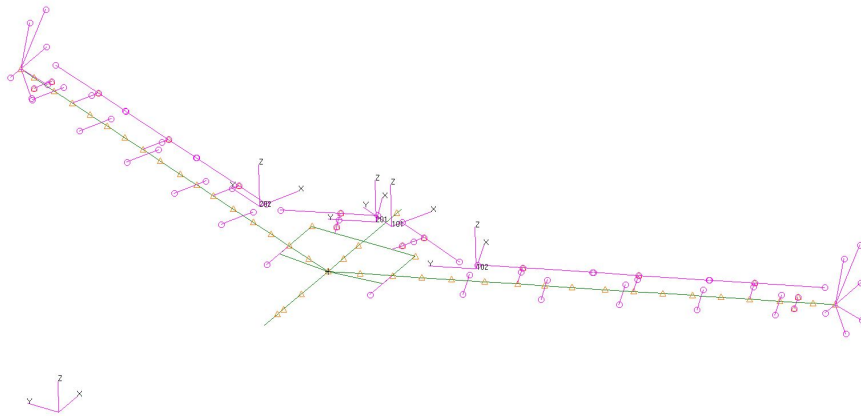
Figure 5.1: Finite element model of Geri

The centerbody of the aircraft was fabricated by encompassing a rib-based structure with low density expanded polystyrene foam. The foam was covered with a combination of carbon fiber and fiberglass reinforced epoxy composites.

The forward avionics bay of the centerbody houses the avionics including the flight computers and a majority of the sensors, e.g. the pitot-static transducers. The rear bay houses the propulsion battery, power regulation and a high definition video recorder. The centerbody of the aircraft was modeled as a rod in the initial FEM model. The mass of the foam and the cover fabric were modeled as a uniformly distributed mass along the rod. The electronic components located in the centerbody were modeled as point masses. As the propulsion battery occupies a significant volume, it was modeled as a point mass/inertia with moments of inertia about its local x and y axes.

The rectangular solid spars are the main load carrying structures in the aircraft wings. The spars were fabricated from a foam core with 3-layer carbon fiber laminate reinforcements surrounding the core. The spars have a uniform cross-section and are assumed to have uniform stiffness and mass properties. The spars were fabricated to have specific stiffness properties based on the desired design of the aircraft. The properties were updated after manufacturing based on static tests conducted on the bare spars as described in the following subsection. Simple beam elements were used to model the spar in the FEM model.

The foam and the cover fabric on the wings provide additional stiffness. The foam and the cover fabric were also modeled as a beam elements, separate from the beam elements for the solid spar. The beam elements modeling the foam and the cover fabric share the same nodes with the beams modeling the spar. The elastic axis and the center of gravity axis of the beam elements modeling the spar were considered to lie on the centerline of the spar. The spar centerline was also considered the elastic axis of the complete wings. For the beam elements modeling the wing foam and the cover fabric, the stiffness properties were considered to be varying along the wing span. The center of gravity (CG) axis of these beams did not coincide with the elastic axis of the wings. Therefore, additional distributed mass moments of inertia due to the offset between the CG axis and the elastic axis were included in the model.

The hinge bolt for the connection between the body flaps and the centerbody

were modeled as a spring element with a large spring stiffness. The attachments connecting the wing with the centerbody were also modeled as beams. The control surfaces on the wings were modeled as lumped point masses. Extra nodes were created at the locations of the accelerometers used for ground vibration tests described in the next section.

The mass properties of the initial FEM model are described in Table 5.1. The modal frequencies obtained from the model are described in Table 5.2.

Mass (kg)	x-CG location (m)	Inertia I_{xx} (kg-m^2)	Inertia I_{yy} (kg-m^2)
6.24	-0.609	2.816	0.466

Table 5.1: Mass and inertia properties of initial FEM model

Mode number	Modal frequency: Hz (rad/s)
1	8.00 (50.26)
2	13.20 (82.93)
3	16.70 (104.93)
4	19.38 (121.77)
5	31.40 (197.29)

Table 5.2: Modal frequencies from initial FEM model

5.2   Static Tests and FEM Update

Usually, some discrepancy is found between the initial, design based finite element model and the structural dynamics of the aircraft. The sources of these discrepancies include incorrect modeling of specific elements like joints and welds, model order errors such as presence of structural nonlinearities [44] in the aircraft and model parameter errors such as incorrect quantification of material properties [51].

An inaccuracy in the structural model will cause a discrepancy between the

predictions from the model and the flexible response of the aircraft. The inaccuracy in the structural model will translate to inaccuracy in flight dynamics model. Such an inaccuracy induces an error in the flight dynamics model predictions including critical predictions like flutter speed and flutter frequency. Therefore, the finite element model needs to be validated and, if required, corrected to match with the structural dynamics of the aircraft. This process correcting the FEM model is known as finite element model updating [52].

The initial FEM model is based on the data from a CAD model of Geri. Next, static tests are conducted on the fabricated aircraft to obtain estimates of the mass and stiffness properties of the actual structure. These test are described in details in [18] and are summarized in Section 5.2.1. The initial FEM model is updated based on the static test data. The updated FEM model is described in Section 5.2.2.

5.2.1 Static Tests

Mass of the components and complete aircraft were estimated by placing them on a scale that had been calibrated with a known mass. Center of gravity was estimated via simple balancing and measuring with respect to a local datum. The balance test was typically performed with a simple fulcrum. In the case of the complete aircraft, custom fixtures were fabricated to assist in the balancing test. The same fixtures were used in the moment of inertia (MOI) testing ensuring a consistent datum scheme. Pendulum swings were used to estimate the MOI of both the centerbody and the complete aircraft. A bifilar pendulum tests, with the aircraft mounted horizontally as shown in Figure 5.2, was used to estimate the yaw MOI.

Time taken for 20 oscillations was measured and yaw moment of inertia was estimated based on time of oscillation of the pendulum. Similarly, to estimate the roll moment of inertia, the aircraft was mounted vertically, with nose pointing upward, forming a bifilar pendulum. The pitch moment of inertia was estimated

Figure 5.2: Bifilar pendulum test setup

using a compound pendulum setup where the aircraft was mounted vertically, with nose pointing downwards. Products of inertia, e.g. I_{xy}, were expected to be small for this aircraft due to symmetry is mass distribution and were not measured.

The results of the mass and inertia tests conducted on Geri are shown in Table 5.3. The coordinate frame used for the center of gravity (CG) location is shown in Figure 2.2. The moments of inertia about the CG of the aircraft are tabulated where I_{xx} represents the roll inertia, I_{yy} represents the pitch inertia and I_{zz} represents the yaw inertia.

Mass (kg)	x-CG location (m)	y-CG location (m)	z-CG location (m)	Inertia I_{xx} (kg-m^2)	Inertia I_{yy} (kg-m^2)	Inertia I_{zz} (kg-m^2)
6.24	-0.603	0.0	-0.0076	2.739	0.462	3.174

Table 5.3: Mass and inertia properties of Geri

The material properties of the foam used in the wings were not available during the design phase. Also, due to manufacturing variability, significant variations in material properties had been observed in the past for the fabricated wings. Therefore, static tests were conducted on the spar and the wings of Geri to obtain a better estimate of the stiffness properties of these components. Separate tests were conducted on the spars and the wings to estimate the stiffness provided the foam and the cover fabric in the wings.

A simplified diagram of the test setup is shown in Figure 5.3 (taken from [18] with approval for re-use). The static tests were conducted by creating a cantilever constraint on the inboard end of the spar/wing. The structure was loaded with a series of weights. The weights (P) were placed on top of the structure and then hung via a light support rod offset from the center. A three axis precision inclinometer was placed on top of the test structure near the tip. The inclinometer was used to measure the bending (θ) and twist (ϕ) angles for each test weight. The Euler-Bernoulli beam bending theory was used to estimate the bending and torsional stiffness (EI and GJ) using Equations 5.1.

$$
\begin{aligned}
EI &= \frac{Pl^2}{2\theta} \\
GJ &= \frac{Pld}{\phi}
\end{aligned}
\tag{5.1}
$$

The results of the static tests conducted on the spars are shown in Table 5.4. It can be seen that the two spars have similar bending stiffness (EI) and masses. But, there is significant difference between their torsional stiffness values (GJ). This results indicates that the two spars have slightly different properties due to manufacturing variability.

Similar tests were conducted on the complete wings of Geri as well. The complete wings consists of the spar surrounded by the foam core, cover fabric and includes the control surfaces and the servo motors. The results are described in Table 5.5. It can be seen that the stiffness properties of the left and right wings
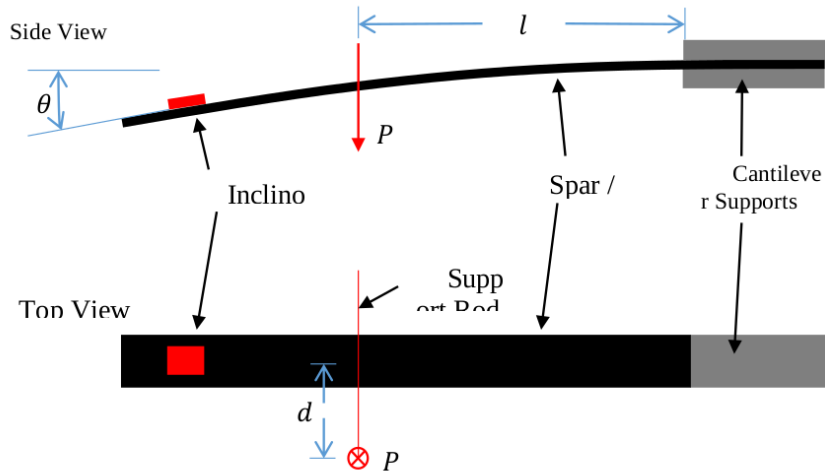
Figure 5.3: Static test set-up

Spar	Mass (kg)	EI (N-m^2)	GJ (N-m^2)
Left spar	0.356	119.29	96.08
Right spar	0.352	119.47	86.18

Table 5.4: Static test results for spars

differ due to manufacturing variability causing and asymmetry in the aircraft.

Spar	Mass (kg)	EI (N-m^2)	GJ (N-m^2)
Left wing	1.392	359.29	299.34
Right wing	1.381	304.75	261.89

Table 5.5: Static test results for wings

5.2.2 FEM Update

The initial FEM model was updated based on the results of the static tests. The asymmetry in the aircraft properties was not taken into account at this step and a symmetric FEM model is assumed. It was decided that the dynamic test results would serve as a better indication of the effects of asymmetry in the aircraft and

asymmetry could be introduced at a later stage. An optimization based update procedure is employed to update the FEM model and is described in [51].

The mass properties of the updated FEM model are shown in Table 5.6 along with the corresponding values form the static test results. It can be seen that the mass properties of the updated FEM model matches with the measured values.

	Mass (kg)	x-CG location (m)	Inertia I_{xx} (kg-m^2)	Inertia I_{yy} (kg-m^2)
Initial FEM model	6.24	-0.609	2.816	0.466
Static Test	6.24	-0.603	2.739	0.462
Updated FEM model	6.25	-0.603	2.640	0.464

Table 5.6: Mass and inertia properties of updated FEM model

The modal frequencies of the updated FEM model are described in Table 5.7. Figure 5.4 show the mode shapes from the updated FEM model.

Mode number	Modal frequency - Initial Model: Hz (rad/s)	Modal frequency - Updated model: Hz (rad/s)	Mode shape - Updated model
1	8.00 (50.26)	7.95 (49.95)	1st symmetric bending
2	13.20 (82.93)	12.5 (78.53)	1st anti-symmetric torsion
3	16.70 (104.93)	15.9 (99.90)	1st symmetric torsion
4	19.38 (121.77)	18.7 (117.49)	1st anti-symmetric bending
5	31.40 (197.29)	31.5 (197.92)	2nd anti-symmetric torsion

Table 5.7: Modal frequencies from updated FEM model

5.3   Ground Vibration Test

After updating and validating the FEM model with the static test data, it was compared with the structural dynamics data of the aircraft. Ground vibration tests (GVT) were conducted to obtain the structural dynamics data from the aircraft. This data was then processed to obtain modal parameters like mode shapes
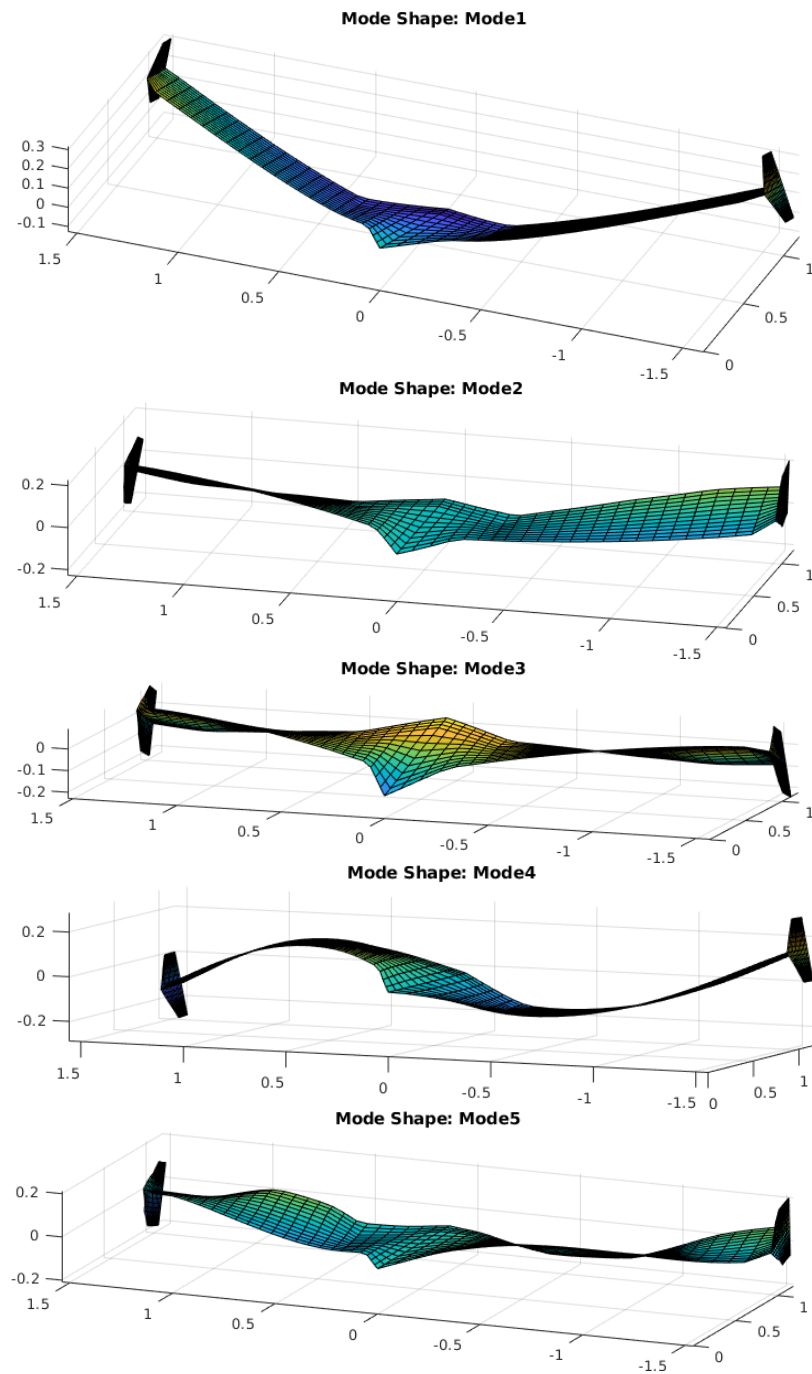
Figure 5.4: Mode shapes from updated FEM model

and modal frequencies. The identified modal parameters were compared with the predicted values from the FEM model to validate it. As the modal parameters predicted by the model were found to be different from the experimental values, the FEM model was updated again [47, 51].

Several considerations go into designing the experiment such as the excitation signal, location of the excitation points and sensors, type of the support to the aircraft, attachment types and data acquisition system requirements [53]. The details of experimental setup and the procedure are described in Section 5.3.1 and 5.3.2 respectively. Similar ground vibration tests have been conducted for other aircraft in mAEWing1 series [54] and for the body freedom flutter aircraft [55]. Post-processing of the experimental data to obtain modal parameters using two different methods is explained in Section 5.4. Section 5.5 discusses the FEM model update using GVT data.

5.3.1 Experimental Setup

The goal of GVT was to obtain structural dynamics data from the aircraft. To obtain such data the aircraft was excited by applying an external force as input. The accelerations of the aircraft at several points were considered as the output. Both input force and output acceleration data were measured using a data acquisition system.

The experimental setup of the ground vibration test is shown in Figure 5.5. The aircraft was suspended from a wooden frame which provides a rigid support to the test setup. A flexible spring was used to suspend the aircraft and was attached to the center of gravity (CG) of the aircraft using a metallic hook. This allowed the aircraft to remain approximately horizontal during the test. The spring was chosen to be of sufficiently low stiffness of 130 Newton/meter so that the aircraft experiences free-free vibration conditions [56]. The mass of the aircraft is 6.24 Kg which implies that the the natural frequency of the mass-spring oscillation was 0.72 Hz. This was well below the lowest modal frequency of the aircraft of around

8 Hz. Thus, the mass-spring oscillation was well separated from the flexible modes in the frequency domain and did not interfere with the identification of the flexible modes.
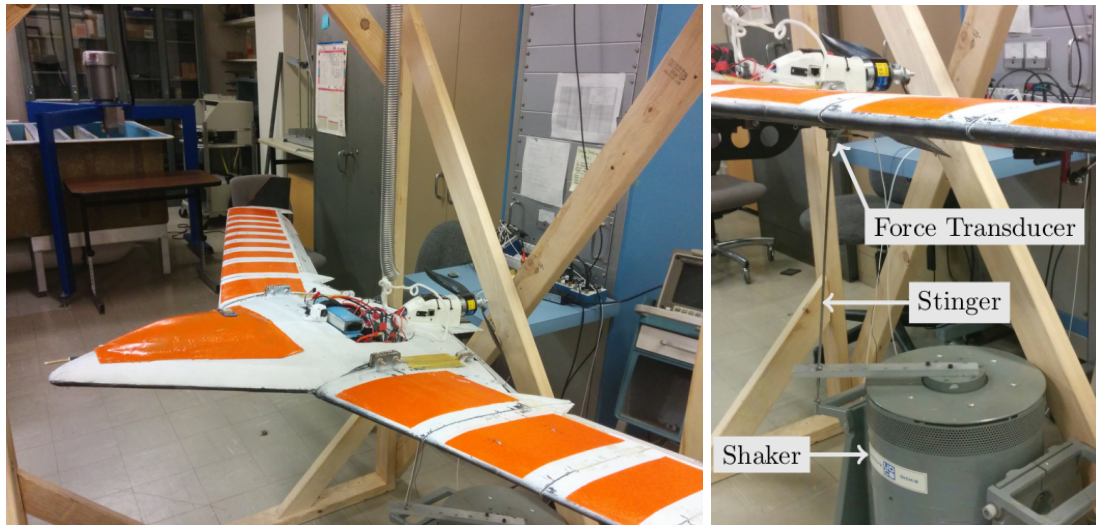
Figure 5.5: Ground vibration test setup

The excitation force was provided using an Unholz-Dickie, model 20 electrodynamic shaker. The shaker is capable of generating more than 1100 Newtons force and has a frequency range of 1-5000 Hz. The shaker transmitted the force to the aircraft using a stinger mechanism as shown in the right part of Figure 5.5. The stinger was used as the transmission mechanism so that only the component of the force perpendicular to the planform was transmitted. This is important for a complex structure like a flexible aircraft because transverse forces might interfere with the excitation of a particular mode of interest. A force transducer was attached between the other end of the stinger and the aircraft. With this arrangement, the force transducer measured the exact force being transmitted to the aircraft via the stinger. This means that the shaker dynamics need not be modeled and taken into account. Using a stinger also ensures the force was transmitted only in the single axis measurable by the single axis force transducer. Hot glue was chosen to affix the force transducer to the aircraft so that the surface of

the aircraft did not get damaged while conducting the test.

Two excitation locations were chosen for the ground vibration test. First point was a symmetric excitation point close to the trailing edge on the longitudinal axis and the second was an asymmetric point close to the body flap. The excitation locations are labeled in figure. 5.6. The excitation points were chosen carefully so that all the symmetric and anti-symmetric bending and torsion modes are excited during the test. Accelerations were measured at twenty eight locations shown in Figure 5.6.
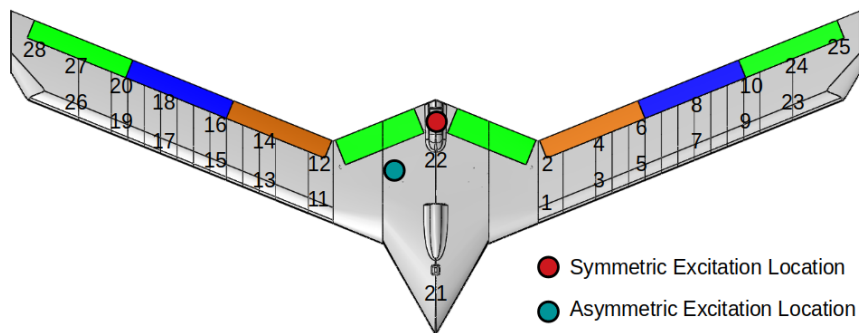
Figure 5.6: GVT input and output locations

5.3.2 Experiment Procedure

To vibrate the aircraft, a chirp signal was provided to the shaker as described in the equation below.

$$I(t) = A \sin \left(\int_0^t \big(\omega(\tau) \times \tau \big) d\tau \right) \tag{5.2}$$

where the amplitude is A, frequency at time τ is $\omega(\tau) = \omega_0 + \frac{\tau}{T}(\omega_f - \omega_0)$, initial frequency is $\omega_0 = 3$ Hz, final frequency is $\omega_f = 35$ Hz and the total duration of the signal is $T = 120$ seconds.

The frequency of the signal is increased linearly with time from 3 Hz to 35

Hz while the amplitude is kept constant. The amplitude is chosen such that the enough vibrational energy is imparted into the aircraft without exceeding the limits of the shaker. The exact value of the amplitude does not matter. A long duration of 120 seconds is chosen to ensure that sufficient excitation is provided to each frequency. The chirp input to the shaker is plotted in Figure 5.7 for the first 10 seconds.
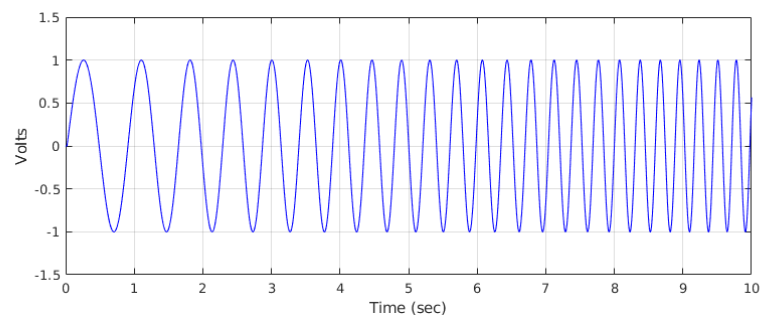
Figure 5.7: Chirp input to shaker for a duration of 10 seconds

The electrodynamic shaker generated force according to the shaker dynamics and the force was transmitted to the aircraft via a stinger. The force generated by the shaker was usually not proportional to the input provided due to the presence of shaker dynamics. The force transducer between the stinger and the aircraft measured the exact force transmitted to the aircraft. The force measured for one of the tests is shown in Figure 5.8. The difference between the input to the shaker, which had a constant magnitude, and the force transmitted to the aircraft can be clearly observed.

Only two accelerometers were available for the ground vibration tests to measure output at twenty eight locations. Therefore, the ground vibration test were conducted fourteen times for each excitation location. The accelerometers were moved to different sensor locations between each test. The acceleration measured for one of the tests is shown in Figure 5.9. This procedure was followed for both the excitation locations. Thus, finally two sets of data are collected, one for each excitation location. Each set contains one force and twenty eight acceleration
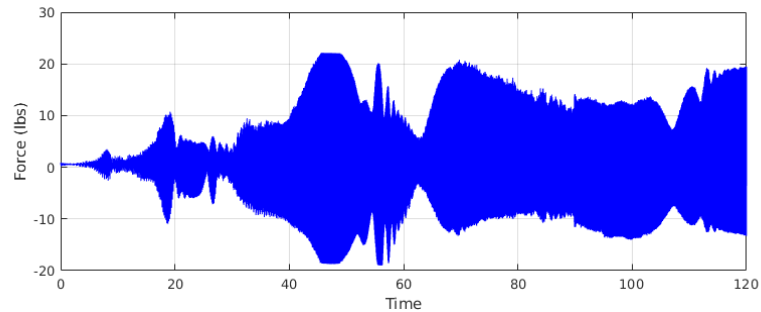
Figure 5.8: Force measured by the transducer

signals.
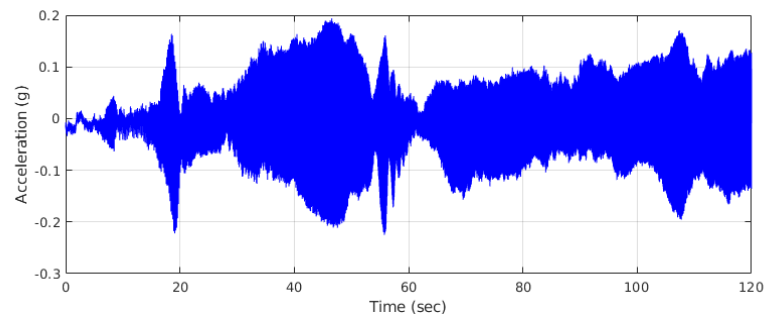
Figure 5.9: Acceleration measured by the accelerometer

A data acquisition (DAQ) system was used to collect the data during the ground vibration tests. The data acquisition system consisted of the NI-9269 signal output module to generate the chirp signal. NI-9229 voltage input module was used to log the measurement from the force transducer and two accelerometers. A sampling frequency of 2000 Hz was used, which was higher than the required nyquist frequency. These two modules are mounted on a NI cDAQ-9178 chassis. The software MATLAB was used to interface with the DAQ using the data acquisition system toolbox. The data is utilized for identification of modal parameters of the aircraft as described in the next section. The data from the GVT can also be used for other purposes like real time shape estimation of the aircraft [57].

5.4   Modal Identification

The data obtained from the GVT is in the form of time series signals consisting of input forces and output accelerations for each excitation location. The time domain data was processed to obtain frequency domain modal parameters. The modal parameters are the mode shapes and modal frequencies. These parameters were later utilized for the update and validation of the finite element model as discussed in Section 5.5.

Two different methods were employed to obtain these modal parameters from the time domain data. The first method, known as the quadrature response method, is described in Section 5.4.1. The second method is the Curve Fitting Frequency Domain Decomposition (CFDD) method and it is described in Section 5.4.2.

5.4.1   Quadrature Response Method

Consider the time series data collected for a single excitation location and 28 output locations. The data was collected in fourteen tests with accelerations measured at two locations in each test. The total duration of each experiment was $T = 120$ sec and data was collected using a sampling time of 5×10^{-4} sec (corresponding to 2000 Hz). Let $\{t_k, f_i(t_k), a_i(t_k)\}_{k=1}^{N_t}$ denote the time, force, and acceleration measurements for a single input/output pair where $N_t = 240001$. There are 28 such pairs, i.e, $i = 1, \ldots, 28$. [1]

The input force and output accelerometer signals are converted to frequency domain via the Fast Fourier Transform (FFT) using the MATLAB command `fft`. The time domain force and accelerometer signals are padded with trailing zeros to obtain signals of length $N_f = 262144$ where N_f is the next power of 2 after N_t. This is done to improve the performance of the FFT algorithm. The FFT is computed on the frequency grid $\omega_k = (2000 \times \frac{k}{N_f})$ Hz for $k = 0, \ldots, \frac{N_f}{2}$. This

---

[1]As noted previously the accelerations were measured at two points at a time but the same f_i is applied for all the measurements in a set.

yields frequency domain data $\{\omega_k, F_i(j\omega_k), A_i(j\omega_k)\}_{k=0}^{N_\omega}$ for $i = 1, \ldots, 28$ where $N_\omega = \frac{N_f}{2} = 131072$. The frequency response function for the ith input/output pair is given by:

$$G_i(j\omega_k) := \frac{A_i(j\omega_k)}{F_i(j\omega_k)} \tag{5.3}$$

This yields frequency response functions $\{G_i(j\omega_k)\}_{k=0}^{N_w}$ for $i = 1, \ldots, 28$ for one excitation point and the twenty eight measurement locations shown in Figure 5.6. Note that the frequency response functions are complex and contain both real and imaginary parts.

The modal frequencies were identified using a peak-picking approach. Let G denote the dynamics from one input excitation location to the 28 output measurement locations. The frequency response function is a 28×1 vector with the ith entry estimated as given in Equation 5.3. The maximum singular value of G at each frequency is given by:

$$\bar{\sigma}(G(j\omega)) := \sqrt{\sum_{i=1}^{28} |G_i(j\omega)|^2} \tag{5.4}$$

The quadrature response method estimates the modal frequencies from a plot of $\bar{\sigma}(G(j\omega))$ vs. ω. This is called a sigma-plot of G. Modal frequencies are identified by peaks on this sigma-plot. The frequency range for this analysis was limited to 3 Hz to 35 Hz, according to the frequency range of chirp excitation provided during GVT. The sigma plots for the symmetric and asymmetric excitation locations are shown in Figure 5.10. The modal frequencies identified by the peaks in the plots are shown in Table 5.8.

The mode shapes are identified using the procedure by Stahle and Forlifer [58]. To motivate their procedure, first consider a single degree of freedom system with
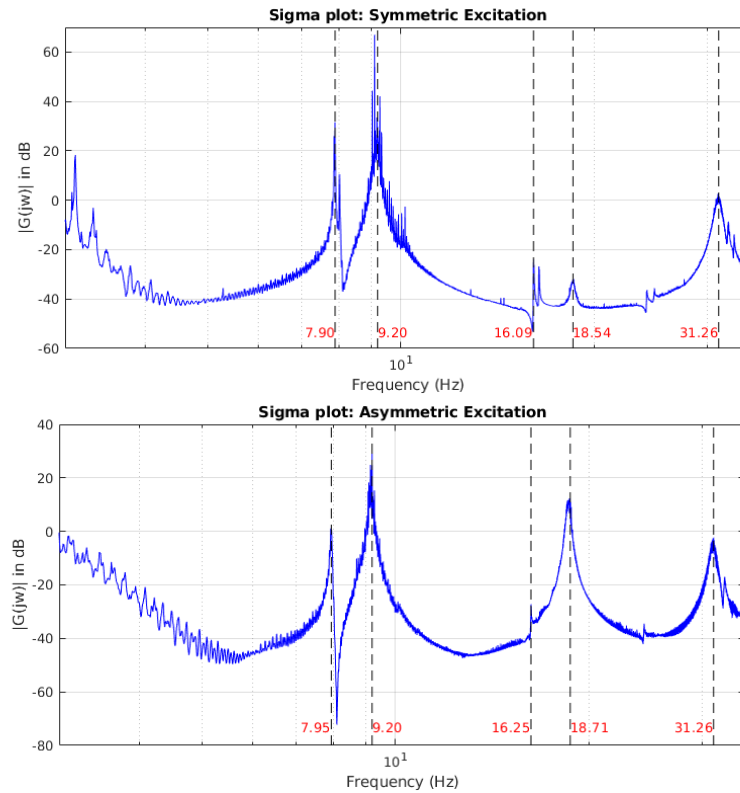
Figure 5.10: Sigma-plots for the frequency response with symmetric (top) and asymmetric (bottom) excitation locations

structural damping. The transfer function of such a system is given by:

$$G(s) = \frac{C\omega_n^2}{s^2 + 2\zeta\omega_n s + \omega_n^2} \tag{5.5}$$

where C is the zero frequency gain (DC gain), ζ is the damping coefficient and ω_n is the modal frequency of the system. The frequency response of this system can be written as:

$$G(j\omega) = \frac{C\omega_n^2}{\left(\omega_n^2 - \omega^2\right) + j\left(2\zeta\omega_n\omega\right)} \tag{5.6}$$

If the damping is small then the peak response occurs at $\omega \approx \omega_n$. Note that the

Mode #	Symmetric Hz (rad/s)	Asymmetric Hz (rad/s)	Mode shapes
1	7.90 (49.63)	7.95 (49.95)	1st symmetric bending
2	9.20 (57.80)	9.20 (57.80)	-
3	16.09 (101.09);	16.25 (102.10)	1st symmetric torsion
4	18.54 (116.49)	18.71 (117.56)	1st anti-symmetric bending
5	31.25 (196.35)	31.26 (197.41)	2nd symmetric bending

Table 5.8: Peak frequencies identified by sigma plot

response at $\omega = \omega_n$ is purely imaginary.

$$G(j\omega_n) = -j\frac{C}{2\zeta} \tag{5.7}$$

The coefficient of the imaginary part of the response is known as quadrature response and is denoted by $\text{Quad}(G(j\omega))$. Equation 5.7 shows that the response is purely imaginary at $\omega = \omega_n$. Thus for lightly damped systems, the peak gain of G and peak quadrature both occurs at $\omega \approx \omega_n$. The peak quadrature response (accounting for sign) is given by:

$$P = \text{Quad}(G(j\omega_n)) = -\frac{C}{2\zeta} \tag{5.8}$$

The frequency response function can be written in term of the peak quadrature response:

$$G(j\omega) = P\frac{-2\zeta\omega_n^2}{(\omega_n^2 - \omega^2) + j\left(2\zeta\omega_n\omega\right)} \tag{5.9}$$

The response can then be split into its real and imaginary parts as follows:

$$G(j\omega) = P\left[\frac{-2\zeta\frac{\omega}{\omega_n}\left(1 - \frac{\omega^2}{\omega_n^2}\right)}{\left(1 - \frac{\omega^2}{\omega_n^2}\right)^2 + \left(2\zeta\frac{\omega}{\omega_n}\right)^2} + j\frac{(2\zeta)^2\frac{\omega}{\omega_n}}{\left(1 - \frac{\omega^2}{\omega_n^2}\right)^2 + \left(2\zeta\frac{\omega}{\omega_n}\right)^2}\right] \tag{5.10}$$

The quadrature response can be written as

$$\mathrm{Quad}(G(j\omega)) = P \left[\frac{(2\zeta)^2 \frac{\omega}{\omega_n}}{\left(1 - \frac{\omega^2}{\omega_n^2}\right)^2 + \left(2\zeta \frac{\omega}{\omega_n}\right)^2} \right] \tag{5.11}$$

Thus, it can be concluded that for a single degree of freedom system with low structural damping, the response at resonance is purely imaginary and can be calculated as $P = -\frac{C}{2\zeta}$.

This can be easily extended to a system with multiple outputs and multiple modes. The response of ith output can be written as:

$$\mathrm{Quad}(G_i(j\omega)) = \sum_{m=1}^{M} P_{i,m} \frac{(2\zeta_m)^2 \frac{\omega}{\omega_m}}{\left(1 - \frac{\omega^2}{\omega_m^2}\right) + j\left(2\zeta_m \frac{\omega}{\omega_m}\right)} \tag{5.12}$$

where a subscript m denotes quantities corresponding to the mth mode and M is the total number of modes. Equation 5.12 states that the quadrature response at i^{th} output is a linear combination of peak quadrature responses $P_{i,m}$ due to each individual mode. $\mathrm{Quad}(G_i(j\omega))$ are measured during GVT, ω_m are obtained from the sigma plot and a constant modal damping can be assumed for all the modes.

The mode shape for mode m is given by the vector $v_m := [P_{1,m}, \ldots, P_{28,m}]$. All quantities in Equation 5.12 are known except for the entries of this vectors. Specifically, evaluating Equation 5.12 at the mth modal frequency ω_m yields a set of algebraic equations of the form $Av_m = b$ where b is the 28×1 vector of quadrature responses at ω_m. This set of algebraic equations can be solved for the mode shape vector v_m associated with mode m. These steps can be repeated for each desired mode shape.

This procedure is applied to the frequency response functions calculated from the GVT data. The procedure described above includes one modification to smooth the data. Specifically, the experimental quadrature response is noisy. Thus the Matlab command `fitfrd` is first used to fit each of the 28 experimental frequency responses. An example of this fitting for one frequency response

function is shown in Figure 5.11. This fitting smoothes the data and improves the quality of the estimated mode shapes. Equation 5.12 is used to calculate the mode shapes from the fitted transfer functions. The resulting mode shapes are shown in Figure 5.12 for both symmetric and asymmetric GVT.
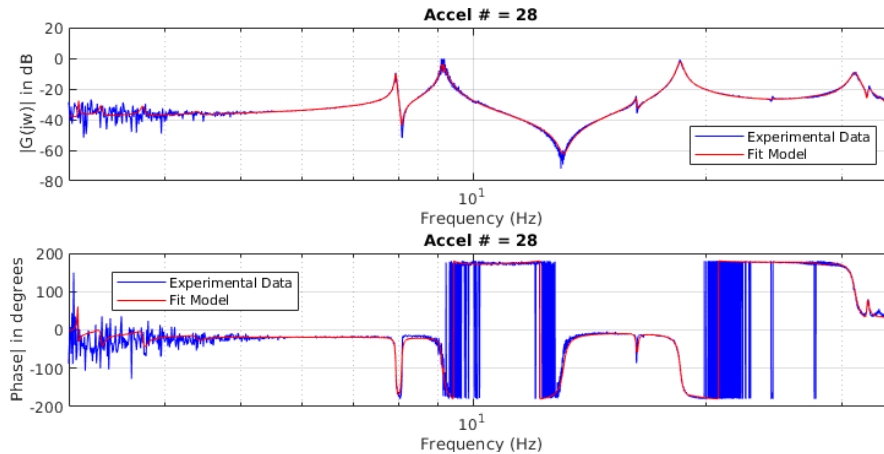
Figure 5.11: Frequency response function fit

5.4.2   Curve-Fitting Frequency Domain Decomposition

The second approach is known as Curve-fitting Frequency Domain Decomposition (CFDD). Classical approach of peak-picking from the power-spectral density diagram for identification of modal parameters [59] works reasonably well for well-separated modes. But, if the modes are closely spaced, the results can become biased [60]. The quadrature response method, described in the previous section, uses the method proposed by the Stahle and Forlifer [58] to correct for the effect of closely spaced modes for the calculation of mode shapes.

It has also been shown that the autospectra of the output signals do not provide sufficient information for the estimation of modal parameters [61]. The cross-spectra magnitude, phase and coherence also play a major role. Refs. [60, 62] proposed the use of the Singular Value Decomposition (SVD) of the power spectral-density matrix to address these issues. Specific details of the CFDD
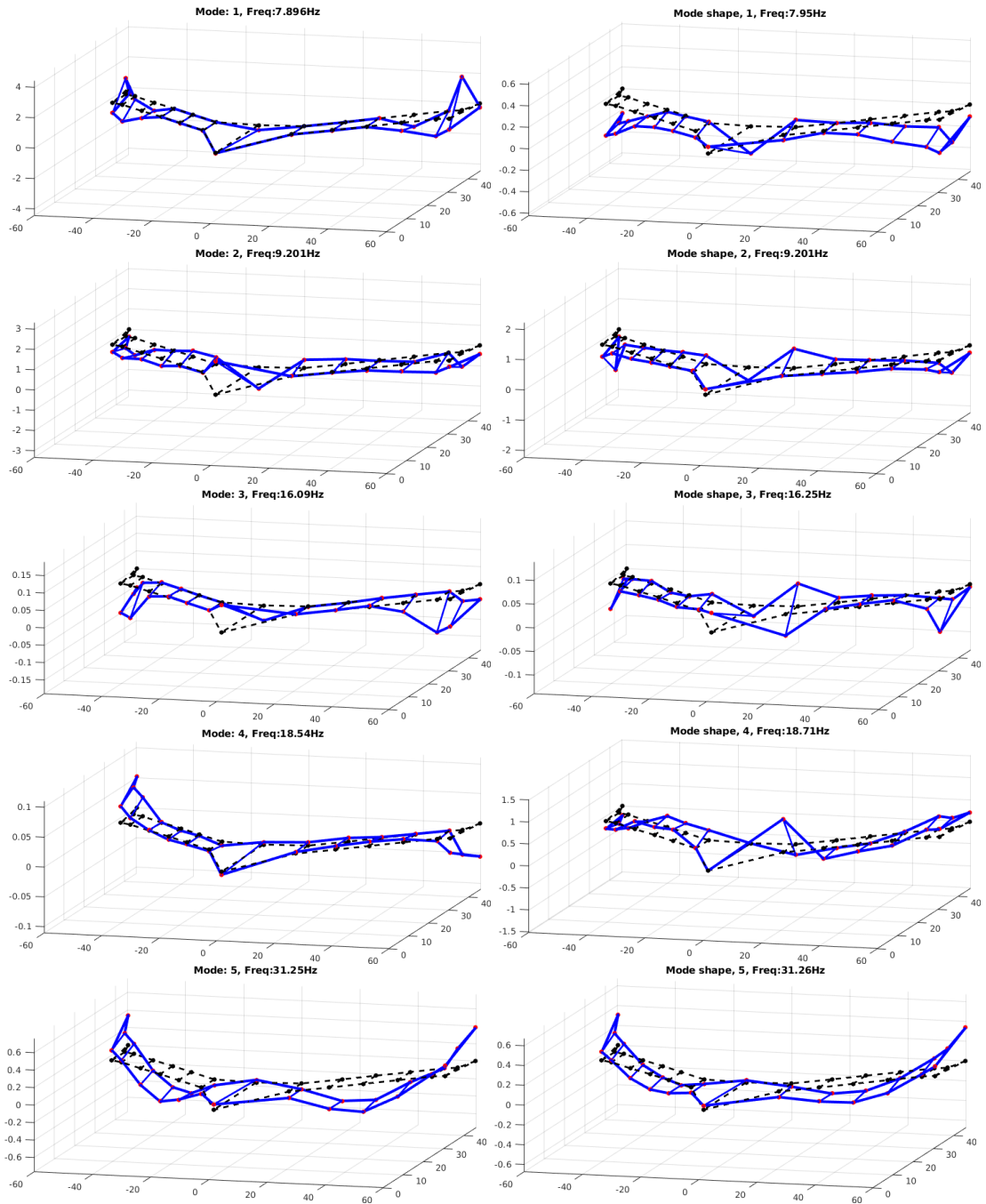
Figure 5.12: Mode shapes from symmetric (Left) and asymmetric (Right) data using quadrature response method

method and its application on extraction of modal parameters estimation from flight test data can be found in [61] and [63]

The modal identification using CFDD method was conducted by the researchers at Systems Technology Inc. and the results are shown in Table 5.9.

Mode #	Symmetric Hz (rad/s)	Asymmetric Hz (rad/s)	Mode Shape
1	7.90 (49.64)	7.94 (49.89)	1st symmetric bending
2	9.10 (57.17)	9.19 (57.74)	-
3	16.09 (101.10);	16.25 (102.10)	1st symmetric torsion
4	18.55 (116.55)	18.69 (117.43)	1st anti-symmetric bending
5	31.22 (196.16)	31.31 (197.72)	2nd symmetric bending

Table 5.9: Modal frequencies identified by CFDD method

5.4.3 Identified Modal Parameters

The quadrature response and the CFDD methods are applied to the symmetric and asymmetric GVT data. It can be seen that the results of the two methods differ slightly for some modes. For any particular mode, one of the two results is picked based on the level of excitation and clarity of the identified mode shape. Table 5.10 show the method picked for each modes.

It can be observed that the second mode with a frequency of around 9.2 Hz does not correspond to any expected mode shape. It is concluded that the effect of the asymmetry in the model is significant and this results in the splitting of the 1st symmetric bending mode into two different mode. Therefore, asymmetry was included in the next FEM update discussed in Section 5.5.

5.5 FEM Update

The modal parameters obtained from the ground vibration test were compared to the finite element model of Geri. It was observed that frequencies of the FEM

Mode #	Frequency Hz (rad/s)	Mode shape	Method used
1	7.95 (49.64)	1st symmetric bending	Quadrature response: Asymmetric
2	9.20 (57.80)	Not identified	Not identified
3	16.1 (101.10)	1st symmetric torsion	Quadrature response: Symmetric
4	18.54 (116.55)	1st anti-symmetric bending	Quadrature response: Symmetric
5	31.25 (196.16)	$2nd$ symmetric bending	CFDD: Symmetric

Table 5.10: Final identified frequencies and modes

model were different from the GVT results. A comparison of the previous FEM model results and the GVT results are shown in Table 5.11.

Mode #	GVT Frequency Hz (rad/s)	FEM Frequency Hz (rad/s)	Mode Shape
1	7.95 (49.95)	7.95 (49.95)	1st symmetric bending
2	9.20 (57.80)	12.5 (78.53)	Not identified
3	16.1 (101.10)	15.9 (99.90)	1st symmetric torsion
4	18.54 (116.55)	18.7 (117.49)	1st anti-symmetric bending
5	31.25 (196.16)	31.5 (197.92)	2nd symmetric bending

Table 5.11: Modal frequencies from GVT and FEM model updated using static test

Therefore, the FEM model was updated based on the GVT data. The FEM updated was conducted by researches at Virginia Polytechnic Institute and State University with support from the team at University of Minnesota. An sucomponent based optimization procedure is employed to update the FEM model with GVT data. The details of the update procedure and optimization results are given in [51, 64, 65] and [27]. The GVT results suggested that the aircraft exhibits significant asymmetry. Therefore, the symmetry constraint was removed while updating the FEM model. The results of the model update on the mass

and structural properties of the aircraft are discussed below.

The mass properties of the updated FEM model are shown in Table 5.12 along with the corresponding values from the previous FEM update. It can be seen that the mass properties did not change significantly.

FEM Model	Mass (kg)	x-CG location (m)	Inertia I_{xx} (kg-m^2)	Inertia I_{yy} (kg-m^2)
Updated using static test	6.25	-0.603	2.640	0.464
Updated using dynamic test	6.26	-0.603	2.648	0.463

Table 5.12: Mass and inertia properties of updated FEM model

The modal frequencies of the updated FEM model are described in Table 5.13. The modal frequencies show appreciable changes while the mode shape remained the same qualitatively. Figure 5.13 show the mode shapes from the updated FEM model.

Mode #	Static test updated Hz (rad/s)	Dynamic test updated Hz (rad/s)	Mode shape
1	7.95 (49.95)	7.81 (49.07)	1st symmetric bending
2	12.5 (78.53)	10.0 (62.83)	1st anti-symmetric torsion
3	15.9 (99.90)	14.73 (92.55)	1st symmetric torsion
4	18.7 (117.49)	19.72 (123.90)	1st anti-symmetric bending
5	31.5 (197.92)	32.44 (203.83)	2nd anti-symmetric torsion

Table 5.13: Modal frequencies from static and dynamic test updated FEM model
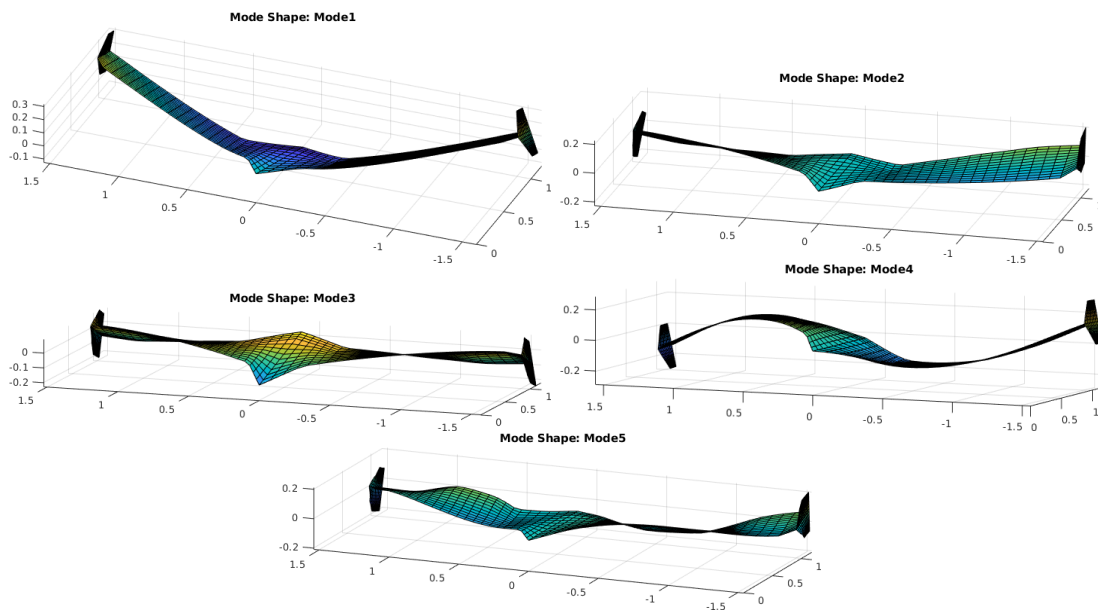
Figure 5.13: Mode shapes from updated FEM model

Chapter 6

Aerodynamic Model

The aerodynamic model is an essential subcomponent of the flight dynamics model of an aircraft. It is used to calculate the forces acting on the aircraft due to the airflow around it. Modeling the aerodynamic forces generated on a flexible aircraft is significantly more challenging than a rigid aircraft. This is because the flexible aircraft changes its shape during flight, thus, changing its aerodynamic properties. This chapter describes the panel method based models used to calculate the steady and unsteady aerodynamic forces acting on the aircraft. These panel methods are further modified to capture the geometrically nonlinear effects on the aerodynamic forces due to the flexibility of the aircraft.

6.1   Introduction

The Navier-Stokes equations [66] are a set of partial differential equations which form the basis of all fluid flows. The interaction of the flow with any surface or body is captured by the boundary condition of the equations. The Navier-Stokes equations can also be used to calculate the forces generated on any such surface or body interacting with the flow. The general form of the Navier-Stokes equations include the compressibility and viscosity effects on the fluid flow.

In general, the fluid dynamics described by the Navier-Stokes equations are

highly nonlinear. This is known as *aerodynamic nonlinearity.* If the flow can be assumed to be incompressible and non-viscous, the equations can be simplified. For example, the fluid flow around a low speed UAV operating in standard atmospheric conditions can be assumed to be incompressible and non-viscous. Such flow are aerodynamically linear. Potential flow theory is used to model the flow under these simplifying assumptions.

An important characteristic of the aerodynamics of a flexible aircraft is that the aerodynamic properties are time varying. Specifically, as the shape of the flexible aircraft changes during flight with time, its aerodynamic properties and the airflow around the aircraft change with time as well. Therefore, both steady and unsteady aerodynamics forces are generated on the aircraft. The change in flow characteristics takes place in a finite amount of time and is not instantaneous. This lag needs to be taken into account in the unsteady aerodynamic model. For a flexible aircraft, the relationship between the changes in the aircraft jig shape and the changes in the aerodynamic properties is nonlinear. This phenomena is another source of nonlinearity in the aerodynamic model known as *geometric nonlinearity.* It should be noted that the geometric nonlinearity due to the flexibility of the aircraft is different from the previously described aerodynamic nonlinearity which is present in both rigid and flexible aircraft in general.

There are several well known methods that can be used model the steady and the unsteady aerodynamics of a flexible aircraft [34, 67, 68]. For example, Computational Fluid Dynamics (CFD) based methods can be used where the equations of the fluid flow are implemented numerically by discretizing the flow domain [66]. Similarly, Computational Structural Dynamics (CSD) based models can capture the structural dynamics of a flexible aircraft. CFD and CSD models can be combined to calculated the flexible deflection and the time varying aerodynamic forces on a flexible aircraft. These methods are usually resource intensive but produce high fidelity results. CFD-CSD methods yield models with a large number of states, which makes them unsuitable for control-oriented aeroelastic modeling. On the other hand, simple potential flow based methods like strip theory have

low computational cost but produce low fidelity results. The accuracy of these low fidelity methods improve for specific cases like high aspect ratio, slender wing aircraft [69].

The focus of this work is to obtain a control-oriented model for the flight dynamics of a flexible, low-speed UAV. For this application, a reasonably accurate model can be obtained even if the aerodynamic nonlinearities are ignored. Potential flow based panel methods are suitable for modeling the aerodynamics of the aircraft in this case. These methods are capable of handling fairly complex geometry including swept back wings, movable control surfaces and winglets etc. These methods are also capable of capturing the effect of tip vortices and the wake. The vortex lattice method (VLM) [66] is a panel method used to model the steady aerodynamic forces while the double lattice method (DLM) [31] is used to model the unsteady aerodynamic forces. The disadvantage of these potential based panel methods compared to high fidelity CFD based methods is that they are not capable of modeling the parasitic drag. This implies that these methods are not suitable for analysis of the performance of an aircraft. However, these methods can model the induced drag which is important for flight dynamics modeling and flutter analysis. As the work presented here focuses of the control oriented flight dynamics of a flexible aircraft and not on performance assessment, the panel methods are considered suitable.

The panel based methods used to model the aerodynamics of the flexible aircraft are described next. A basic description of the vortex lattice method used to model the steady aerodynamic forces is given in Section 6.2. The VLM is further modified to include the geometrically nonlinear effects of the flexibility of the aircraft. These modifications are discussed in Section 6.3. The doublet lattice method used to model the unsteady aerodynamic forces is described in Section 6.4.

6.2   Vortex Lattice Method

The Vortex Lattice Method (VLM) is a numerical, panel based method used to model the steady aerodynamic forces on a collection of lifting surface. Modeling a lifting surface (or a collection of surfaces) in a fluid flow using the VLM involves the following steps [68].

1. The surfaces are divided into a lattice of trapezoidal panels. The two parallel edges of the panels should be aligned with the direction of the fluid flow.

2. A horseshoe vortex of unknown strength is placed on each panel with bound section of the vortex on the 1/4 chord line.

3. The 3/4th point of the middle chord of the panel is considered as the collocation point for the panel. Zero normal flow boundary conditions are satisfied on these collocation points. The strengths of the horseshoe vortices are determined by the satisfying the boundary condition equations.

4. The force acting on each panel is calculated based on the strength of the horseshoe vortices and external flow properties.

These steps are demonstrated for a simple, swept-back lifting surface. The surface is shown in Figure 6.1. The surface is immersed in free stream flow with a constant velocity of V_∞ at an angle of attack α as shown in Figure 6.2. Sideslip is not considered in this example, i.e. $\beta = 0$.

The first step in the VLM implementation is to divide the surface into trapezoidal panels as shown in Figure 6.3. The two parallel edges of each trapezoid must be aligned with free stream flow direction as shown.

The second step in the VLM is to attach a horseshoe vortex of unknown strength to each panel. One such horseshoe vortex is shown in Figure 6.4. The horseshoe vortex is attached to the panel at the quarter-chord line. Specifically, the chord at any span location on the panel is a straight line connecting the leading to the trailing edge at that span. The quarter-chord line is the locus of the 1/4th
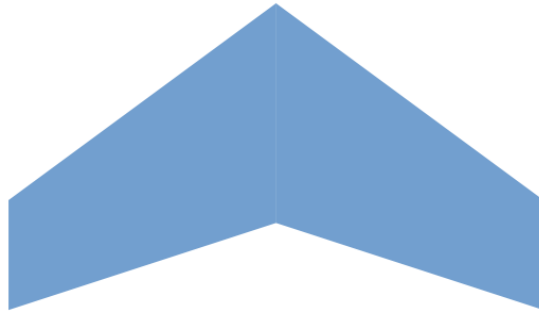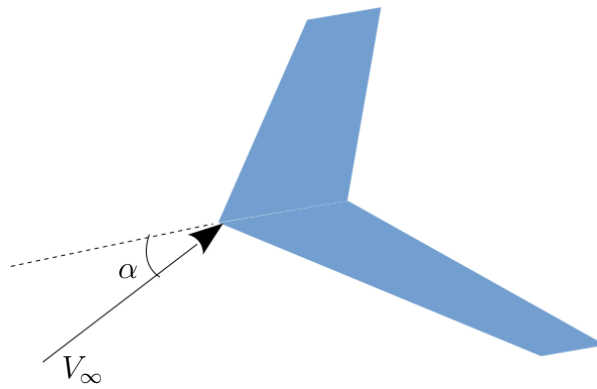
Figure 6.1: Example lifting surface

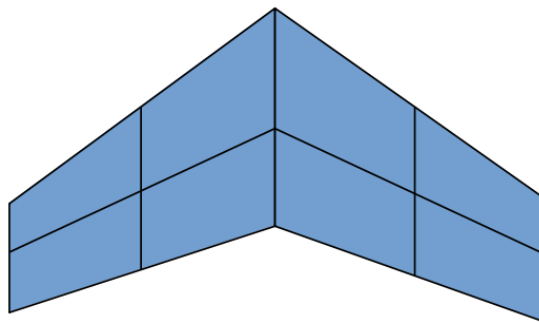Figure 6.2: Lifting surface in a free stream flow

Figure 6.3: Discretization of surface into trapezoidal panels

location of all the chords of the panel. Note that for a trapezoidal panel, this is a straight line. The unbounded parts of vortices are assumed to be parallel to the

left and right edges of the panel. Similar horseshoe vortices are placed on all the panels. Note that, in general, different panels can have different orientations.
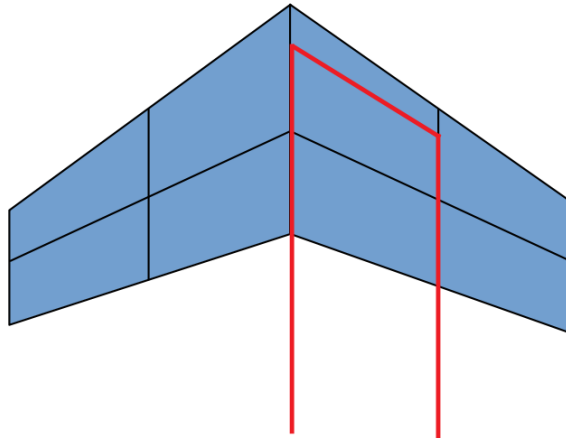

Figure 6.4: Horseshoe vortices

The third step of the VLM is to satisfy the zero normal flow boundary condition at the collocation points of the panels to calculate the strength of the horseshoe vortices. This step involves the calculation of the induced velocity due to the horseshoe vortices at the collocation points. The collocation point for each panel is located at the center (midpoint) of the 3/4th chord line for the panel. The Biot-Savart law is utilized for this computation. The law is explained in the appendix of this chapter in Section 6.5.1. It can be used to calculate the velocity induced by a horseshoe vortex at any point, as described in Equation 6.44.

The specific application of Equation 6.44 for the given aerodynamic grid is briefly summarized here. Consider the horseshoe vortex corresponding to the nth panel as shown in Figure 6.5. The strength of the vortex is denoted as $\mathcal{T}_n$. The vector $\vec{r}_n$ denotes the bound part of the horseshoe vortex. Magnitude of $\vec{r}_n$ is the length of the bound part of the vortex and its direction is aligned with the direction of the vortex. The center of the bound part of the horseshoe vortex for the nth panel is denoted as A_n. The collocation point of the mth panel is denoted as C_m.

The velocity induced by this horseshoe vortex at the collocation point C_m of
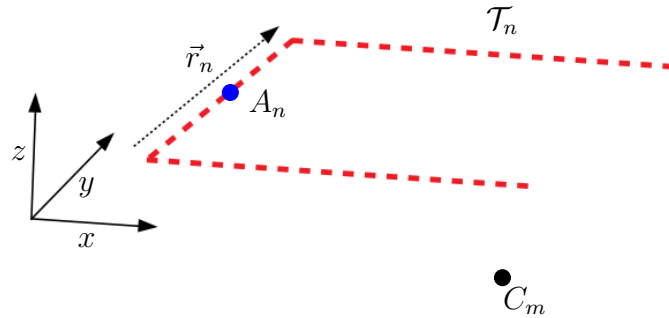
Figure 6.5: Collocation point C_m of panel m and the horseshoe vortex on panel n

the mth panel can be written as follows:

$$\vec{V}_{m,n} = \vec{Q}_{m,n}\,\mathcal{T}_n \tag{6.1}$$

Note that all the vectors are represented in the coordinate system shown in Figure 6.5. Equation 6.1 is applied to compute the induced velocity at the collocation point of m_{th} panel due to all the P vortices as:

$$\vec{V}_{\text{ind},m} = \sum_{n=1}^{P} \vec{Q}_{m,n}\mathcal{T}_n \tag{6.2}$$

Equation 6.2 can be used to compute the component of the induced velocity normal to the panel as shown in Equation 6.3.

$$\begin{aligned} w_{\text{ind},m} &= \hat{n}_m \cdot \vec{V}_{\text{ind},m}. \\ &= \sum_{n=1}^{p} (\hat{n}_m \cdot \vec{Q}_{m,n})\,\mathcal{T}_n \end{aligned} \tag{6.3}$$

where $\hat{n}_m$ is the normal vector to the panel surface. Next, we define the scalar $D_{m,n}$ as:

$$D_{m,n} = \hat{n}_m \cdot \vec{Q}_{m,n} \tag{6.4}$$

Thus, Equation 6.3 can be written as a scalar equation:

$$w_{\text{ind},m} = \sum_{n=1}^{p} D_{m,n}\, \mathcal{T}_n \tag{6.5}$$

Similarly, the normal velocity at the collocation point due to external free stream flow can be written as:

$$w_{\text{ext},m} = \hat{n}_m \cdot \vec{V}_\infty \tag{6.6}$$

where $\vec{V}_\infty$ is the freestream flow velocity expressed in the coordinate system shown in Figure 6.5.

The total normal flow at the collocation point of the m_{th} panel comprises of the normal flow due to the free stream and induced flow due to the horseshoe vortices. Using equations 6.5 and 6.6, the total normal flow velocity at the collocation point can be written as:

$$\begin{aligned} w_m &= w_{\text{ext},m} + w_{\text{ind},m} \\ &= w_{\text{ext,m}} + \sum_{n=1}^{P} D_{m,n}\mathcal{T}_n = 0 \end{aligned} \tag{6.7}$$

Equation 6.7 can be stacked for all the panels to obtain the matrix equation

$$\begin{aligned} w &= w_{\text{ext}} + w_{\text{ind}} \\ &= w_{\text{ext}} + D\mathcal{T} = 0 \end{aligned} \tag{6.8}$$

where w, w_{ext} and w_{ind} are P-by-1 vectors containing the total, external and induced normalwash at the P panels, D is a P-by-P matrix whose elements are $D_{m,n}$ and $\mathcal{T}$ is a P-by-1 vector containing the strength of the horseshoe vortices

of the P panels. Thus, the strength of the vortices can be calculated as:

$$
\begin{aligned}
\mathcal{T} &= \begin{bmatrix} -D^{-1} \end{bmatrix} w_{ext} \\
&= [\text{AIC}]\, w_{ext}
\end{aligned}
\tag{6.9}
$$

Here, we denote the matrix $[-D^{-1}]$ as the Aerodynamic Influence Coefficient (AIC) matrix. The AIC matrix is a property of the geometry of the aircraft and is used for calculation of the aerodynamic forces based on the external flow conditions as described next.

The fourth step is to calculate the force generated on each panel. Kutta-Joukowski theorem is utilized for this step and is described in the appendix of this chapter in Section 6.5.2. Using the theorem, the force generated on the nth panel can be written as:

$$
\vec{F}_n = \rho \mathcal{T}_n \left(\vec{V}_\infty \times \vec{r}_n \right)
\tag{6.10}
$$

Note that any force generated on the the two semi-infinite vortices cancel each other. Therefore, only the finite section of the vortex is taken into account in this step. This finite section is described by the vector $\vec{r}_n$ in Figure 6.5.

For the simple example of a planar wing discussed here, the resulting force lies in the z direction i.e normal to the surface. Therefore, the z component of the force can be written as a scalar equation as:

$$
F_{z,n} = \rho \left(\vec{V}_\infty \times \vec{r}_n \right)_z \mathcal{T}_n
\tag{6.11}
$$

Not that $(\vec{V}_\infty \times \vec{r}_m)_z$ is the scalar z component of the vector $(\vec{V}_\infty \times \vec{r}_m)$. Equation 6.11 can be stacked for all the panels as

$$
F_z = M_z\, \mathcal{T}
\tag{6.12}
$$

where, F_z is a P-by-1 vector of the z component of the forces on acting on the

panel, M_z is a P-by-P diagonal matrix whose n^{th} diagonal element is $\rho\,(\vec{V}_\infty \times \vec{r}_n)_z$. This formulation can be easily extended to a non-planar lifting surface where F_x and F_y can be included in Equation 6.12.

Equation 6.9 and 6.12 can be combined to write the panel forces in terms of the AIC matrix and external normalwash.

$$F_z = \big(M_z[AIC]\big)w_\text{ext} \tag{6.13}$$

Thus, it can be seen that the vortex lattice method can be used to calculate the aerodynamic forces based on external flow conditions and the panel orientations as w_{ext} is a P-by-1 vector whose m^{th} element is $\hat{n}_m \cdot V_\infty$.

The process of calculating aerodynamic forces using the vortex lattice method is summarized in Figure 6.6. For a given aerodynamic grid, the external normalwash w_ext is calculated using the external flow parameters and panel orientations. The AIC matrix is computed based on the geometry of the aircraft. The AIC matrix is used to calculate the strength of the horseshoe vortices $\mathcal{T}$. The vortex strengths are then used to calculate the forces acting on the panels.
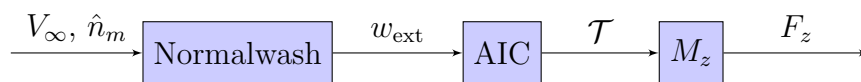
Figure 6.6: Calculation of panel forces using VLM

6.3 Modifications of VLM Formulation

The previous section described a basic, well-known implementation for the vortex lattice method. The VLM formulation has been applied extensively for rigid body flight dynamics. However, the formulation is linear and ignores both aerodynamic and geometric nonlinearities. This section describes two modifications to this basic implementation to account for: i) geometric nonlinearities, and ii) higher fidelity aerodynamic calculations, e.g. the use of local velocity for force calculation instead

of the freestream velocity V_∞. The second modification is needed for induced drag calculation. The first modification is new and is a contribution of this thesis. The second modification is known but typically not implemented. The higher fidelity aerodynamics (as provided by modification ii) is required for the inclusion of the geometric nonlinearities (modification i). These modifications enable a deeper study of the flight dynamics and flutter characteristics of low-speed speed UAV. A study of the effects of including these phenomena on flight dynamics model and flutter characteristics of the flexible aircraft Geri is presented later in Chapter 7.

The first step of the implementation of the VLM is discretization of the lifting surfaces into panels. This step is not modified and remains the same as described in the previous section. The aircraft Geri is discretized into 888 panels. The top view and the side view of discretized surfaces are shown in Figure 6.7
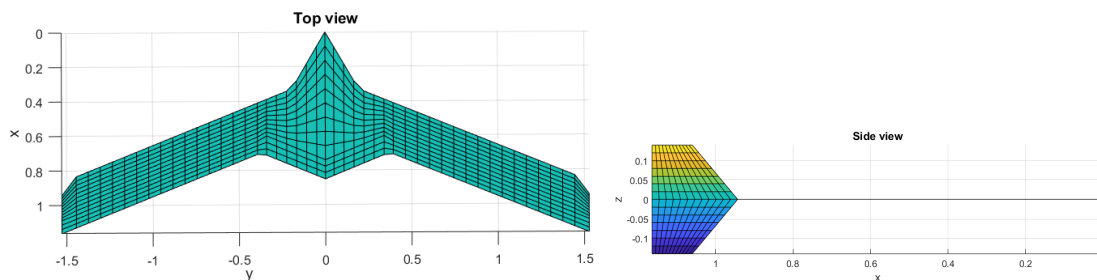
Figure 6.7: Discretization of Aircraft Geri

The second step is to attach horseshoe vortices of unknown strength to the aerodynamic panels. This step remains unchanged as well. The third step of VLM involves satisfying the zero normal flow boundary condition at the collocation points of the panels. The total normal flow at the collocation points are calculated as the sum of the normalwash due to external freestream flow and the normalwash induced by the horseshoe vortices.

The normalwash due to external flow for the basic VLM formulation has been described in Equation 6.6 in the previous section. The external flow observed by each panel was assumed to be freestream flow velocity $\vec{V}_\infty$. This can be modified

to take into account the flow due to rotation of the aircraft, flexible deflection and flexible velocity. Therefore, instead of $\vec{V}_\infty$ in Equation 6.6, we use the following for the external flow velocity on m^{th} panel.

$$\vec{V}_{ext,m} = \vec{V}_\infty - \vec{\omega}_b \times (\vec{r}_{m,c} + \vec{r}_{m,f}) - \dot{\vec{r}}_{m,f} \tag{6.14}$$

were $\vec{V}_{ext,m}$ is the total velocity at the collocation point of the mth panel, $\vec{\omega}_b$ is the angular velocity of the mean axes, $\vec{r}_{m,c}$ is the position vector of the collocation point of the mth panel in the undeformed position from the CG of the undeformed aircraft, $\vec{r}_{m,f}$ and $\dot{\vec{r}}_{m,f}$ are the flexible deflection and velocity of the mth panel in the mean axes. The flexible deflections and velocities can be written in terms of flexible mode shapes and modal deflections as:

$$\vec{r}_{m,f} = \sum_{k=1}^{n_{modes}} \vec{\phi}_{m,k}^{trans} \eta_k \tag{6.15}$$

$$\dot{\vec{r}}_{m,f} = \sum_{k=1}^{n_{modes}} \vec{\phi}_{m,k}^{trans} \dot{\eta}_k \tag{6.16}$$

where n_{modes} is the number of structural modes included in the model, $\vec{\phi}_{m,k}^{trans}$ is a 3-by-1 vector containing the deflections of the translational degrees of freedom along the x, y and z axes of the mth panel for the kth mode shape, η_k is modal deflection vector for k^{th} mode. The mode shapes and modal deflections are described in Chapter 5. These equations essentially express the flexible deflection and flexible velocity of the aircraft as a superposition of n_{modes} structural modes.

Another aspect of flexible aircraft is that the panel orientations change as the aircraft deforms. This changes the direction of the normal vector of the panels. Control surface deflections also cause a change in the normal vectors of the panels corresponding to those surfaces. The effect of the flexible deflections and control surface deflections are taken into account separately.

The flexible deflections are assumed to be small and can be described as a superposition of n_{modes} structural modes. Therefore, the dependence of the normal

vectors on the flexible deflection can be assumed to be linear. The normal vector of the mth panel for the deformed aircraft can be calculated as:

$$\hat{n}_{flex,m} = \hat{n}_{m,0} + \sum_{k=1}^{n_{modes}} \vec{N}_{m,k}\,\eta_k \tag{6.17}$$

where $\hat{n}_{m,0}$ is the 3-by-1 normal vector of the mth panel in for the undeformed aircraft, $\vec{N}_{m,k}$ is a 3-by-1 vector which describes the change in the normal vector of the mth panel due to the kth mode and η_k is the modal deflection of kth mode. $\vec{N}_{m,k}$ can be calculated as the cross product of the rotational degrees of freedom of the kth mode shape and the undeformed normal vector of the mth panel as:

$$\vec{N}_{m,k} = \vec{\phi}_{m,k}^{\text{rot}} \times \hat{n}_{m0} \tag{6.18}$$

where $\vec{\phi}_{m,k}^{\text{rot}}$ is a 3-by-1 vector containing the deflections of the rotational degrees of freedom along the x, y and z axes of the mth panel for the k_{th} mode shape.

$$\vec{\phi}_{m,k}^{\text{rot}} = [\phi_x, \phi_y, \phi_z]'_{m,k} \tag{6.19}$$

The normal vectors of the panels corresponding to the control surfaces rotate due to control surface deflections. This control surface deflection angle cannot be assumed to be small. The normal vectors of these panels are calculated using a rotation matrix. The rotation matrix for the ith control surface can be calculated as shown in Equation 6.20. Note that the rotation matrix is a nonlinear function of the control surface deflection angle.

$$R_i = \begin{bmatrix} C_i + u_{i,x}^2(1 - C_i) & u_{i,x}u_{i,y}(1 - C_i) - u_{i,z}S_i & u_{i,x}u_{i,z}(1 - C_i) + u_{i,y}S_i \\ u_{i,y}u_{i,x}(1 - C_i) + u_{i,z}S_i & C_i + u_{i,y}^2(1 - C_i) & u_{i,y}u_{i,z}(1 - C_i) - u_{i,x}S_i \\ u_{i,z}u_{i,x}(1 - C_i) - u_{i,y}S_i & u_{i,z}u_{i,y}(1 - C_i) + u_{i,x}S_i & C_i + u_{i,z}^2(1 - C_i) \end{bmatrix} \tag{6.20}$$

where the deflection the ith control surface is denoted as θ_i, cosine of θ_i is denoted as C_i, sine of θ_i is denoted as S_i and the direction cosines of the axis of rotation for the ith control surface is denoted as $[u_{i,x}, u_{i,y}, u_{i,z}]'$. It should be noted that only the normal vectors of the panels which belong to the control surfaces are modified. Therefore, the resulting normal vectors can be calculated as:

$$\hat{n}_m = \begin{cases} R_i\, \hat{n}_{m,flex} & \text{if } m \in \text{panels of } i^{th} \text{ control surface} \\ \hat{n}_{m,flex} & \text{if } m \notin \text{panels of any control surface} \end{cases} \tag{6.21}$$

where $\hat{n}_{m,flex}$ is the normal vector of mth panel as defined in Equation 6.17.

The normalwash due to external flow at each panel can be obtain by taking the dot product of the external flow velocity at the collocation point and the deformed normal vector. Equation 6.14 and 6.21 are used to obtain the normalwash due to external flow.

$$w_{ext,m} = \hat{n}_m \cdot \vec{V}_{ext,m} \tag{6.22}$$

Note that Equation 6.22 describe the modifications to the Equation 6.6 for the basic VLM formulation described in the previous section.

For the previous formulation, the velocity induced at the mth panel due to the horseshoe vortices has been described in Equation 6.2. This expression remains the same for the current VLM formulation. The induced normalwash calculation, which utilizes the normal vector of the panel, is shown in Equation 6.3. For a flexible aircraft, the normal vector changes with the control surface deflections and flexible deflections of the aircraft as described in Equation 6.21. The induced normalwash for a flexible aircraft can be calculated based on these equations. Substituting Equation 6.21 in Equation 6.3, the following equation is obtained:

$$
w_{ind,m} =
\begin{cases}
\sum_{n=1}^{P} \left(R_i \left(\hat{n}_{m0} + \sum_{k=1}^{n_{modes}} \vec{N}_{m,k}\, \eta_k \right) \cdot \vec{Q}_{m,n} \right) \mathcal{T}_n & \text{if } m \in \text{ panels of} \\
& \quad i^{th} \text{ control surface} \\
\sum_{n=1}^{P} \left(\left(\hat{n}_{m0} + \sum_{k=1}^{n_{modes}} \vec{N}_{m,k}\, \eta_k \right) \cdot \vec{Q}_{m,n} \right) \mathcal{T}_n & \text{if } m \notin \text{ panels of} \\
& \quad \text{any control surface}
\end{cases}
\tag{6.23}
$$

Note that $w_{ind,m}$ has a linear dependence on the strength of the vortices $\mathcal{T}_n$. We define a scalar $D_{m,n}(\theta, \eta)$, similar to Equation 6.4, as:

$$
D_{m,n}(\theta, \eta) =
\begin{cases}
R_i \left(\hat{n}_{m0} + \sum_{k=1}^{n_{modes}} \vec{N}_{m,k}\, \eta_k \right) \cdot \vec{Q}_{m,n} & \text{if } m \in \text{ panels of} \\
& \quad i^{th} \text{ control surface} \\
\left(\hat{n}_{m0} + \sum_{k=1}^{n_{modes}} \vec{N}_{m,k}\, \eta_k \right) \cdot \vec{Q}_{m,n} & \text{if } m \notin \text{ panels of} \\
& \quad \text{any control surface}
\end{cases}
\tag{6.24}
$$

It should be noted that $D_{m,n}(\theta, \eta)$ explicitly depends on the rotation matrices for the control surfaces which, in turn, depend on the control surface deflections θ. They also depends on the modal flexible deflections (η) explicitly. The induced normalwash at the collocation point of the mth panel can be written in terms of $D_{m,n}(\theta, \eta)$, similar to the Equation 6.5.

$$
w_{\text{ind},m} = \sum_{n=1}^{P} D_{m,n}(\theta, \eta)\, \mathcal{T}_n
\tag{6.25}
$$

The zero normal flow boundary condition is satisfied at the collocation point of

the mth panel. The total normalwash is calculated using Equations 6.22 and 6.25.

$$
\begin{aligned}
w_m &= w_{\text{ext},m} + w_{\text{ind},m} \\
&= w_{\text{ext,m}} + \sum_{n=1}^{P} D_{m,n}(\theta, \eta)\mathcal{T}_n = 0
\end{aligned}
\tag{6.26}
$$

Equation 6.26 can be stacked for all the panels to obtain

$$
\begin{aligned}
w &= w_{ext} + w_{ind} \\
&= w_{ext} + D(\theta, \eta)\mathcal{T} = 0
\end{aligned}
\tag{6.27}
$$

where w, w_{ext} and w_{ind} are P-by-1 vectors containing the total, external and induced normalwash at the P panels, $D(\theta, \eta)$ is a P-by-P matrix whose elements are $D_{m,n}(\theta, \eta)$ and $\mathcal{T}$ is a P-by-1 vector containing the strength of the horseshoe vortices of the P panels. Equation 6.27 is similar to Equation 6.8 for the previous formulation.

Following the similar procedure as Equation 6.9, vortex strengths can be calculated.

$$
\begin{aligned}
\mathcal{T} &= \left[-D(\theta, \eta)^{-1}\right] w_{ext} \\
&= \left[\text{AIC}(\theta, \eta)\right] w_{ext}
\end{aligned}
\tag{6.28}
$$

The $\text{AIC}(\theta, \eta)$ matrix depend on θ and η due to the dependence of $D_{m,n}(\theta, \eta)$ on these parameters. If the number of panels which correspond to the control surfaces are small as compared to the total number of panels on the aircraft, the dependence of the AIC matrix on θ can be ignored to obtain Equation 6.29.

$$
\mathcal{T} = \left[\text{AIC}(\eta)\right] w_{ext}
\tag{6.29}
$$

It should be noted that the control surface deflections still significantly affect Equation 6.29 as w_{ext} are a function of $\hat{n}_m$ which, in turn, depend on θ as shown in Equation 6.21.

The fourth step is to calculate the force generated on each panel. As before, the Kutta-Joukowski theorem is utilized for this step. Aerodynamic forces acting on the panels depend on the flow velocity experienced by the finite part of the horseshoe vortices. In the previous formulation, this velocity was assumed to be the freestream velocity V_∞ as described in Equation 6.10. The formulation is modified to use the local flow velocity experienced by each vortex for the calculation of panel force instead. The local flow velocity can be written as a sum of external flow and flow due to horseshoe vortices

$$\vec{V}_{a,n} = \left(\vec{V}_\infty - \vec{\omega}_b \times (\vec{r}_{n,a} + \vec{r}_{n,f}) - \vec{r}_{n,f}\right) + \sum_{l=1}^{P} \vec{Q}_{a,l} \mathcal{T}_l \tag{6.30}$$

where $\vec{V}_{a,n}$ is the total velocity at the center of the bound vortex line of the nth panel i.e at the point A_n in Figure 6.5 , $\vec{r}_{n,a}$ is the position vector of the center of the bound vortex of the nth panel in the undeformed position, $\vec{Q}_{a,l}$ is obtained by applying the Biot-Savart law (Equation 6.44) to obtain the induced velocity at the point A_n due the the horseshoe matrix at l^{th} panel.

The force generated on the nth panel can be written as

$$\vec{F}_n = \rho \mathcal{T}_n \left(\vec{V}_{a,n} \times \vec{r}_{n,flex}\right) \tag{6.31}$$

where $\vec{r}_{n,flex}$ is the vector describing the finite part of the vortex in the deformed position. Calculation of $\vec{r}_{n,flex}$ is similar to the calculation of normal vector for the deformed aircraft as shown in Equation 6.17

$$\vec{r}_{n,flex} = \hat{r}_n + \sum_{k=1}^{n_{modes}} \vec{N}_{n,k} \, \eta_k \tag{6.32}$$

Note, this modified VLM formulation calculates the aerodynamic forces in all three direction, not just perpendicular to the lifting surface. The formulation is capable of capturing a change in the overall direction of the panel forces and therefore, induced drag can be calculated. The panel forces can then be used to

calculate the total forces and moments acting on the entire aircraft to be utilized in the flight dynamics model. The details of the implementation of this modified VLM formulation on the flexible aircraft Geri are described in Chapter 7.

6.4 Doublet Lattice Method

The previous section (Section 6.2) describes the Vortex Lattice Method (VLM) used to calculate steady forces acting on a collection of lifting surfaces. This section describes the basics of the Doublet Lattice Method (DLM) [31]. It is a panel based method used to calculate the unsteady forces on the lifting surface. Like VLM, it is capable of modeling the aerodynamics of multiple lifting surfaces with different orientations.

The DLM is frequency domain, panel method based on potential flow theory [31]. The method assumes the lifting surface is undergoing harmonic oscillations in a steady airflow. The potential flow is linear. Therefore, the pressure distribution on the lifting surface is also harmonic and has the same frequency as the oscillation frequency of the surface. The DLM calculates the frequency response from the oscillation of the surface to the pressure distribution. It should be noted that the assumptions behind the DLM do not allow for geometrically nonlinear aerodynamics. Therefore, only geometrically linear aerodynamic model is considered in this thesis.

The implementation of the DLM for a set of lifting surfaces is similar to the implementation of VLM. The surface is divided into trapezoidal panels as shown in Figure 6.3. The two parallel edges of each trapezoid must be aligned with the direction of the free stream flow. Next a doublet line is attached to the quarter chord line of each panel. This doublet line shown in Figure 6.8. Note that unlike VLM, the doublet is not in the shape of a horseshoe in this case.

Next, the normalwashes are calculated at the collocation points. The collocation points are chosen at the midpoint of the 3/4 chord as before. The normalwash induced at the collocation point of the mth panel due to the doublet of the nth
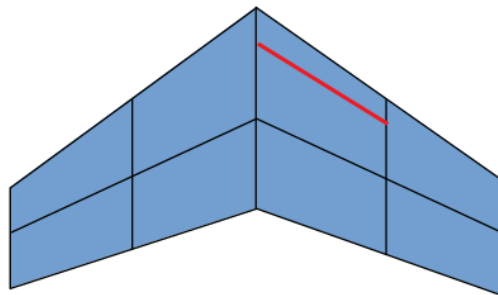
Figure 6.8: Doublet line at quarter chord

panel is given by the following equation:

$$w_{m,n} = \frac{c_n}{8\pi} \int_{-L/2}^{L/2} K(x_m, y_m, \xi_n(l), \sigma_n(l), \omega, V_\infty)\Delta p_n dl \qquad (6.33)$$

where, w_{mn} is the complex induced normalwash at m^{th} panel due to the doublet line on the nth panel, c_n is the chord length of the nth panel, K is the Kernel function which relates the complex normalwash to the complex pressure difference, x_m and y_m are the coordinates of the collocation point of the mth panel, ξ_n and σ_n are the coordinates along the doublet line of the nth panel, ω is the frequency of oscillation of the lifting surface, V_∞ is the free stream velocity, Δp_n is the complex pressure difference across the doublet line on the nth panel. The Kernel function K is described in [31]. A more detailed description including the derivation are given in [32].

Equation 6.33 can be used to evaluate the normalwash at the mth collocation point due to doublets at all P panels.

$$w_{ind,m} = \sum_{n=1}^{P} \mathcal{D}_{m,n}\Delta p_n \qquad (6.34)$$

$$\mathcal{D}_{m,n} = \frac{c_n}{8\pi} \int_{-L/2}^{L/2} K(x_m, y_m, \xi_n(l), \sigma_n(l), \omega, V_\infty)dl \qquad (6.35)$$

Here $w_{ind,m}$ is the induced normalwash at the collocation point of mth panel, $\mathcal{D}_{m,n}$ is a calculated using Equation 6.33 and Δp_n is the pressure difference across n^{th} panel. Note that Equation 6.34 is similar to Equation 6.5 obtained for VLM. The expression for $\mathcal{D}_{m,n}$ depends on the the free stream velocity and oscillation frequency. The calculation can be simplified as it can be written as a function of a single parameter κ, known as reduced frequency.

$$\kappa = \frac{\omega \bar{c}}{2V_\infty} \tag{6.36}$$

where $\bar{c}$ is the reference chord. Equation 6.34 can be stacked for the panels to obtain the matrix equation

$$w_{ind} = \mathcal{D}(\kappa)\Delta p \tag{6.37}$$

where w_{ind} is a P element vector containing the complex normalwash for all P panels, $\mathcal{D}(\kappa)$ is a P-by-P matrix whose elements are $\mathcal{D}_{m,n}$ and p is a P-by-1 vector containing the pressure differences of all panels.

w_{ind} can be calculated by satisfying the zero normal boundary flow condition at the collocation points.

$$w = w_{ext} + w_{ind} = 0$$
$$\implies w_{ind} = -w_{ext} \tag{6.38}$$

where w_{ext} is a P-by-1 vector containing the normalwash due to external flow. It depends on the orientation of the lifting surface and external flow conditions. Calculation of w_{ext} has been described previously in Equations 6.6 - 6.8. Finally, the pressure at each panel can be calculated as

$$\Delta p = \left[-\mathcal{D}(\kappa)^{-1}\right]w_{ext} \tag{6.39}$$

Here, we denote the matrix $[-D(\kappa)^{-1}]$ as the Aerodynamic Influence Coefficient (AIC) matrix. It should be noted that for DLM, the AIC matrix is defined between the pressure and the normalwash while for VLM, it is defined between the vortex

strength and the normalwash as described in Equation 6.9.

Thus, the AIC matrix for a particular reduced frequency κ can be obtained using the formulation described above. But for the calculation of unsteady aerodynamic forces, the AIC matrix for any general value of κ might be needed. Therefore, in order to calculation the AIC matrix for any value of κ, a rational function of κ is fit to a set of 7 AIC matrices. These 7 AIC matrices are calculated for $\kappa \in \{0.0469, 0.0938, 0.188, 0.375, 0.750, 1.50, 3.00\}$. These AIC matrices are fit with a rational function of the following form:

$$AIC(\kappa) = A_0 + A_1\kappa + B_1\frac{\kappa}{(\kappa + b_1)} + B_2\frac{\kappa}{(\kappa + b_2)} \tag{6.40}$$

where $b_1 = 0.11$ and $b_2 = 0.22$ are the assumed lag poles. The unknown matrices A_0, A_1, B_1, B_2 are calculated by solving the least square problem based in the linear equation shown in Equation 6.40. Note that A_0 is the steady part of the AIC matrix. As the VLM is a much better method to calculate the steady part of the aerodynamic forces, A_0 part of the AIC matrix is replaced with VLM calculation. Thus, purely unsteady part of the AIC matrix can be written as:

$$AIC(\kappa)_{\text{unsteady}} = A_1\kappa + B_1\frac{\kappa}{(\kappa + b_1)} + B_2\frac{\kappa}{(\kappa + b_2)} \tag{6.41}$$

The process of calculating aerodynamic forces using the doublet lattice method is similar to the vortex lattice method. For a given aerodynamic grid, the external normalwash w_{ext} is calculated using the external flow parameters like V_∞ and α in frequency domain. The purely unsetady AIC matrix is computed by first computing the κ and then using the rational function described in Equation 6.41. The AIC matrix is used to compute the resulting pressure in frequency domain. Once the pressure at each panel is known the resulting forces are calculated and summed with the forces calculated by the steady aerodynamic model.

The resulting forces from the steady and unsteady aerodynamic models described in this chapter can then be used for calculation of the flight dynamics

and flutter characteristics of the aircraft. The details of the implementation of the flight dynamics model, a study of the effects of unsteady forces and geometric nonlinearity and resulting flutter characteristics are discussed in the next chapter.

6.5   Appendix

6.5.1   Biot-Savart Law

Biot-Savart law [68, 30] is used to calculate the flow due to a vortex element at any location. Consider an infinitesimal filament of a line vortex of strength $\mathcal{T}$, denoted by $\vec{dl}$ as shown in Figure 6.9. The filament has a length of $|\vec{dl}|$ and is aligned to the direction of $\vec{dl}$. The flow velocity due to the vortex element at a point P with a position vector $\vec{r}$ is given by Equation 6.42.
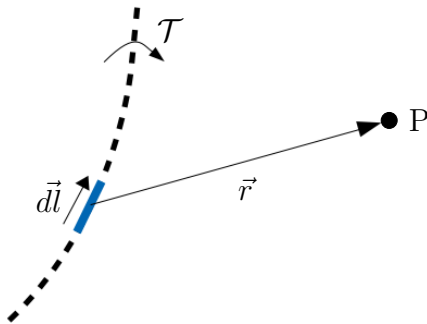

Figure 6.9: Biot-Savart law

$$d\vec{V}_p = \frac{\mathcal{T}}{2\pi} \frac{\vec{dl} \times \vec{r}}{|\vec{r}|^3} \tag{6.42}$$

The Biot-Savart law can be used to calculate the induced flow velocity due to a horseshoe vortex. Consider a horseshoe vortex of strength $\mathcal{T}$ as shown in Figure 6.10. The two vertices of the horseshoe are denoted as A and B, and the point at which the velocity is calculated is denoted as C. The coordinates of A, B and C are $(x_a, y_a, z_a), (x_b, y_b, z_b)$ and (x_c, y_c, z_c) respectively. The position vectors of C

with respect of A and B are denoted by $\vec{r_1}$ and $\vec{r_2}$ and position vector of B with respect to A is denoted by $\vec{r_0}$. The induced velocity due to an infinitesimal vortex line element is calculated and the result is integrated to obtain the induced flow due to the entire horseshoe vortex. The resulting flow is a sum of flow due to the bound part and the two semi-infinite parts of the horseshoe vortex as shown in Equation 6.43. For simplicity, it is assumed that the semi-infinite part of the vortices are aligned with the x-axis.
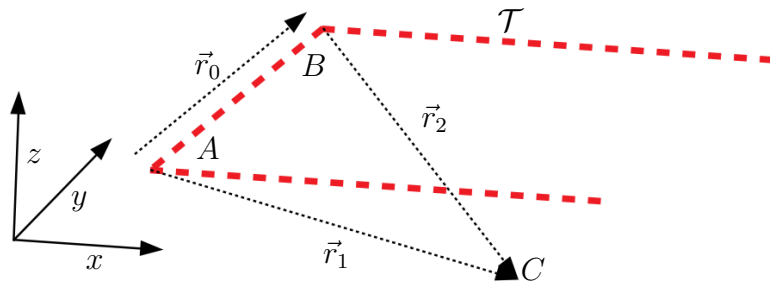

Figure 6.10: Velocity due to a horseshoe vortex

$$\vec{V_c} = \frac{\mathcal{T}}{4\pi} \frac{\vec{r_1} \times \vec{r_2}}{|\vec{r_1} \times \vec{r_2}|} \left[\vec{r_0}\cdot\frac{\vec{r_1}}{|\vec{r_1}|} - \vec{r_0}\cdot\frac{\vec{r_2}}{|\vec{r_2}|} \right]$$
$$+ \frac{\mathcal{T}}{4\pi} \left[\frac{(z_c - z_a)\hat{j} + (y_a - y_c)\hat{k}}{(z_c - z_a)^2 + (y_a - y_c)^2} \right] \left[1 + \frac{x_c - x_a}{\sqrt{(x_c - x_a)^2 + (y_c - y_a)^2 + (z_c - z_a)^2}} \right]$$
$$- \frac{\mathcal{T}}{4\pi} \left[\frac{(z_c - z_b)\hat{j} + (y_b - y_c)\hat{k}}{(z_c - z_b)^2 + (y_b - y_c)^2} \right] \left[1 + \frac{x_c - x_b}{\sqrt{(x_c - x_b)^2 + (y_c - y_b)^2 + (z_c - z_b)^2}} \right]$$

$$(6.43)$$

Equation 6.43 can be written in a compressed form as:

$$\vec{V_c} = \vec{Q}(A, B, C)\,\mathcal{T} \tag{6.44}$$

6.5.2 Kutta-Joukowski Theorem

Kutta-Joukowski theorem states that the force generated by a segment of vortex line of length vector $\vec{l}$ and strength $\mathcal{T}$ is given by the following relation.

$$\vec{F} = \rho\mathcal{T}(\vec{V}_\infty \times \vec{l}) \tag{6.45}$$

Chapter 7

Flight Dynamics Model

A brief overview of the flight dynamics modeling procedure was given in Chapter 3. Various subcomponents of the flight dynamics model like the mean axes framework, the structural dynamics model and the aerodynamics model have been described in Chapter 4, 5 and 6 respectively. These submodules and the interconnection between them are implemented in the simulation software SIMULINK to obtain the flight dynamics model. This chapter describes the details of this implementation for the flexible aircraft Geri. The flight dynamics model of Geri is available at [14] and [15] for free. The resulting flight dynamics model is analyzed and conclusions are drawn about the dependence of the flutter characteristics of the aircraft on various aerodynamic phenomena like the presence of geometric nonlinearities and unsteady aerodynamics.

The details of the implementation of the submodules in SIMULINK are given in Section 7.1. The resulting nonlinear flight dynamics model is demonstrated using a simple example. The nonlinear flight dynamics model is then linearized to obtain a control oriented state space model of the flexible aircraft. An array of linearized models for varying flight speeds are obtained and utilized to analyze the flutter characteristics of the aircraft. Section 7.2 contains the details of the nonlinear and linearized flight dynamics model. It also contains the analysis of flutter characteristics of the aircraft. Next, the effect of the presence of geometric

nonlinearities and unsteady aerodynamics on the flight dynamics model are analyzed. The details of this analysis, including the effect on flutter characteristics is described in Section 7.3.

7.1 Implementation in SIMULINK

The basic framework of the flight dynamics model was described in Figure 3.1 in Chapter 3. The framework, repeated below in Figure 7.1, shows all the submodules and the interconnection between them. The throttle command and the control surface commands are the inputs to the model. The propulsion model is used to calculate propulsion force and moment acting on the aircraft based on the throttle command. The control surface commands are used by the actuator model to calculate the control surface deflection and velocity. These are utilized by the aerodynamics model, along with the flexible states and rigid states, to calculate the forces acting on each panel of the aerodynamic grid of the aircraft. The flexible states consist of the modal deflections and modal velocities. The rigid body states are the linear velocities and the rotational orientation and velocities of the mean axes. The resulting forces on the aircraft are utilized by the rigid body dynamics and flexible dynamics to calculate the rigid body and flexible states. The sensor model is used to calculate the output of various sensors on the aircraft.

This framework is implemented in the simulation software SIMULINK as shown in Figure 7.2 to obtain the nonlinear flight dynamics model. The environment block in the figure contains the atmospheric model to calculate the air density. For the present work, the density is assumed to be constant at 1.225 kg/m^3. The details of various elements of the SIMULINK implementation are described next.
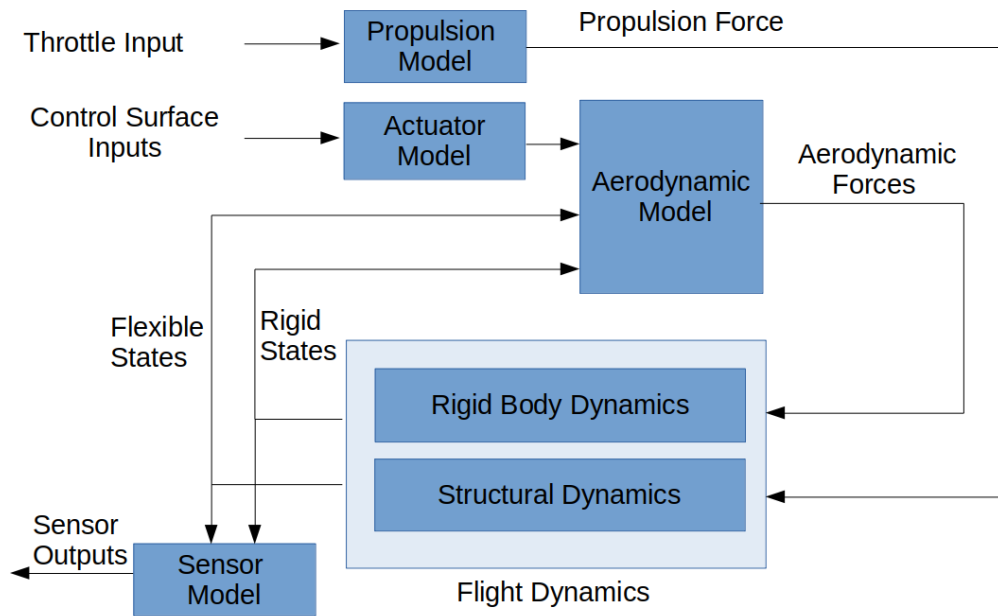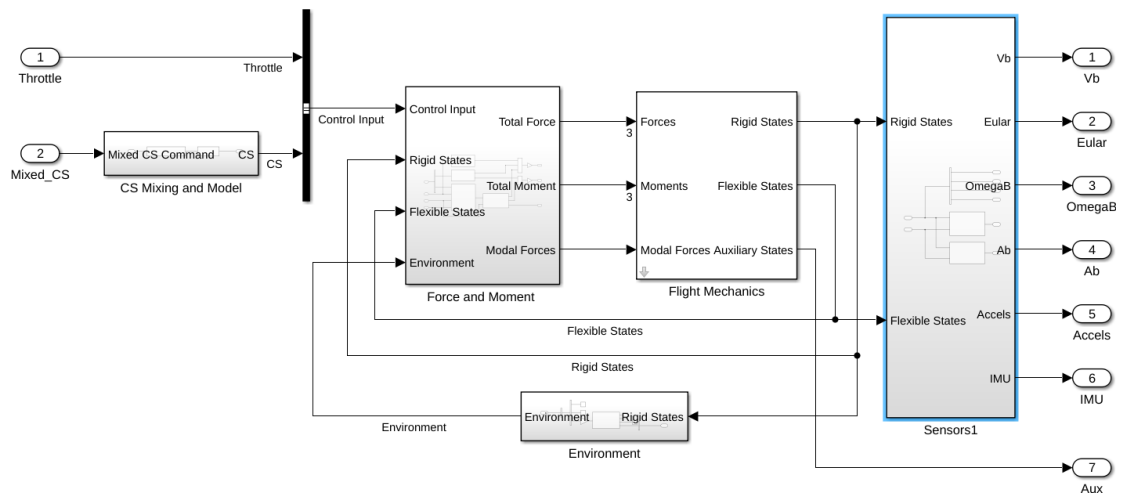
Figure 7.1: Modeling framework

Figure 7.2: SIMULINK implementation

Inputs:

The inputs to the SIMULINK model are *throttle* and *mixed control surface* commands. The throttle command assumed to be in a range of 0 to 100 where a value of 0 corresponds to no throttle and a values of 100 corresponds to full throttle. The propulsion model, described later, uses the throttle command to calculate the resulting propulsion forces and moments generated by the electric motor mounted on Geri.

The mixed control surface input commands consists of a total of eight inputs. The inputs are the symmetric and asymmetric control surface deflection commands for four pair of control surfaces as shown in Figure 2.5. For example, the first mixed control surface input, *Sym1*, corresponds to an equal deflection command to "L1" and "R1" control surfaces.

CS Mixing and Model:

The actuator model is used to calculate the resulting control surface deflections and velocities from the mixed control surface commands. The two steps involved in this calculation are described next.

First, the individual control surface commands are calculated from the mixed control surface commands. The implementation of this calculation is shown in Figure 7.3. This calculation is implemented in the *CS Mixing and Model* block in the SIMULINK implementation.
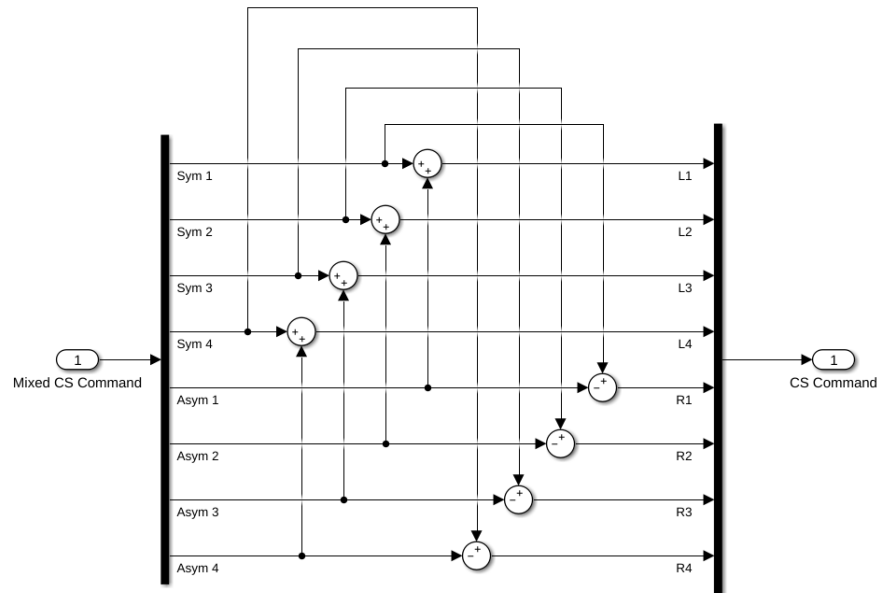
Figure 7.3: Control surface mixing

Next, a second order actuator model is implemented for the calculation of the actual control surface deflections and velocities using the individual control surface commands. The model is identified experimentally by providing chirp input to the actuator [18]. The transfer function of the actuator model is:

$$\frac{96710}{s^2 + 840s + 96710} \tag{7.1}$$

The implementation of the actuator model is shown in Figure 7.4. This implementation resides in the *CS Mixing and Model* block in SIMULINK implementation as well.
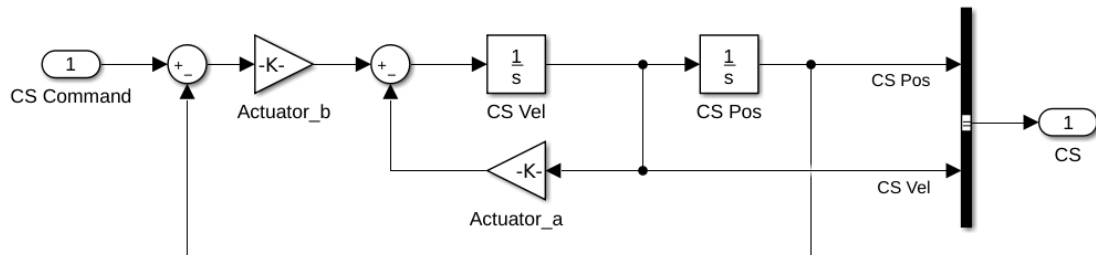
Figure 7.4: Actuator model

Forces and Moments:

The *Force and Moment* block is implemented to calculate the three types of forces and their resulting moments acting on the aircraft: propulsion forces, aerodynamic forces and gravitational forces. The block is also used to output the total forces, total moments and flexible modal forces, to be utilized by the other submodules.

Propulsion Model:

The propulsion model utilizes the throttle command to calculate the propulsive forces and moments. A simple propulsion model is utilized where the propulsion force is proportional to the throttle input. The maximum force generated by the motor is obtained from experiments conducted on the propulsion motor. A throttle value of 100 corresponds to the maximum thrust of 28.9 Newtons. The propulsion force is assumed to be oriented along the root chord of the aircraft. It generates no moments about the center of mass of the aircraft. The propulsion model is shown in Figure 7.5.
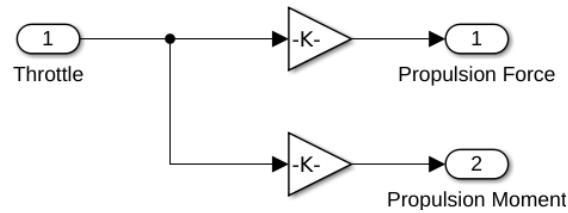
Figure 7.5: Propulsion model

Gravitation Model:

The gravitation force is calculated in the inertial frame as $\vec{F}_g = -mg\hat{k}_I$ where $\hat{k}_I$ is the unit vector along the z direction of the inertial reference frame. Note that the gravitation force acts in the $-z$ direction in the inertial frame. As the flight dynamics model utilizes the body fixed, mean axes frame; the components of the gravitational force along the mean axes are calculated. The direction cosine matrix (DCM) describing the transformation between the mean axes frame and the inertial frame is utilized for this calculation. The DCM is calculated based on the Euler angles describing the orientation of the mean axes frame. The gravitation model is shown in Figure 7.6.
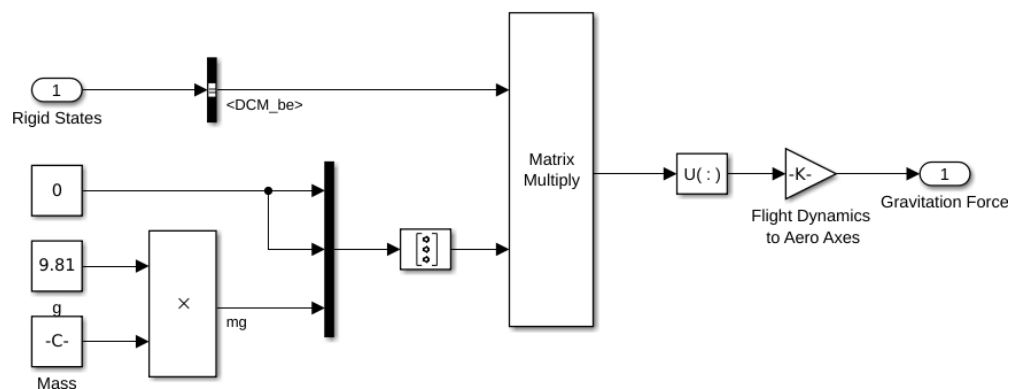

Figure 7.6: Gravitation model

Steady Aerodynamic model:

The aerodynamic model has been described in Chapter 6. The details of the steady aerodynamic model, which is a vortex lattice method modified to include

the geometric nonlinearities and to improve the fidelity, are described in Section 6.3. The implementation of the modified VLM based aerodynamic model is shown in Figure 7.7.

The block labeled *N_hat* calculates the normal vector of each panel using equation 6.17. This is described in Figure 7.8. Here the matrix labeled *Nhat_eta_all* is a $3P$-by-$(n_{modes}+1)$ sized matrix. It contains the 3 components of $\hat{n}_{m,0}$ for all the P panels as its first column and three components of $\vec{N}_{m,k}$ for all the P panels as its $(k+1)^{th}$ column. The details of this block are shown in Figure 7.8.
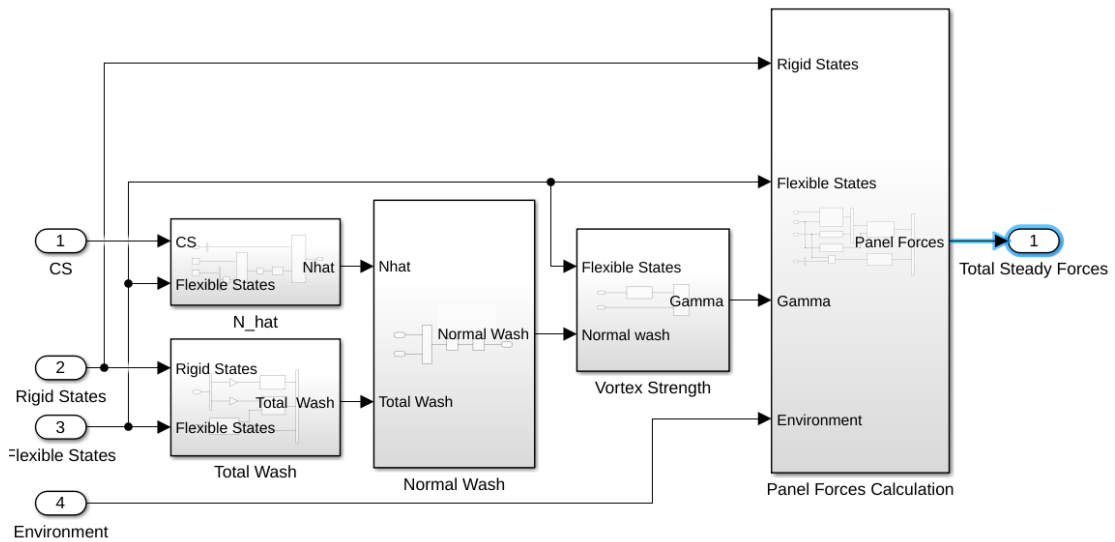

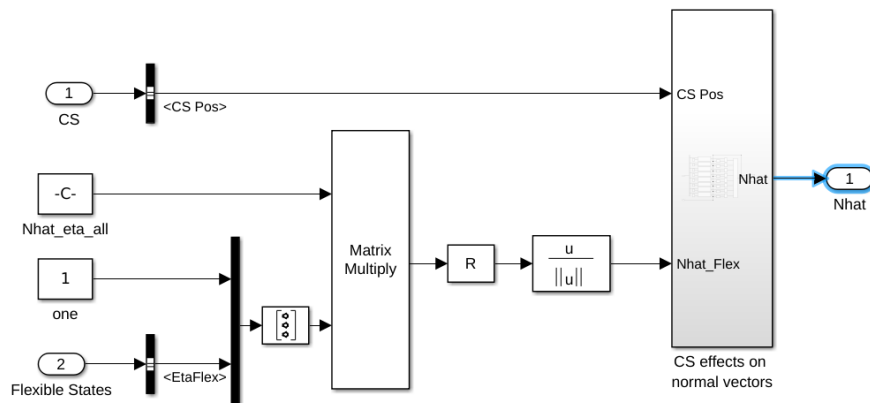
Figure 7.7: Steady aerodynamic model

Figure 7.8: Normal vector calculation

Similarly, the block labeled *Total wash* implements Equation 6.14. This is shown in Figure 7.9. The *Normal Wash* block calculates the normal wash on the panels by taking the dot product of the total wash vectors with the normal vectors. This calculation was described in Equation 6.22.
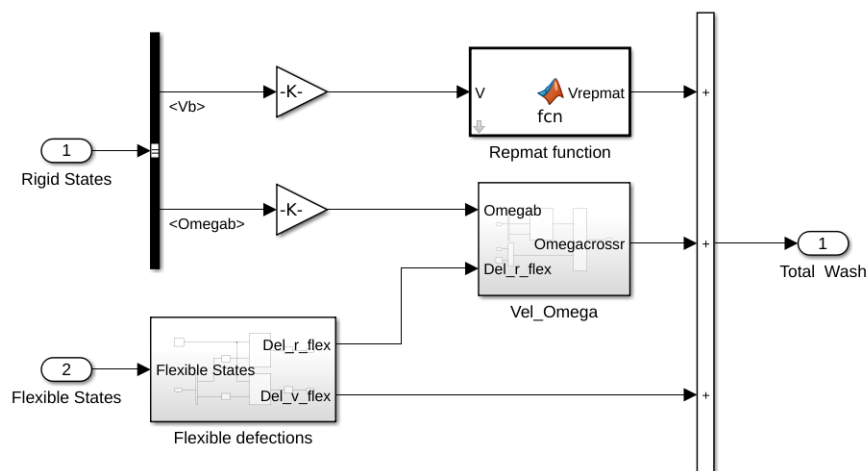

Figure 7.9: Total wash calculation

Next, the strength of the horseshoe vortices are calculated. In order to calculate the vortex strengths, Equation 6.29 needs to be implemented. The implementation requires calculation of AIC(η) at each time step. The AIC matrix is a

P-by-P matrix where P is the number of panels on the aircraft. For the aircraft Geri P is 888. Therefore, the calculation of AIC(η) using Equation 6.29 at each time step of the simulation is resource intensive. Therefore, an approximation of AIC(η) is obtained as described in the appendix in Section 7.4.1. The linear approximation of the AIC(η) matrix is:

$$[\text{AIC}(\eta)] = [\text{AIC}]_0 + \sum_{k=1}^{n_{modes}} [\text{A}_k]\eta_k \tag{7.2}$$

where $[\text{AIC}(\eta_k)]$ is the P-by-P AIC matrix for the deformed aircraft, $[\text{AIC}]_0$ is the P-by-P nominal AIC matrix for the undeformed aircraft and $[\text{A}_k]$ is P-by-P matrix describing the dependence of the AIC matrix on the k_{th} flexible mode. A_k is calculated using the Taylor series as derived in the appendix in Section 7.4.1 in Eqution 7.11.

The block labeled 'Vortex Strength' first calculates the AIC matrix using Equation 7.2 and then calculates the strengths of the horseshoe vortices. The block labeled 'Panel Forces Calculation', shown in Figure 7.10 obtains the aerodynamic force acting on each panel using the Biot-Savart law described in Section 6.5.1.
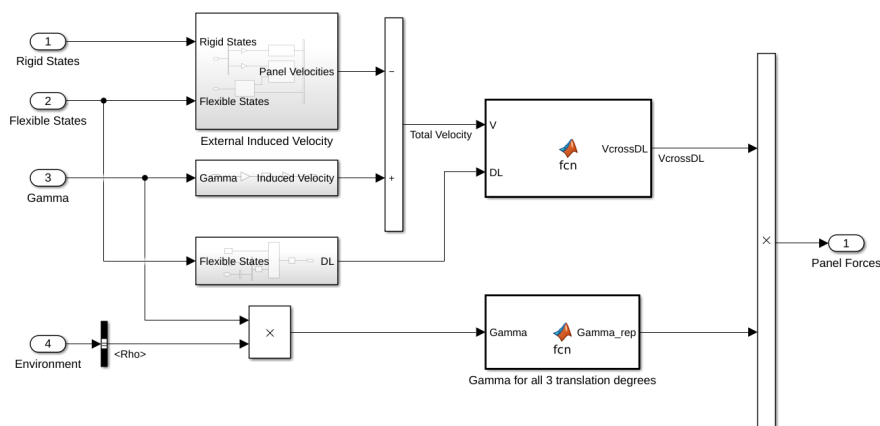

Figure 7.10: Panel force calculation

Finally, the total forces and moments acting on the aircraft are calculation in

block as shown in Figure 7.11.
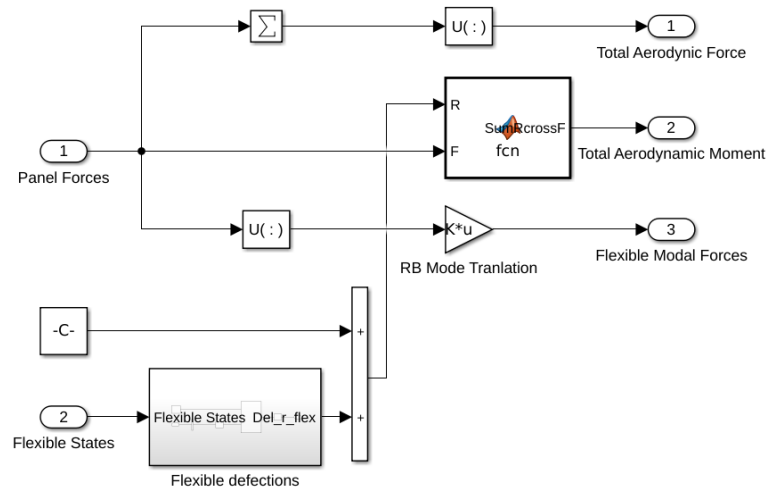
Figure 7.11: Total forces and moments calculation

Unsteady Aerodynamic model:

The unsteady aerodynamic model has been described in Chapter 6 in Section 6.4. The implementation of unsteady aerodynamic model is shown in Figure 7.12. The first two blocks in the figure are used to calculate the 'normal wash derivative', which is in turn used by the 'Normal Force' block to calculate the reduced frequency κ as described in Equation 6.36. The 'Normal Force' block also implements Equation 6.41 to calculate the AIC matrix and the resulting unsteady aerodynamic forces. The unsteady forces are summed up with the steady forces to obtain the total aerodynamic forces and moments.
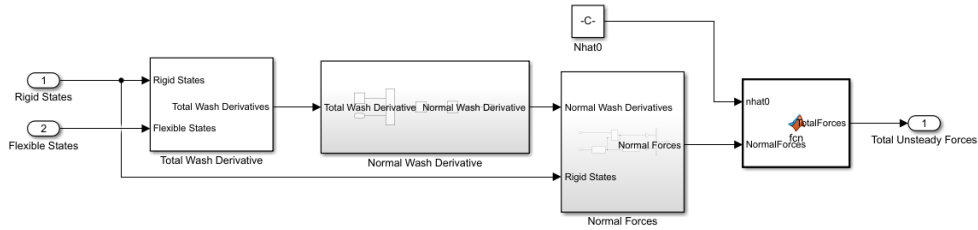
Figure 7.12: Unsteady force calculation

Flight mechanics:

The external forces acting on the aircraft are utilized by the mean axes framework based equations of motion. These equations of motion have been described in Chapter 4 in Equations 4.39, 4.40 and 4.41. The implementation is shown in Figure 7.13.
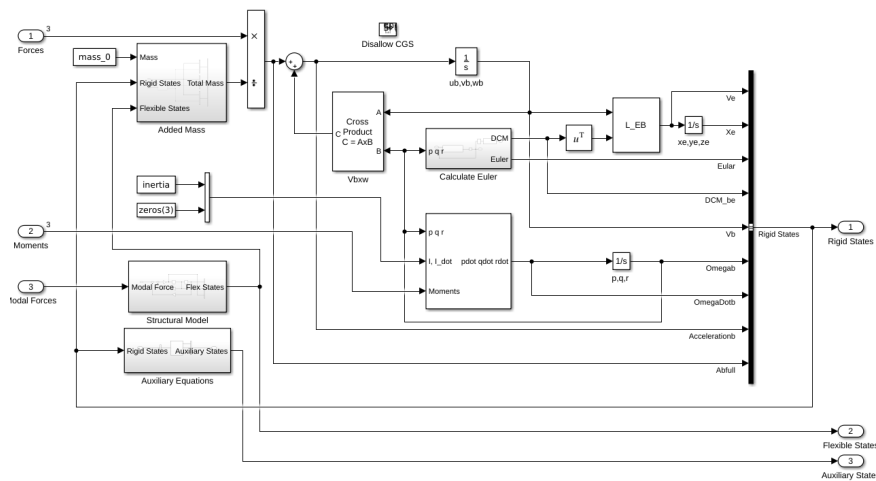
Figure 7.13: Equations of motion

Sensor outputs:

The equations for the accelerometer and IMU sensors have been described in Section 4.5. These equations are implemented as shown in Figure 7.14 and 7.15.
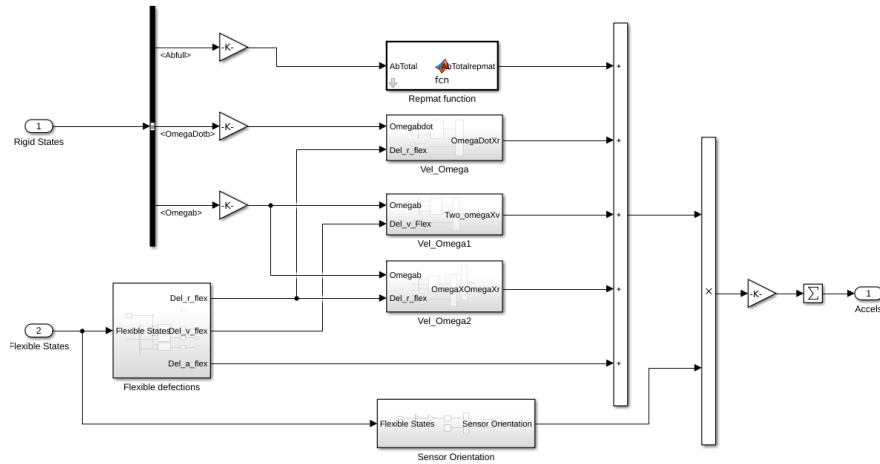
Figure 7.14: Accelerometer output
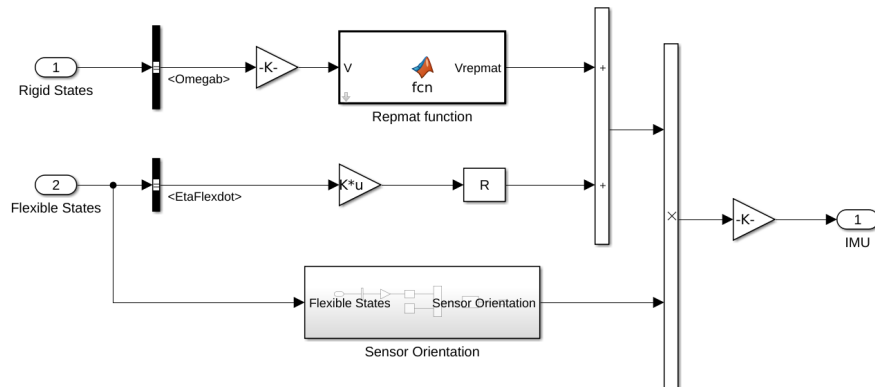
Figure 7.15: IMU output

7.2   Results from Flight Dynamics Model

The SIMULINK implementation described in the previous section results in a simulation model of the flexible aircraft Geri. The simulation model can also be thought of a the mathematical nonlinear flight dynamics model of the aircraft. The model can be used in an open loop configuration where the control inputs are

provided by the user. For example, for a manual flight where the inputs provided by the pilot are logged, the model can used to simulate the flight by giving the same inputs to the model. The model can also be used in the closed loop configuration by implementing the flight controller (including any flutter suppression controller) in the SIMULINK model itself.

The flight dynamics model is capable of modeling various flight conditions including steady and transient flights. Steady flight conditions include straight and level flight, steady turn at a constant bank angle, steady climb or descent, spiral climb and descent etc. The in-built trim functionality of SIMULINK can be used to trim the aircraft for these steady flight conditions. For example, the trim function is used to calculate the control surface deflections required for a 30 degree bank flight at 23 m/s. Transient flights can also be modeled by the flight dynamics model presented in this thesis. An example of transient flight is when the aircraft switches from one steady flight condition to another steady flight condition. For example, a straight and level flight to a banked turn.

The simulation model is extremely modular in the sense that various aerodynamic and structural phenomena can be switched on or off easily by the user. These phenomena include number of flexible modes, unsteady aerodynamics, geometrically nonlinear effects like change in direction of the local lift with flexible deflection of the aircraft, dependence of the AIC matrix on the flexibility etc. This capability can be used to study the properties of the aircraft in a deeper level and develop an understanding of underlying dynamics of the aircraft. The results of these simulations can be used for control system design or the next iterations of aircraft design.

7.2.1   Nonlinear Simulation

A simple test case is used to demonstrate the nonlinear flight dynamics model in the open loop configuration. Straight and level flight is considered at two different flight speeds of 23 m/s and 28 m/s. The trimming functionality is used to trim

the aircraft at an angle of attack of 1.87 and 1.15 degrees respectively for 23 m/s and 28 m/s case. Next, a doublet input is provided to the ailerons i.e L2, R2 control surfaces. The control surfaces are shown in Figure 2.5. The commanded input to ailerons are shown in Figure 7.16.
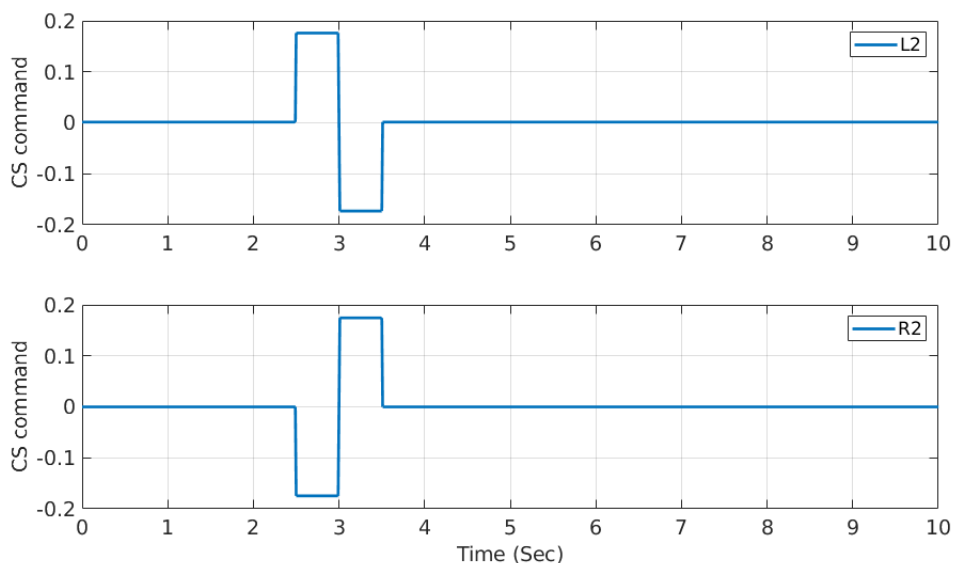
Figure 7.16: Command to 'L2' and 'R2' the control surfaces

The open loop response of the Euler angles to the doublet aileron input is shown in Figure 7.17. This example is specially useful to study the transient response of the model. Note that without a controller, the aircraft is mildly unstable and, therefore, the outputs drift over time.

The response of the modal deflections (η_1 and η_2) and velocities ($\frac{d\eta_1}{dt}$ and $\frac{d\eta_2}{dt}$) of the first two flexible modes are shown in Figure 7.18 and 7.19. It can be clearly observed that the flexible response is higher for the 28 m/s case even though same input is given to the aircraft. As expected, as the aircraft velocity increases and comes closer to the flutter speed, the margin of stability decreases. This leads to larger flexible deflections for a given input. If the aircraft velocity increases

and becomes equal to the flutter velocity, the flexible deflections increase without bounds and result in a catastrophic failure of the aircraft.
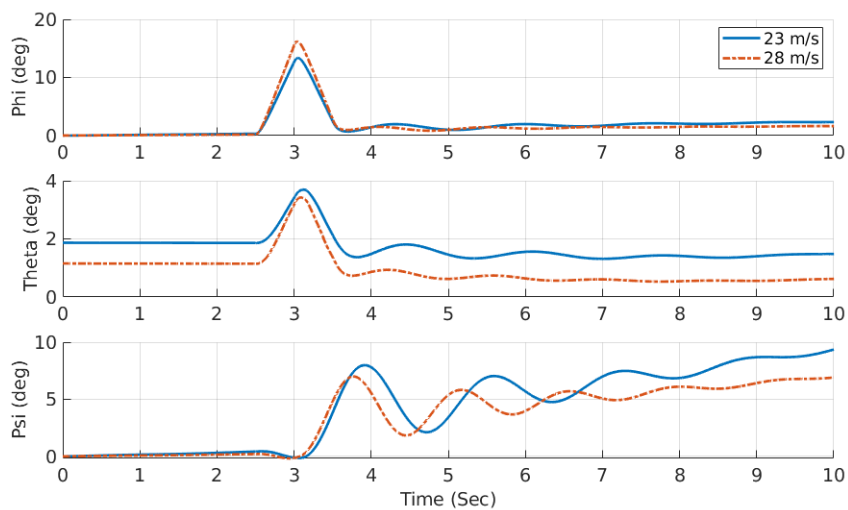
Figure 7.17: Response to doublet aileron input
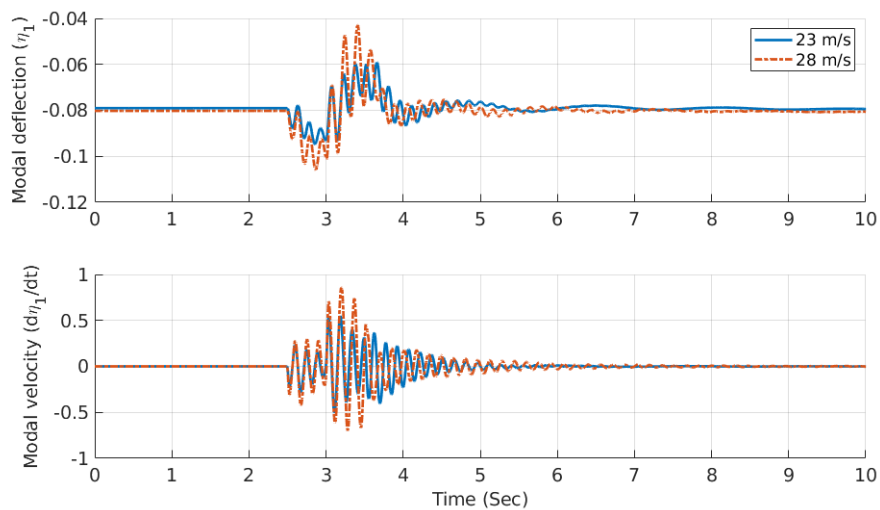
Figure 7.18: Response of first flexible mode to doublet aileron input
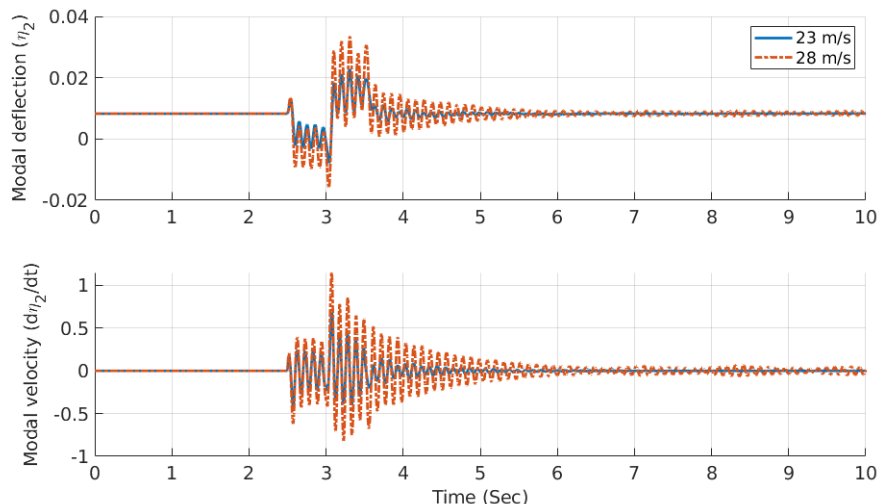
Figure 7.19: Response of second flexible mode to doublet aileron input

7.2.2 Trimming and Linearized Model

The nonlinear model can be linearized for any steady flight condition to obtain a low order, state space model of the aircraft for any trim condition. For example, the nonlinear model based on steady aerodynamic model with geometric nonlinearity is linearized for a 23 m/sec straight and level flight. This results in a 36 state linear model. The states of the models are the body frame velocity of the aircraft, Euler angles, angular velocities, modal deflections and velocities for the five included modes, control surface positions and velocities for eight control surfaces. Different models can be obtained for different flight conditions and for different aerodynamic models.

To demonstrate this, a linear model is obtained at 23 m/s straight and level flight. The frequency response from elevator i.e L3 and R3 control surfaces to the pitch rate of the mean axes is shown in Figure 7.20.
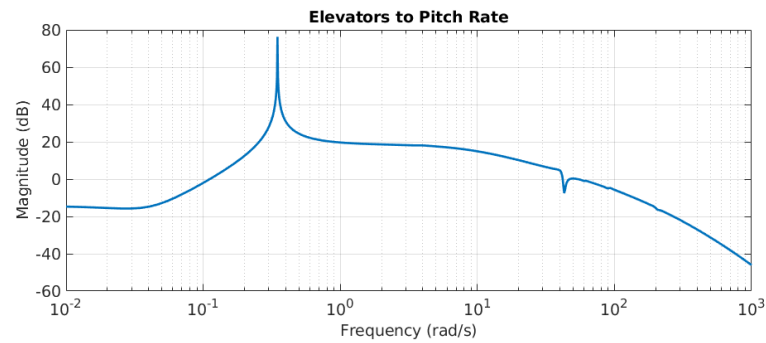
Figure 7.20: Frequency response from elevator to pitch rate

The response of elevator to the flexible deflections η_1 and η_2 are shown in Figure 7.21
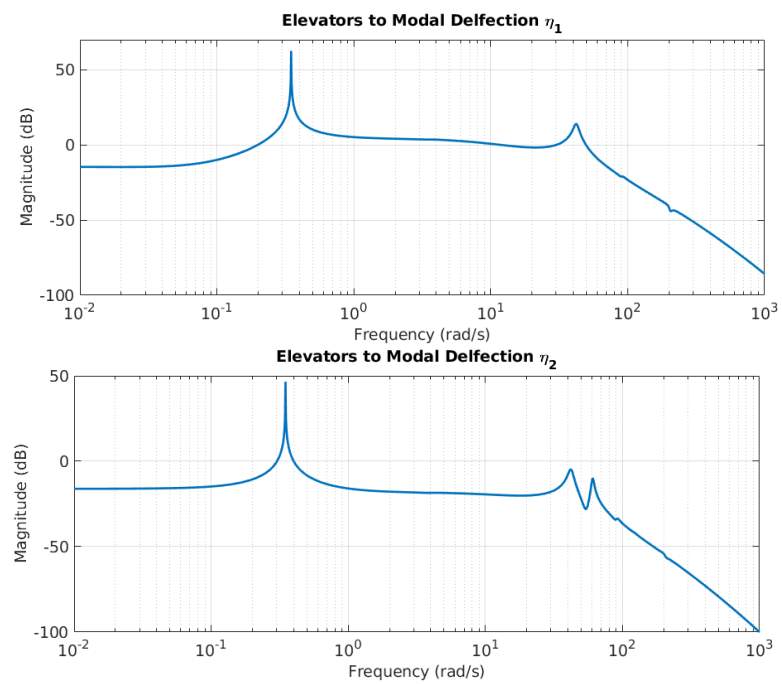
Figure 7.21: Frequency response from elevator to first flexible mode

7.2.3   Linear Flutter Analysis

The liner models can be used to obtain the flutter characteristics of the aircraft. The nonlinear model can be linearized for a range of flight velocities for straight and level flight. The poles of these linear models can be plotted in the S-plane. The flight velocities at which the poles cross from the left half plane to the right half plane, i.e cross the imaginary axis, are the flutter velocities of the aircraft. The aircraft becomes unstable if the flight velocity is higher than the minimum of these flutter velocities. The frequency of the poles at the imaginary axis corresponds to the flutter frequencies of the aircraft for the particular modes.

This analysis is conducted for a range of 20-40 m/sec straight and level flight. The results of the analysis is shown in Figure 7.22. It can be seen that the flutter velocity with a geometrically nonlinear, steady aerodynamic model is 30.5 m/sec. The flutter frequency is 6.05 Hz.
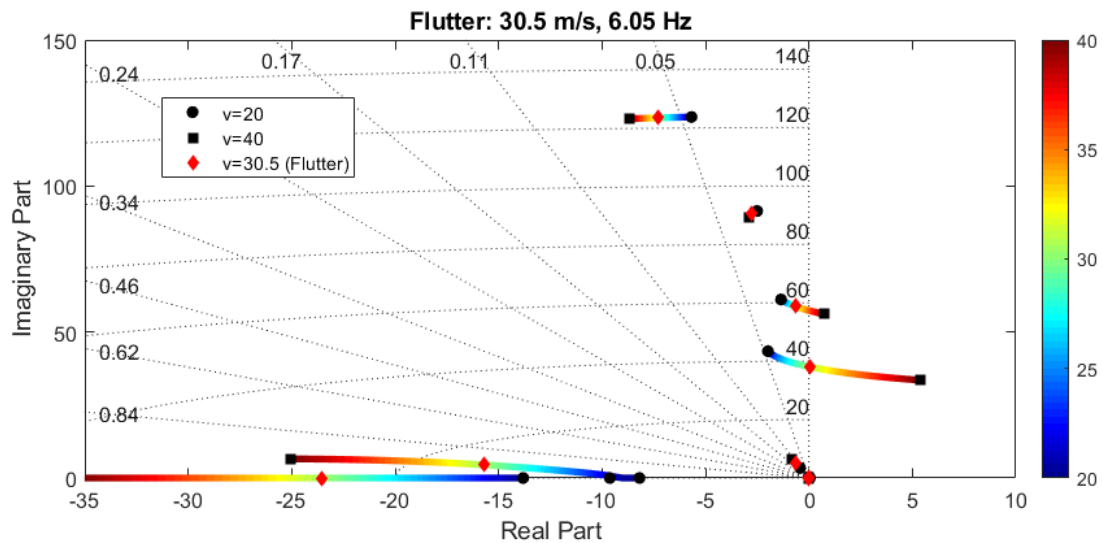
Figure 7.22: Flutter characteristics: Geometrically nonlinear model

7.3 Effect of Unsteady and Nonlinear Aerodynamics

In this section, the effect of various aerodynamic phenomena are studied. First the effect of geometrically nonlinear aerodynamics is studied by comparing it with models based on geometrically linear aerodynamics. The poles plot flight dynamics model with geometrically nonlinear, steady aerodynamics has been shown before in Figure 7.22. Similar plot is obtained for flight dynamics model with geometrically linear, steady aerodynamics. The flutter frequency for this type of model is 32.5 m/sec. This is 2 m/sec over the prediction from the model with geometrically nonlinear aerodynamic model. *Therefore, it can be concluded that the flight dynamics model without geometrically nonlinear aerodynamic model underpredicts the instability in the flight dynamics by a significant amount.* The flutter frequency is 6.06 Hz.
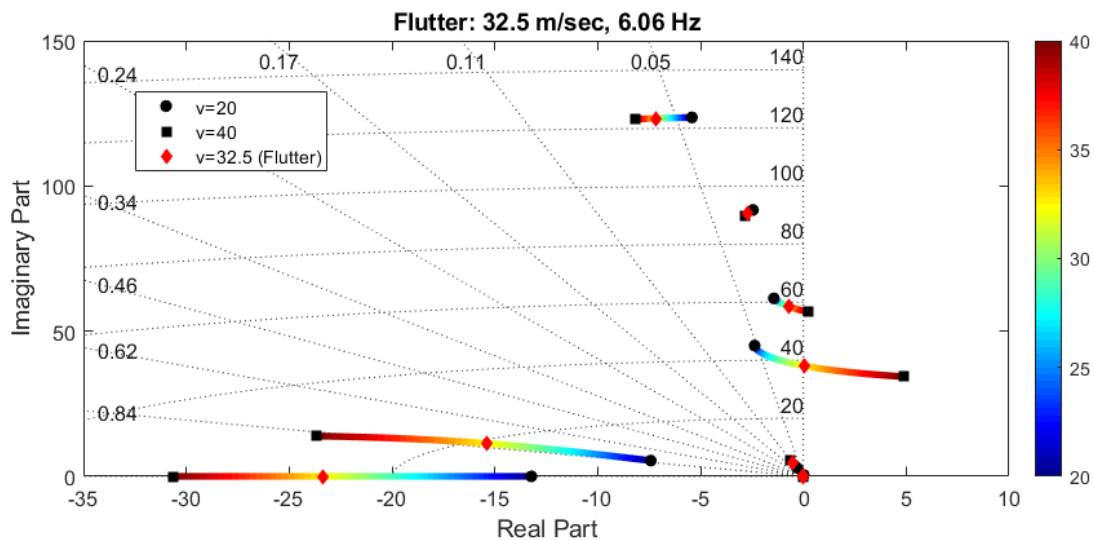
Figure 7.23: Flutter characteristics: Geometrically linear model

The effect of including the unsteady aerodynamics is also studied. The doublet

lattice method (DLM) used to model the unsteady aerodynamics has 2 lag poles for each panel. As Geri has $P = 888$ panels, the linear model obtained for this case has more than $2P = 1776$ poles. The poles plot for a velocity range of $20 - 40$ m/s is shown in Figure 7.24. It can be seen that the flight dynamics models with unsteady aerodynamics have very similar poles to that of the models with steady aerodynamics. The plot also show the lag poles on the real axis which were not present for the models with steady aerodynamics. Therefore, it is concluded that the unsteady aerodynamics is not important for obtaining the flutter characteristics of the aircraft Geri. Note that this analysis is specific to the aircraft Geri and can not be used to draw conclusions about the importance of unsteady aerodynamics for other aircraft.
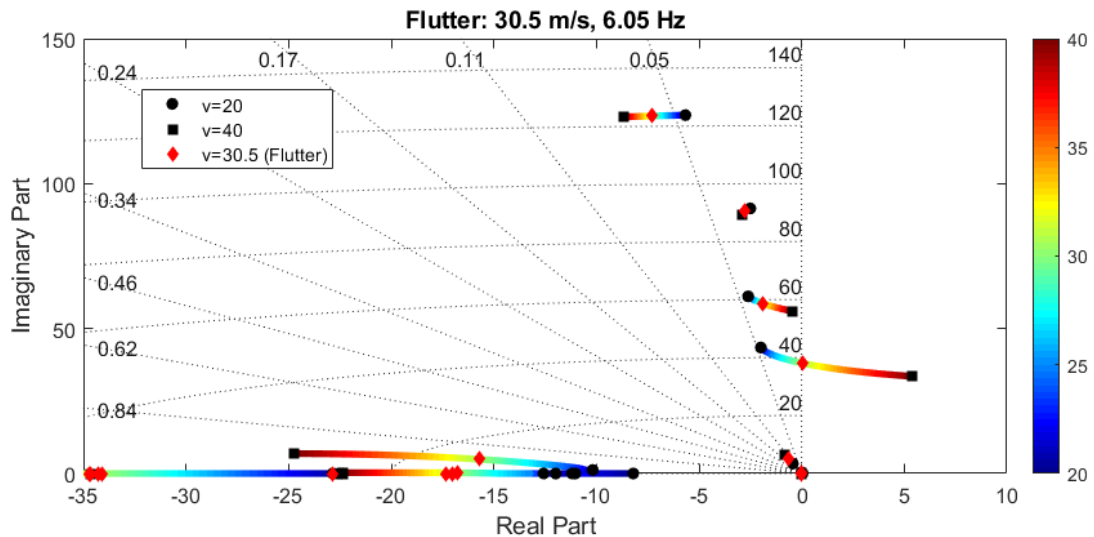
Figure 7.24: Flutter characteristics: Geometrically linear model with unsteady aerodynamics

7.4 Appendix

7.4.1 Approximation of AIC Matrix

This section derives the derivation of the relationship between the the AIC matrix and modal deflections as shown in Equation 7.2 using the assumption of small flexible deflection. Consider Equation 6.1 describing the relationship between the strength of all the horseshoe vortices and the total induced velocity at the mth panel. This equation can be stacked for all the panels and all three axes as follows:

$$
\begin{bmatrix}
V_{ind,x1} \\
V_{ind,y1} \\
V_{ind,z1} \\
V_{ind,x2} \\
V_{ind,y2} \\
\vdots \\
V_{ind,zP}
\end{bmatrix}
=
\begin{bmatrix}
Q_{x1,1} & Q_{x1,2} & \cdots & Q_{x1,P} \\
Q_{y1,1} & Q_{y1,2} & \cdots & Q_{y1,P} \\
Q_{z1,1} & Q_{z1,2} & \cdots & Q_{z1,P} \\
Q_{x2,1} & Q_{x2,2} & \cdots & Q_{x2,P} \\
Q_{y2,1} & Q_{y2,2} & \cdots & Q_{y2,P} \\
\vdots & \vdots & \ddots & \vdots \\
Q_{zP,1} & Q_{zP,2} & \cdots & Q_{zP,P}
\end{bmatrix}
\begin{bmatrix}
\mathcal{T}_1 \\
\mathcal{T}_1 \\
\vdots \\
\mathcal{T}_P
\end{bmatrix}
\tag{7.3}
$$

This can be equivalently written as:

$$
V_{ind} = Q\mathcal{T} \tag{7.4}
$$

where V_{ind} is a $3P$-by-1 vector, Q is a $3P$-by-P matrix and $\mathcal{T}$ is a P-by-1 vector.

Now consider the P-by-$3P$ block diagonal matrix N consisting of direction cosines of the normal vectors as

$$
N_v =
\begin{bmatrix}
n_{x1} & n_{y1} & n_{z1} & 0 & 0 & 0 & \cdots & 0 & 0 & 0 \\
0 & 0 & 0 & n_{x2} & n_{y2} & n_{z2} & \cdots & 0 & 0 & 0 \\
\vdots & \vdots & \vdots & \vdots & \vdots & \vdots & \ddots & \vdots & \vdots & \vdots \\
0 & 0 & 0 & 0 & 0 & 0 & \cdots & n_{xP} & n_{yP} & n_{zP}
\end{bmatrix}
\tag{7.5}
$$

Using Equation 6.3,7.4,7.5 and the fact that w_{ind} is the stacked version of

$w_{ind,m}$, the following equation is obtained:

$$
\begin{aligned}
w_{ind} &= N_v V_{ind} \\
&= N_v Q \mathcal{T}
\end{aligned}
\tag{7.6}
$$

Now, using Equation 6.8, 6.9 and 7.6, it can be concluded that

$$
[\text{AIC}(\eta)] = (-N_v Q)^{-1}
\tag{7.7}
$$

Note that the AIC matrix depends on the modal deflection η because normal vectors depend on η.

Now, we can expand the expression of the AIC matrix in Equation 7.7. First, using Equation 6.17,

$$
N_v = N_{v,0} + \sum_{k=1}^{n_{modes}} N_{v,k} \eta_k
\tag{7.8}
$$

where N_v, $N_{v,0}$ and $N_{v,k}$ are $3P$-by-P stacked block diagonal matrices corresponding to $\hat{n}_{m,flex}$, $\hat{n}_{m0}$ and $\vec{N}_{m,k}$ and have similar structure as shown for N_v in Equation 7.5. Combining Equations 7.7 and 7.8, we obtain the expression for AIC matrix as:

$$
\begin{aligned}
[\text{AIC}(\eta)] &= \left(- \left(N_{v,0} + \sum_{k=1}^{n_{modes}} N_{v,k} \eta_k \right) Q \right)^{-1} \\
&= \left(- N_{v,0} Q - \sum_{k=1}^{n_{modes}} N_{v,k} \eta_k Q \right)^{-1}
\end{aligned}
\tag{7.9}
$$

In order to simplify Equation 7.9, consider the following argument.

Let M be a given P-by-P matrix and η a scalar with $\eta * \rho(M) < 1$. Define the function

$$
f : \mathbb{R}^{P \times P} \to \mathbb{R}^{P \times P} : f(\eta) := (I + \eta M)^{-1} = I - \eta M + \eta^2 M^2 - \eta^3 M^3 + ...
$$

This can be shown by simply multiplying both sides by $(I+\eta M)$. The sum on the right converges based on the assumption $\eta * \rho(M) < 1$. Thus, the linear Taylor series expansion is:

$$(I - eta * M)^{-1} \approx I - \eta * M$$

Next consider the case where A and B be given P-by-P matrices and η a small scalar. Assume A to be non-singular. Define the function

$$f : \mathbb{R}^{P \times P} \to \mathbb{R}^{P \times P} : f(\eta) := (A + \eta B)^{-1}$$

Then the linear Taylor series expansion (using the fact above) is

$$
\begin{aligned}
(A + \eta B)^{-1} &= A^{-1} * (I + \eta B * A^{-1})^{-1} \\
&\approx A^{-1} * [I - \eta B * A^{-1}] \\
&= A^{-1} - \eta A^{-1} B A^{-1}
\end{aligned}
\tag{7.10}
$$

The approximation described by Equation 7.10 can be applied to Equation 7.9 to obtain the linear approximation the AIC matrix which depends upon the flexible deflections η_k as follows:

$$
\begin{aligned}
[\text{AIC}(\eta)] &= (-N_{v,0}Q)^{-1} - (-N_{v,0}Q)^{-1}\left(-\sum_{k=1}^{n_{modes}} N_{v,k} \right)(-N_{v,0}Q)^{-1}\eta_k \\
&= [\text{AIC}]_0 + \sum_{k=1}^{n_{modes}} [\text{A}_k]\eta_k
\end{aligned}
\tag{7.11}
$$

Chapter 8

Flight Test Update

The flight dynamics model described in this thesis combines various subcomponents including structural dynamics, aerodynamics and the mean-axis based flight dynamics. This mathematical model is compared and validated against actual flight data. The model is also updated to reduce any mismatch with the flight data. This chapter describes the process of comparison, validation and update of the flight dynamics model based on flight test data of the aircraft Geri.

8.1 Introduction

The mathematical model of the flight dynamics of the aircraft Geri is described in Chapter 7. The model combines various submodules like structural dynamics, aerodynamics and mean axes based flight dynamics. Various approximations have been made while developing the flight dynamics model. For example, the steady and unsteady aerodynamic models are developed using panel methods. These methods assume that the lifting surfaces are flat and they ignore any aerodynamic nonlinearities. Therefore, such a mathematical model which is derived by employing various approximations should be validated against data obtained from the real system. Moreover, the model must be updated if significant differences are observed in comparison to data collected from the actual system. Several

methods are available to update a flight dynamics model.

The submodules used to obtain the flight dynamics model were derived based on different approximations. For example, the flight dynamics equations based on the mean axes approach are derived from theory while making reasonable assumptions of small flexible deflections of the aircraft. This makes the mean axes based equations accurate. Therefore, a high level of confidence can be assigned to the equations. The structural model is based on the finite element method which is a linear model. This structural model has been separately updated using experimental data obtained from ground vibration tests. Therefore, a higher level of confidence can be assigned to the updated structural model as well. On the other hand, the panel method based aerodynamics model assumes the lifting surfaces to be flat. It also ignores the aerodynamic nonlinearities. Therefore, the aerodynamic model has the least amount of confidence. Updating the aerodynamics model would be a reasonable approach to update the final flight dynamics model.

There are several approaches available to update aerodynamic models. One such approach based on correction matrices was proposed by Rodden in [37]. This approach is specially suitable for updating a panel method based aerodynamic model. This is because the panel methods output an AIC matrix that can be corrected based on pre-multiplicative and post-multiplicative matrices [1]. As the AIC matrix is independent of the flight conditions like aircraft velocity, the same corrective matrices can be utilized to update the model for different operating conditions.

Section 8.2 describes the various flight tests conducted on the aircraft for the purpose of flight dynamics identification. The details of the methodology implemented to update the flight dynamics model is described in Section 8.3. The updated model is analyzed and compared with the initial model in Section 8.4. The section also contains flutter predictions from the updated model.

---

[1] Note that post-multiplicative matrix multiplies on the input of the AIC matrix and pre-multiplicative matrix multiples on the output of the AIC matrix

8.2   Summary of Flight Tests

Several flights were conducted on the aircraft Geri for various purposes [13, 70]. Each flight consisted of several smaller flight tests, carried out for a brief period of time during the flight. Five of these flight tests focused on system identification. Orthogonal multi-sine and chirp inputs were provided to the control surface inputs for the system identification flight tests. The details of these five flight tests are given in Table 8.1.

Various input and output signals were logged during these flight tests. The input signals consist of various symmetric and asymmetric signals to the control surfaces. For example, the same orthogonal multi-sine signal was injected at L4 and R4 control surfaces during flight test-1. This input is labeled as Sym-4 in Table 8.1. The measurements made by various sensors on the aircraft were logged as outputs. These sensors include six accelerometers placed close to the leading edge and trailing edge in the two wings and the centerbody of the aircraft. The orientation measurements made by the inertial measurement unit (IMU) located in the centerbody of the aircraft are also logged as outputs. Both input and output signals were recorded with a sample rate of 151 Hz.

Flight Test	Airspeed (m/s)	Test time (s)	Input details
1	23	[635, 647]	OMS to Sym-4 input
2	23	[692.5, 704.9]	OMS to Sym-3 and Sym-4 inputs
3	23	[633.1, 645.2]	OMS to Sym-1 and Sym-4 inputs
4	20	[928.5, 940.6]	OMS to Sym-3 and Sym-4 inputs
5	23	[304.8, 323.5]	Chirp to Asym-4 input

Table 8.1: Flight tests used for model update and validation

The time domain signal of the Sym-4 input for flight test-1 is shown for a duration of 2 seconds in Figure 8.1. The frequency content of this input signal is shown in Figure 8.2. It can be seen that the signal excites frequencies of up to around 120 rad/sec. The time domain signal of the acceleration measurement by the accelerometer located at the left wing close to the leading edge is shown in

Figure 8.3.

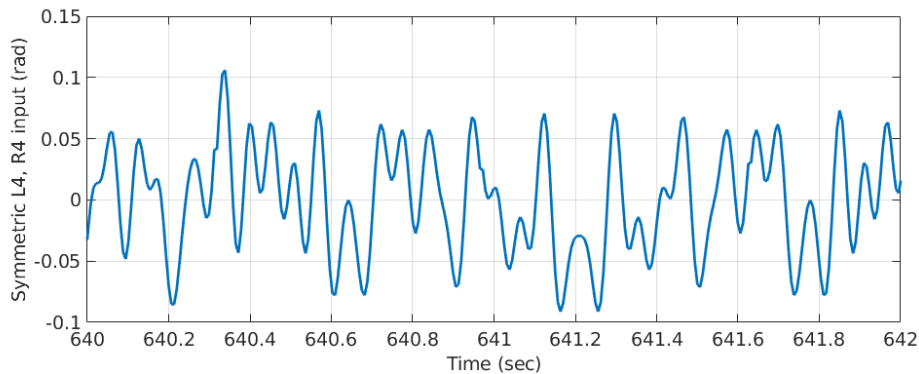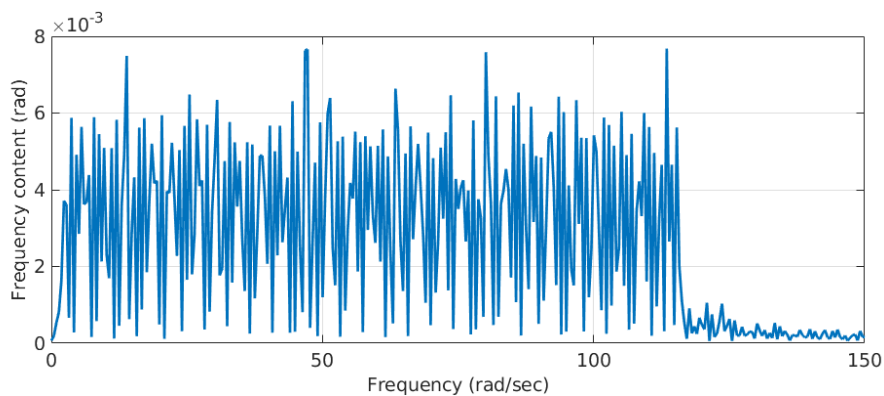Figure 8.1: Signal to symmetric L4, R4 input

Figure 8.2: Frequency content of input signal for flight test-1

8.3   Model Update Procedure

8.3.1   Flight Test Data Analysis

The data obtained from the flight tests is in time domain. Frequency response functions are approximated from the time domain data. Numerical computing software MATLAB is utilized for this analysis. The function *etfe* provided by
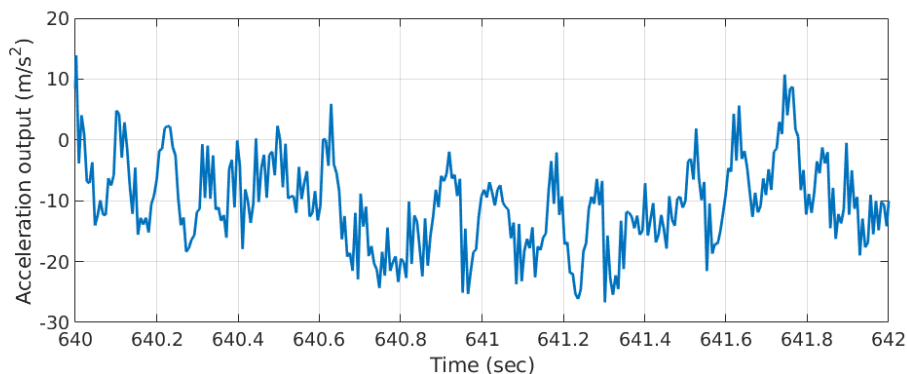
Figure 8.3: Acceleration output at left wing

the system identification toolbox of MATLAB is used for this purpose. Using this function, frequency response functions are obtained from the relevant inputs to all the available outputs at 512 points in the frequency range of 0 to 100 rad/sec. A *hamming* window with a frequency resolution of $\pi/80$ is utilized to smoothen the spectral estimates. Figure 8.4 shows the estimated frequency response function from the Sym-4 input to the left wing forward accelerometer output for flight test-1. Note that the frequency response function is a complex valued function and has both magnitude and phase. Similar responses are obtained from the other flight tests as well.

8.3.2 Correction Matrices

The method of using correction matrices for updating the aerodynamic model suggested by [37] is utilized to obtain the updated flight dynamics model. The aerodynamic model is corrected by modifying the AIC matrix calculated by the aerodynamic model. The AIC matrix is modified by pre and post-multiplying by correction matrices. This yields the following modified form for Equation 7.2:

$$[\text{AIC}(\eta)] = [C_{pre}][\text{AIC}]_0[C_{post}] + \sum_{k=1}^{n_{modes}} [C_{pre}][\text{A}_k][C_{post}]\eta_k \qquad (8.1)$$
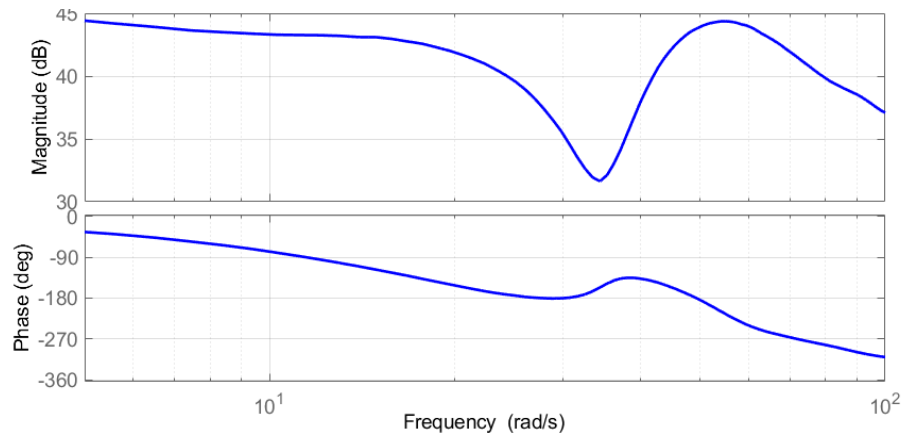
Figure 8.4: Estimated frequency response from Sym-4 input to left wing forward accelerometer output for using flight test-1 data

where [AIC] is a P-by-P matrix calculated by the aerodynamic model, $[C_{pre}]$ and $[C_{post}]$ are P-by-P correction matrices.

The pre-multiplicative correction matrix is equivalent to correcting the vortex strength on the aerodynamic panels as calculated by the panel methods. This directly corrects the aerodynamic forces acting on the panels. A post-multiplicative correction matrix corrects the normalwash as seen by the panels. This normalwash is utilized by the aerodynamic model to calculate the aerodynamic forces. In other words, a pre-multiplicative matrix corrects the output of the aerodynamic model while a post-multiplication corrects the input to the aerodynamic model.

The aerodynamic grid for the aircraft Geri has $P = 888$ panels. This makes the total number of free parameters of the two correction matrices to be $2P^2 = 1577088$. Identifying such a large number of parameters from the flight test data is virtually impossible. Fortunately, the number of parameters can be drastically reduced by using a few simple approximations. First, it is assumed that both the correction matrices are diagonal. A diagonal post-multiplicative correction matrix implies that same correction is applied to the relationship from the downwash of a particular panel to the vortex strength of all the other panels. Similarly, a diagonal pre-multiplicative correction matrix implies that same correction is applied to the

relationship from the downwash of all the panels to the vortex strength of a particular panel. This approximation reduces the number of free parameters from $2P^2 = 1577088$ to $2P = 1776$.

The number of free parameters in the correction matrices formulation is further reduced using basis functions for correction matrices. For example, the ith diagonal element of the pre-multiplicative correction matrix is written as a sum of polynomial basis functions as:

$$[C_{pre}]_{\{i,i\}} = 1 + a_1 + a_2 x + a_3 x^2 + a_4 y^2 + a_5 x^3 + \\ a_6 xy^2 + a_7 x^4 + a_8 x^2 y^2 + a_9 y^4 \tag{8.2}$$

where a_j is the coefficient of the jth basis function, x and y are the x and y coordinates of the centroid of the ith panel in the coordinate system located at the center of gravity of the undeformed aircraft. The x-axis points towards the tail of the aircraft and y-axis towards the right wing. Note that when these coefficients are zero i.e $a_i = 0$ for $i \in \{1 : 9\}$, the correction matrix $[C_{pre}]$ becomes identity matrix. This means that no correction is made. Similarly, the post-multiplicative correction matrix can be written in terms of the basis functions as:

$$[C_{post}]_{\{i,i\}} = 1 + b_1 + b_2 x + b_3 x^2 + b_4 y^2 + b_5 x^3 + \\ b_6 xy^2 + b_7 x^4 + b_8 x^2 y^2 + b_9 y^4 \tag{8.3}$$

The use of these basis functions reduce the number of unknown parameters to 18.

8.3.3   Parameter Identification

To update the flight dynamics model, a gray box approach is utilized. The flight dynamics model is parameterized. The parameters are then identified by minimizing the difference between the frequency responses identified from the flight test data and the model.

The correction matrices have been parameterized with eighteen parameters as described in the previous section. Apart from these eighteen parameters, two

more parameters are included in the flight dynamics update procedure. The first parameter relates to the time delay added to the flight dynamics model. The expression for this time delay is

$$T_d(s) = e^{-\frac{(1+\tau_d)s}{f_s}} \tag{8.4}$$

where f_s is the sampling frequency of the flight test data. Note that if the value of the parameter τ_d is zero, a nominal time delay of 1 sample time is employed. This time delay captures any transmission delays present in the onboard computer, sensor modules and data acquisition system.

The second parameter is the damping of the first flexible mode. The damping of the flexible modes were not identified using the GVT data and the first modal damping was assumed to be 0.02. The new damping for the first flexible mode can be written as

$$\zeta_1 = 0.02 \times (1 + \zeta_u) \tag{8.5}$$

Note that if the value of the parameter ζ_u is zero, the damping of the first flexible mode is at the nominal value of 0.02. Thus, the flight dynamics model is parameterized by a total of twenty unknown parameters.

An optimization routine based on *trust region* algorithm [71] is implemented using the MATLAB function *fmincon*. The cost function is based on the square of the difference in magnitude in the frequency responses identified from the flight test data and the flight dynamics model. This difference is summed up for a set of frequencies (F) for all considered input-output pairs (IO) and for all relevant flight tests (FT) to obtain the cost function. The optimization problem can be written as follows:

$$P_u^* = \arg\min_{P_u \in S} \sum_{FT} \sum_{IO} \sum_{\omega \in F} \left(|H_f(\omega) - H_m(\omega, P_u)|^2 \right) \tag{8.6}$$

where P_u is the 20-by-1 vector containing the update parameters, S is set of allowable values for the parameters, F is the set of frequencies at which the frequency

responses are evaluated, $H_f(\omega)$ is the complex frequency response identified from the flight test data and $H_m(\omega, P_u)$ is the complex frequency response obtained from the flight dynamics model for the given parameter vector P_u. Note that the flight dynamics model depends on the selected parameter vector P_u and this has been explicitly denoted in the frequency response by $H_m(\omega, P_u)$. Also note that this optimization is non-convex and `fmincon` is not guaranteed to find a global optimum. Hence, we will only seek a local optimum which improves on the baseline (nominal) parameter values.

Parameter	Constraint	Initial Value	Optimized Value
a_1	$-10 \le a_1 \le 10$	0	0.133
a_2	$-10 \le a_2 \le 10$	0	-0.486
a_3	$-10 \le a_3 \le 10$	0	0.661
a_4	$-10 \le a_4 \le 10$	0	-0.040
a_5	$-10 \le a_5 \le 10$	0	2.702
a_6	$-10 \le a_6 \le 10$	0	-0.368
a_7	$-10 \le a_7 \le 10$	0	0.946
a_8	$-10 \le a_8 \le 10$	0	0.071
a_9	$-10 \le a_9 \le 10$	0	-0.109
b_1	$-10 \le b_1 \le 10$	0	-0.654
b_2	$-10 \le b_2 \le 10$	0	0.566
b_3	$-10 \le b_3 \le 10$	0	-1.309
b_4	$-10 \le b_4 \le 10$	0	0.173
b_5	$-10 \le b_5 \le 10$	0	-0.705
b_6	$-10 \le b_6 \le 10$	0	0.726
b_7	$-10 \le b_7 \le 10$	0	0.256
b_8	$-10 \le b_8 \le 10$	0	0.113
b_9	$-10 \le b_9 \le 10$	0	0.461
τ_d	$0 \le \tau_d \le 5$	0	0.847
ζ_u	$-1 \le \zeta_u \le 2$	0	0.622

Table 8.2: Parameters for model udpated

For the optimization, the objective is evaluated on a set F of 1000 logarithmically spaced points in the range of 5 rad/sec to 100 rad/sec. The flight tests

utilized for the model update are given in Table 8.1. The inputs are listed in the the table as well. For symmetric inputs, all 6 accelerometers measurements and the pitch rate measurement from the IMU located in the centerbody are included. For asymmetric inputs, measurements from the four accelerometers located on the wings and the roll rate measurement from the IMU are included. The details of the parameters and the constraints are given in Table 8.2.

8.4　Updated Flight Dynamics Model

The correction parameters obtained from the flight dynamics model are independent of the flight conditions. Thus, updated flight dynamics model for any flight condition can be derived easily using the same parameters. Figure 8.5 shows the comparison between the frequency response of the updated flight dynamics model with the nominal (before update) and identified frequency response from the flight tests.
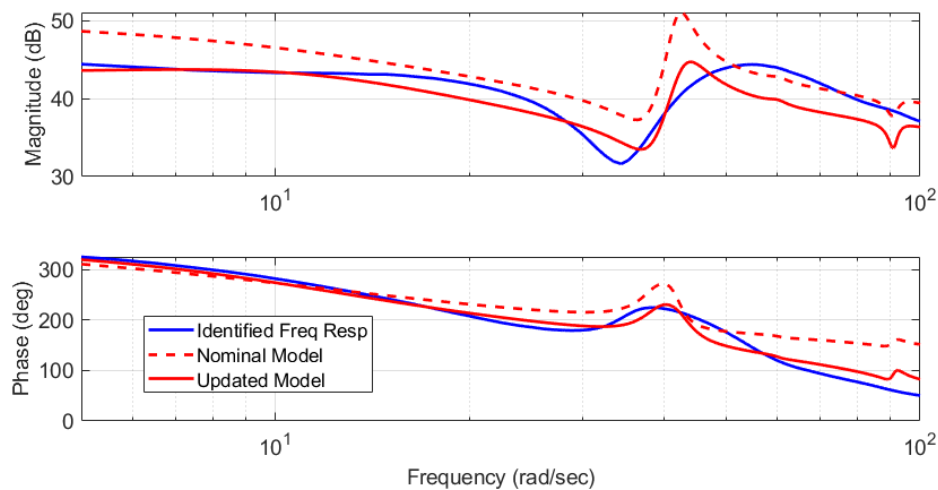

Figure 8.5: Frequency response comparison of updated model, nominal model and flight test

It can be seen that the frequency response of the updated model has a better

match with the frequency response from the flight dynamics model as compared to the nominal model. The cost function reduced by 45% as a result of the optimization. The frequency response and the flutter prediction from the updated model are analyzed in the next section. The updated models can be linearized to obtain state space models at increasing flight speeds. Flutter characteristics can be identified from the poles of the state space models.
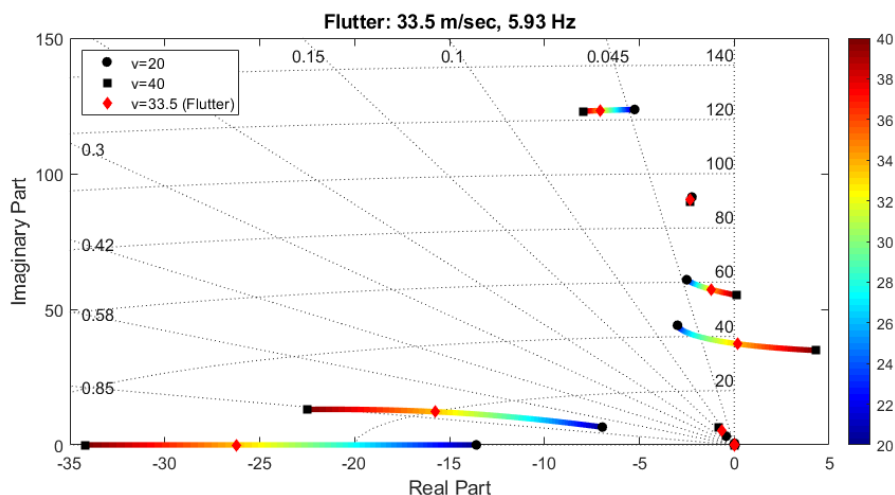
Figure 8.6: Flutter analysis from updated model

Figure 8.6 shows the plot for various flight speeds. The flutter speed is identified as 33.5 m/s from the updated flight dynamics model compared 30.5 m/s for the nominal model (before update). It should be noted that the identified flutter speed of 33.5 m/s is quite close to the prediction from another flight dynamics model of the aircraft based on aerodynamic coefficients which is updated with flight test data as well [63].

8.5 Validation

The updated flight dynamic model described in the previous section needs to be validated to ensure that the model update procedure did not suffer from overfitting. In order to conduct the validation, a flight test data which has not been used for model updated is utilized. A flight test data from a flight at 20 m/s is used. Note that the model update was conducted using flight tests at 23 m/s. Using a different flight speed for validation also ensures that the extrapolation of the model update procedure to different flight speeds is also validated.

The same cost function as Equation 8.6 is utilized for validation. The frequency responses for the flight at 20 m/s is shown below in Figure 8.7. It can be seen that the frequency response from the updated flight dynamics model is closer to the identified frequency response from the flight test data. A 20 % reduction is observed in the cost function for this case as well.
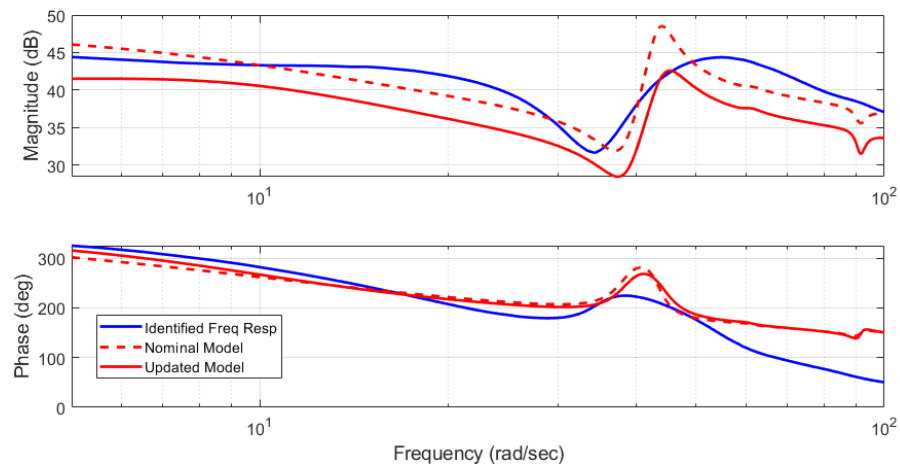

Figure 8.7: Model update validation using flight at 20 m/s

Thus, it can be concluded that the model has been successfully updated and validated using various flight test data.

Chapter 9

Concluding Remarks

This chapter contains the closing remarks on the overall research and the results of the research in this thesis. The work presented here opens up several avenues for future research. Some possible future research based on this thesis are discussed in this chapter.

9.1 Conclusions

A medium fidelity flight dynamics model of the flexible aircraft Geri is developed. Geri is one of the mAEWing1 series of aircraft developed under the Performance Adaptive Aeroelastic Wing (PAAW) project. The mean axes approach is utilized for the development of the flight dynamics model as it decouples the flexible structural modes from the rigid body modes. Various submodules of the flight dynamics model are developed separately and combined in the simulation software SIMULINK to obtain the flight dynamics model. The steps to develop these submodules and the lesson learned are discussed in details in this thesis.

The submodule of structural dynamics model of the aircraft is developed based on Finite Element Method approach. Ground vibration tests are conducted to obtain data to update the structural model. Similarly, the aerodynamic model is developed by modifying and implementing a panel-based model. The vortex

lattice method is used to model the steady aerodynamics while the doublet lattice method is used for unsteady aerodynamics. Modifications are made to the VLM method to capture the geometrically nonlinear aerodynamics effects on the flight dynamics model. These effects are evaluated and it is concluded that modeling the geometric nonlinearity is essential to capture the accurate flutter characteristics. For Geri, including geometric nonlinearity in aerodynamics results in a 2 m/sec decrease in the flutter velocity estimation. The presence of unsteady aerodynamics has minimal effect on the flutter characteristic.

Flight test data is used to identify the frequency response from various control surface inputs to sensors outputs. The frequency responses from the flight dynamics model are compared with the responses identified from flight data. The flight dynamics model is parameterized using the correction matrices approach to update the aerodynamics model. Basis functions are used to reduce the number of free parameters to 20. An optimization is posed and solved for (locally) optimal values of the parameters which reduces the difference between the two frequency responses. Thus, an updated flight dynamics model is obtained and analyzed. The flutter velocity of the updated model is found to be 33.5 m/s which matches with the prediction from other higher fidelity methods. The updated model is validated using a separate flight test data at a different speed. The flight dynamics model of Geri is available at [14] and [15] for free.

9.2   Future Work

The low cost and modularity of the model makes it suitable for analysis of the effects of various kinds of phenomena. Individual subcomponent of the flight dynamics model can be easily changed to conduct *one parameter at a time* analysis to quantify the effects of a particular aerodynamic or structural phenomena. The effect of geometric nonlinearity and unsteady aerodynamics has been already discussed in this thesis. Similar analysis can be done to quantify the effect of other phenomena like structural nonlinearity, more accurate plate based FEM

model, more advanced unsteady aerodynamics model like 'Unsteady Vortex Lattice Method' (UVLM) etc.

The low computational cost of the model also makes it amenable towards Monte-Carlo analysis to quantify the uncertainty of open loop model. For example, Monte-Carlo simulations can be used to obtain a set of linear models based on the uncertainty in the first symmetric bending mode shape. This set of models can be used can be used to design robust flutter control systems for the identified unstructured uncertainty. Similar approach can be used to analyze the uncertainty in various parameters like mode shapes, modal frequencies and aerodynamic properties. Monte-Carlo analysis can be used to demonstrate the robustness of close loop models with respect to these kinds of uncertainties as well.

References

[1] P. P. Friedmann. Renaissance of aeroelasticity and its future. *Journal of Aircraft*, 36(1):105–121, 1999.

[2] J. J. Ryan and J. T. Bosworth. Current and future research in active control of lightweight, flexible structures using the X-56 aircraft. In *52nd Aerospace Sciences Meeting*, page 0597, 2014.

[3] R. L. Bisplinghoff, H. Ashley, and R. L. Halfman. *Aeroelasticity*. Courier Corporation, 2013.

[4] D. H. Hodges and G. A. Pierce. *Introduction to structural dynamics and aeroelasticity*, volume 15. cambridge university press, 2011.

[5] D. K. Schmidt. *Modern flight dynamics*. McGraw-Hill New York, 2012.

[6] Y. C. Fung. *An introduction to the theory of aeroelasticity*. Courier Dover Publications, 2008.

[7] M. R. Waszak and S. Srinathkumar. Flutter suppression for the active flexible wing-a classical design. *Journal of Aircraft*, 32(1):61–67, 1995.

[8] A. Kotikalpudi, B. P. Danowsky, D. K. Schmidt, J. Theis, and P. Seiler. Flutter suppression control design for a small, flexible flying-wing aircraft. In *2018 Multidisciplinary Analysis and Optimization Conference*, page 3426, 2018.

[9] J. Theis, H. Pfifer, and P. Seiler. Robust control design for active flutter suppression. In *AIAA Atmospheric Flight Mechanics Conference*, page 1751, 2016.

[10] D. K. Schmidt. Stability augmentation and active flutter suppression of a flexible flying-wing drone. *Journal of Guidance, Control, and Dynamics*, 38(11):409–422, 2015.

[11] C. P. Moreno. Linear, parameter-varying control of aeroservoelastic systems. 2015.

[12] B. P. Danowsky. Flutter suppression of a small flexible aircraft using midaas. In *AIAA Atmospheric Flight Mechanics Conference*, page 4353, 2017.

[13] B. P. Danowsky, A. Kotikalpudi, D. K. Schmidt, C. Regan, and P. Seiler. Flight testing flutter suppression on a small flexible flying-wing aircraft. In *2018 Multidisciplinary Analysis and Optimization Conference*, page 3427, 2018.

[14] Performance Adaptive Aeroeleastic Wing (PAAW) Program at University of Minnesota digital conservancy. `https://conservancy.umn.edu/handle/11299/167170`.

[15] Flight dynamics model of the aircraft geri. `https://github.com/gupta165/FlightDynamicsModel_Geri`.

[16] Performance Adaptive Aeroelastic Project. `http://paaw.net`.

[17] C. D. Regan and C. V. Jutte. Survey of applications of active control technology for gust alleviation and new challenges for lighter-weight aircraft. 2012.

[18] C. D. Regan and B. R. Taylor. maewing1: Design, build, test-invited. In *AIAA Atmospheric Flight Mechanics Conference*, page 1747, 2016.

[19] E. Burnett, C. Atkinson, J. Beranek, B. Sibbitt, B. Holm-Hansen, and L. Nicolai. Ndof simulation model for flight control development with flight test correlation. In *AIAA Modeling and Simulation Technologies Conference*, page 7780, 2010.

[20] J. Beranek, L. Nicolai, M. Buonanno, E. Burnett, C. Atkinson, B. Holm-Hansen, and P. Flick. Conceptual design of a multi-utility aeroelastic demonstrator. In *13th AIAA/ISSMO Multidisciplinary Analysis Optimization Conference*, page 9350, 2010.

[21] E. Burnett, J. Beranek, B. Holm-Hansen, C. Atkinson, and P. Flick. Design and flight test of active flutter suppression on the X-56a multi-utility technology test-bed aircraft. *The Aeronautical Journal*, 120(1228):893–909, 2016.

[22] E. Livne. Aircraft active flutter suppression: State of the art and technology maturation needs. *Journal of Aircraft*, 55(1):410–452, 2017.

[23] D. K. Schmidt, W. Zhao, and R. K. Kapania. Flight-dynamics and flutter modeling and analyses of a flexible flying-wing drone-invited. In *AIAA Atmospheric Flight Mechanics Conference*, page 1748, 2016.

[24] D. K. Schmidt, B. P. Danowsky, P. Seiler, and R. K. Kapania. Flight-dynamics and flutter analysis and control of an mdao-designed flying-wing research drone. In *AIAA Scitech 2019 Forum*, page 1816, 2019.

[25] W. Zhao, M. Jrad, R. Gupta, and R. K. Kapania. Multidisciplinary design analysis and optimization of performance adaptive aeroelastic wings. In *AIAA Atmospheric Flight Mechanics Conference*, page 1392, 2017.

[26] A. Dorobantu, W. Johnson, A. F. Lie, B. Taylor, A. Murch, Y. C. Paw, D. Gebre-Egziabher, and G. Balas. An airborne experimental test platform: From theory to flight. In *2013 American Control Conference*, pages 659–673. IEEE, 2013.

[27] A. Gupta, W. Zhao, C. Regan, P. Seiler, and R. K. Kapania. Identification of symmetrical structures with fabrication and damage induced asymmetry. In *International Conference on Experimental Vibration Analysis for Civil Engineering Structures*, pages 683–693. Springer, 2017.

[28] M. R. Waszak and D. K. Schmidt. Flight dynamics of aeroelastic vehicles. *Journal of Aircraft*, 25(6):563–571, 1988.

[29] D. L. Logan. *A first course in the finite element method*. Cengage Learning, 2011.

[30] J. Ketz and A. Plotkin. *Low-speed aerodynamics: from wing theory to panel methods*. McGraw-Hill, Incorporated, 1991.

[31] E. Albano and W. P. Rodden. A doublet-lattice method for calculating lift distributions on oscillating surfaces in subsonic flows. *AIAA journal*, 7(2):279–285, 1969.

[32] M. Blair. A compilation of the mathematics leading to the doublet lattice method. Technical report, WRIGHT LAB WRIGHT-PATTERSON AFB OH, 1992.

[33] W. P. Rodden, P. F. Taylor, and S. C. McIntosh. Further refinement of the subsonic doublet-lattice method. *Journal of Aircraft*, 35(5):720–727, 1998.

[34] A. Kotikalpudi, H. Pfifer, and G. J. Balas. Unsteady aerodynamics modeling for a flexible unmanned air vehicle. In *AIAA Atmospheric Flight Mechanics Conference*, page 2854, 2015.

[35] R. D. Milne. *Dynamics of the deformable aeroplane*. PhD thesis, University of London (Queen Mary College), 1962.

[36] S. A. Keyes, P. Seiler, and D. K. Schmidt. A newtonian development of the mean-axis equations of motion for flexible aircraft. In *AIAA Atmospheric Flight Mechanics Conference*, page 1395, 2017.

[37] J. P. Giesing, T. P. Kalman, and W. P. Rodden. Correction factory techniques for improving aerodynamic prediction methods. 1976.

[38] M. V. Cook. *Flight dynamics principles: a linear systems approach to aircraft stability and control.* Butterworth-Heinemann, 2012.

[39] D. T. McRuer, D. Graham, and I. Ashkenas. *Aircraft dynamics and automatic control*, volume 740. Princeton University Press, 2014.

[40] L. Meirovitch and I. Tuzcu. The lure of the mean axes. *Journal of Applied Mechanics*, 74(3):497–504, 2007.

[41] D. K. Schmidt. Discussion:the lure of the mean axes(meirovitch, l., and tuzcu, i., asme j. appl. mech., 74 (3), pp. 497–504). *Journal of Applied Mechanics*, 82(12):125501, 2015.

[42] S. A. Keyes, P. Seiler, and D. K. Schmidt. Newtonian development of the mean-axis reference frame for flexible aircraft. *Journal of Aircraft*, 56(1):392–397, 2018.

[43] M. J. Patil, D. H. Hodges, and C. E. S. Cesnik. Nonlinear aeroelasticity and flight dynamics of high-altitude long-endurance aircraft. *Journal of Aircraft*, 38(1):88–94, 2001.

[44] C. Park, C. Y. Joh, and Y. S. Kim. Multidisciplinary design optimization of a structurally nonlinear aircraft wing via parametric modeling. *International Journal of Precision Engineering and Manufacturing*, 10(2):87–96, 2009.

[45] I. Lee and S. H. Kim. Aeroelastic analysis of a flexible control surface with structural nonlinearity. *Journal of Aircraft*, 32(4):868–874, 1995.

[46] B. Lee and A. Tron. Effects of structural nonlinearities on flutter characteristics of the cf-18 aircraft. *Journal of Aircraft*, 26(8):781–786, 1989.

[47] A. Gupta, C. P. Moreno, H. Pfifer, B. Taylor, and G. J. Balas. Updating a finite element based structural model of a small flexible aircraft. In *AIAA Modeling and Simulation Technologies Conference*, page 0903, 2015.

[48] M. Drela. Integrated simulation model for preliminary aerodynamic, structural, and control-law design of aircraft. In *40th Structures, Structural Dynamics, and Materials Conference and Exhibit*, page 1394, 1999.

[49] T. Lieu, C. Farhat, and M. Lesoinne. Reduced order fluid/structure modeling of a complete aircraft configuration. *Computer methods in applied mechanics and engineering*, 195(41-43):5730–5742, 2006.

[50] P. C. Schulze, B. P. Danowsky, and T. Lieu. High fidelity aeroservoelastic model reduction methods. In *AIAA Atmospheric Flight Mechanics Conference*, page 2007, 2016.

[51] W. Zhao, N. Muthirevula, R. K. Kapania, A. Gupta, C. D. Regan, and P. Seiler. A subcomponent-based finite element model updating for a composite flying-wing aircraft. In *AIAA Atmospheric Flight Mechanics Conference, 2017*. American Institute of Aeronautics and Astronautics Inc, AIAA, 2017.

[52] J. E. Mottershead and M. Friswell. Model updating in structural dynamics: a survey. *Journal of sound and vibration*, 167(2):347–375, 1993.

[53] D. J. Ewins. *Modal testing: theory and practice*, volume 15. Research studies press Letchworth, 1984.

[54] A. Gupta, P. J. Seiler, and B. P. Danowsky. Ground vibration tests on a flexible flying wing aircraft-invited. In *AIAA Atmospheric Flight Mechanics Conference*, page 1753, 2016.

[55] C. P. Moreno, A. Gupta, H. Pfifer, B. Taylor, and G. J. Balas. Structural model identification of a small flexible aircraft. In *2014 American Control Conference*, pages 4379–4384. IEEE, 2014.

[56] R. D. Blevins. *Formulas for dynamics, acoustics and vibration.* John Wiley & Sons, 2015.

[57] A. Kotikalpudi, B. P. Danowsky, D. K. Schmidt, C. D. Regan, and A. Gupta. Real-time shape estimation for a small flexible flying-wing aircraft. In *AIAA Scitech 2019 Forum*, page 1818, 2019.

[58] C. V. Stahle and W. R. Forlifer. Ground vibration testing of complex structures. In *Flight Flutter Testing Symposium*, pages 83–90, 1958.

[59] J. S. Bendat and A. G. Piersol. *Engineering applications of correlation and spectral analysis.* John Wiley and Sons, 1980.

[60] R. Brincker, L. Zhang, and P. Andersen. Modal identification from ambient responses using frequency domain decomposition. In *Proc. of the 18*International Modal Analysis Conference (IMAC), San Antonio, Texas*, 2000.

[61] P. C. Schulze, P. Thompson, B. P. Danowsky, D.-C. Lee, and C. Harris. System identification and modal extraction from response data. *AIAA Atmospheric Flight Mechanics Conference*, 2013.

[62] R. Brincker, C. E. Ventura, and P. Andersen. Damping estimation by frequency domain decomposition. In *19th International Modal Analysis Conference*, volume 9, pages 698–703, 2001.

[63] B. P. Danowsky, D. K. Schmidt, and H. Pfifer. Control-oriented system and parameter identification of a small flexible flying-wing aircraft. In *AIAA Atmospheric Flight Mechanics Conference*, page 1394, 2017.

[64] W. Zhao, A. Gupta, J. Miglani, C. D. Regan, R. K. Kapania, and P. J. Seiler. Finite element model updating of composite flying-wing aircraft using global/local optimization. In *AIAA Scitech 2019 Forum*, page 1814, 2019.

[65] W. Zhao, A. Gupta, C. D. Regan, J. Miglani, R. K. Kapania, and P. J. Seiler. Component data assisted finite element model updating of composite

flying-wing aircraft using multi-level optimization. *Aerospace Science and Technology*, 95:105486, 2019.

[66] J. Moran. *An introduction to theoretical and computational aerodynamics.* Courier Corporation, 2003.

[67] P. Konstadinopoulos, D. Thrasher, D. Mook, A. Nayfeh, and L. Watson. A vortex-lattice method for general, unsteady aerodynamics. *Journal of aircraft*, 22(1):43–49, 1985.

[68] R. M. Cummings, W. H. Mason, S. A. Morton, and D. R. McDaniel. *Applied computational aerodynamics: A modern engineering approach*, volume 53. Cambridge University Press, 2015.

[69] D. K. Schmidt. Matlab-based flight-dynamics and flutter modeling of a flexible flying-wing research drone. *Journal of Aircraft*, 53(4):1045–1055, 2015.

[70] H. Pfifer and B. P. Danowsky. System identification of a small flexible aircraft-invited. In *AIAA Atmospheric Flight Mechanics Conference*, page 1750, 2016.

[71] R. H. Byrd, J. C. Gilbert, and J. Nocedal. A trust region method based on interior point techniques for nonlinear programming. *Mathematical programming*, 89(1):149–185, 2000.